THERMAL STRESS ANALYSIS OF DEFECT FORMATION IN FUSED-CAST ALUMINA REFRACTORIES

by

DOMINIC KA MAN AU

B.A.Sc., The University of British Columbia, 1997

A THESIS SUBMITTED IN PARTIAL FULFILLMENT OF
THE REQUIREMENTS FOR THE DEGREE OF

MASTER OF APPLIED SCIENCE

in

THE FACULTY OF GRADUATE STUDIES

(Department of Metals and Materials Engineering)

We accept this thesis as conforming
to the required standard

THE UNIVERSITY OF BRITISH COLUMBIA

October 1999

In presenting this thesis in partial fulfilment of the requirements for an advanced degree at the University of British Columbia, I agree that the Library shall make it freely available for reference and study. I further agree that permission for extensive copying of this thesis for scholarly purposes may be granted by the head of my department or by his or her representatives. It is understood that copying or publication of this thesis for financial gain shall not be allowed without my written permission.

Department of Metals and Materials Engineering

The University of British Columbia
Vancouver, Canada

Date October 14, 1999

Abstract

Mathematical models have been developed to predict the temperature, stress and strain evolution during the manufacture of fused-cast αβ-alumina refractories approximately consistent with the process used at Monofrax Inc.. An uncoupled thermal stress model, which consists of a heat transfer model to predict the temperature evolution and a mechanical model to predict the stress and strain evolution, has been formulated. The commercial finite element code ABAQUS was employed in the thermal stress analysis.

The thermal model was validated against industrial thermocouple and pyrometer measurements obtained at Monofrax Inc., located in Falconer, NY. The model predictions were in good agreement with the thermocouple data obtained at several locations from within the graphite mold, during Stage I cooling, and in the alumina annealing ore, during Stage II cooling. In Stage I cooling, it has been necessary to augment the conductivity of the liquid alumina to account for convective heat transport. In Stage II cooling, it proved necessary to account for asymmetric placement of the block in the annealing bin.

The temperatures obtained from the thermal model were utilized as input to the mechanical model. Elastic and elastic-plastic stress analyses were conducted to assess the evolution of stress and strain during the casting process. The strain rate independent inelastic behavior of the casting based on the flexural tests performed at Oak Ridge National Laboratory was incorporated into the elastic-plastic stress model. The results obtained from the elastic-plastic stress model were more realistic than those predicted by the elastic analyses. However, the plastic strain may be under-predicted during Stage II cooling owing to the strain rate independent plasticity employed in the analysis.

The preliminary stress/strain predictions indicate that the β-alumina core plays an important role in the generation of tensile stresses and likely gives rise to the generation of cracks. Since high tensile stress/strain was found to develop within the refractory, it is likely that crack initiates subsurface and propagates outwards. Overall, the results of the present research show the importance and usefulness of developing the ability to predict temperature, stress and strain evolution in the fused-cast αβ-alumina refractories during the manufacturing process.

Table of Contents

List of Tables

Page

List of Figures

Page

List of Symbols

Latin Symbols	Description	Units	Page
a	distance from the support to the load applicator when the specimen is straight	m	34,41
A	material constant		16,17,21
b	specimen width	m	34,41
C_p	specific heat	J kg^{-1} K^{-1}	46,61-63
E	Young's modulus	Pa	34
f_c	fraction of contact between the casting and mold surfaces		50,53-55
f_s	a field variable used in the *ufield* subroutine reflecting the fraction to which the alumina annealing ore is sintered		57,58
fv1	a field variable used in the *ufield* subroutine reflecting the phase distribution in the as-cast material at each integration point		72,73
fv2	a field variable used in the *ufield* subroutine reflecting the void distribution within the casting		73
h	specimen height	m	34,41
h_c	heat transfer coefficient due to contact conduction	W m^{-2} K^{-1}	50,53,55
h_{rad}	effective heat transfer coefficient due to radiation	W m^{-2} K^{-1}	50
k	material constant		10,76
k	thermal conductivity	W m^{-1} K^{-1}	46,49, 61-63
L	span length between the lower supports	m	34,41
n	material constant		10,76
n	stress exponent		16,17,21
n	normal to surface direction		49
P	applied load	N	34
PE22	predicted plastic strain which is parallel to the broad face of the refractory		83,95,97
R	molar gas constant (8.3144)	J mol^{-1} K^{-1}	16
q	heat flux	W m^{-2}	49
q	heat flux across the surface of the mold	W m^{-2}	51
Q_c	activation energy for creep	J mol^{-1}	16,17,21
$\dot{Q}$	volumetric heat source term	W m^{-3}	46
S22	predicted stress which is parallel to the broad face of the refractory	Pa	78-81, 89-94,96
t	time	s	49
t	current total model time	s	50,55

$t_{elapsed}$	elapsed time, or duration, of Stage I or II cooling	s	50,55
T	temperature	K	16,46,49
T	current temperature of the alumina ore evaluated at each material integration point within an element	°C	58
T_1	temperature of the casting	K	50
T_2	temperature of the mold	K	50
T_a	ambient temperature	K	51
T_h	temperature above which the alumina ore becomes hard sintered	°C	58
T_s	temperature of the casting surface	K	51
T_s	temperature above which the alumina ore becomes weakly sintered	°C	58
T_{th}	threshold temperature below which sintering does not occur	°C	58
U	span length between the upper supports	m	34,41

Greek Symbols	**Description**	**Units**	**Page**
δ	corrected load-point displacement of Monofrax-M	m	33,34
$\delta_{Monofrax\text{-}M\ +\ load\ train}$	displacement obtained from the flexural tests on the Monofrax-M specimens	m	33,34
$\delta_{load\ train}$	displacement gathered from the flexural tests on the SiC bend bar	m	33,34
$\delta_{SiC\ bend\ bar}$	load-point displacement based on the elastic deflection of the SiC bend bar	m	33,34
ε	outer-fiber tensile strain		34
ε	effective emissivity		50,51
ε	emissivity of the mold (Equation 5.7)		51
ε_1	emissivity of Monofrax M		51
ε_2	emissivity of the mold		51
$\bar{\varepsilon}^p$	total equivalent plastic strain		10
$\dot{\varepsilon}$	creep strain rate		16
$\rho_{theoretical}$	theoretical density	kg m^{-3}	17
ρ	density	kg m^{-3}	17,46, 61-63
σ	stress	Pa	16,34
σ	Stefan-Boltzmann constant (5.67×10^{-8})	W m^{-2} K^{-4}	50,51
σ_e	Von Mises effective stress	Pa	10
σ_o	yield stress	Pa	10

Acknowledgements

I would like to thank my advisor, Dr. Steve L. Cockcroft for his utmost support and encouragement throughout the research programme. I am grateful to the Monofrax related personnel, Dr. Steve M. Winder, Mr. Amul Gupta, and Mr. Dennis Walrod, for their technical help. I wish to thank Monofrax Inc. for the support of research expenses, and the provision of valuable data. I would also like to thank Oak Ridge National Laboratory (ORNL) and its personnel in the high temperature materials laboratory, Dr. Andrew A. Wereszczak and Dr. Kristin Breder, for the support and technical help on the laboratory experiments.

In addition, I have profited from numerous discussions with my colleagues and professors at the University of British Columbia. I particularly thank Dr. Daan M. Maijer, Dr. Mary A. Wells, Dr. Tom Troczynski and Dr. Warren J. Poole.

CHAPTER 1

INTRODUCTION AND OVERVIEW

1.1 Introduction

Refractories are often used in high temperature industrial processes involving materials manufacturing because of their insulation capabilities and ability to contain reactive materials at elevated temperatures. They are essential in the production of glass, metals, cements and other materials. One class of refractory, called fused-cast refractory, is widely used in glass industry for furnace linings owing to its superior corrosion/erosion resistance to the environment present in float-glass furnaces. These include refractories such as fused-cast alumina-zirconia-silica (AZS), and αβ-alumina.

During the solidification process, fused-cast refractories are subject to a variety of defects that are comparable to those found in the metal castings. These include cracks that arise due to excessive thermal stresses or strains and porosity due to volumetric contraction associated with solidification. Under extreme conditions existing in modern glass furnaces, these defects can lead to excessive chemical attack, which can have a negative effect on glass quality. On-going efforts to improve glass quality while at the same time reducing costs have led to a need for higher quality fused-cast refractories. To achieve high quality products, these defects must be controlled and preferably eliminated.

This thesis is focused on the development of a mathematical model capable of predicting the thermal and stress/strain history in fused-cast αβ-alumina refractories during the casting process. The ultimate goal of this work is to understand the mechanism(s) leading to the formation of cracks, which are a common defect, found in

this type of refractory block. This work has been sponsored by Monofrax Inc., a leading manufacturer of fusion cast products.

1.2 Background

Monofrax Inc., located in Falconer, NY, manufactures various types of fused-cast ceramic components for different applications. Fusion cast αβ-alumina, sold under the trademark Monofrax-M, is one class of product and is used in glass furnace superstructure, known as crown block. Monofrax-M is a dense, high alumina fused-cast refractory formed by first melting a fusion of oxides, typically 94.5 weight % Al_2O_3, 3.8 weight % Na_2O and other minor oxides, in an electric arc furnace and then pouring the resulting liquid into a graphite mold [1]. After a short time, the graphite mold is removed once a suitable solid shell has formed and the refractory is placed into an annealing bin (box) and covered in an insulating annealing sand (alumina ore), where it may take a few weeks to cool.

To avoid cavity formation within the refractory during solidification, components are cast with an oversized header (refer to Figure 1.1), which serves as a liquid reservoir. Typical melt densities are 2660 kg/m^3 and solid densities are 3590 kg/m^3, representing a ~35% volume reduction [2]. The resulting void distribution in a cast block with header attached is shown in Figure 1.2. The header is removed from the refractory block using a diamond-saw prior to surface grinding. Typical block sizes for a glass furnace crown are 0.4 m by 0.5 m by 1.0 m (16 inches by 20 inches by 40 inches).

Under equilibrium solidification conditions [3], the mixture of oxides would solidify to form a material consisting of crystalline phases of alpha- (~38 vol.%) and beta-alumina (~62 vol.%) together with a small amount of interstitial glass, less than 1% [1]. However, in practice, refractory blocks of this composition solidify with an β-alumina core surrounded by α-β shell. The β core forms due to rejection of Na_2O, a β stabilizer, at the solid/liquid interface – refer to Figures 1.2 and 1.3 in which the β core can be seen.

In addition to void formation, the other major defect and the most problematic from a process viewpoint, is crack formation. Cracks have been found in all the castings that have been cut open for examination. Figures 1.2 and 1.3 show the orientations and locations of the cracks found in a typical refractory. The formation of the β core would appear to have important implications in terms of the formation of crack defects as the majority of cracks appear to emanate from or terminate at the α-β/β boundary. These cracks can reduce the erosion-corrosion resistance of the refractory and can also lower the ability of the refractory to withstand thermal cycling. Blocks that exhibit surface cracks at the hot face of the block (the bottom horizontal plane of the casting that is in contact with the vapor phase species generated at the glass melt surface inside a glass furnace) must be rejected and recast. Moreover, if the customer is not willing to accept a cracked product, the refractory is recycled at a considerable cost. Hence, there is a strong desire to determine the origins of these cracks and to eliminate them.

1.3 Fundamental Based Approach

Historically, fused-casting processes have been developed on the basis of trial-and-error optimization. In terms of solving specific problems, such as the formation of a particular crack, this approach is often time-consuming, costly and ineffective. The main objective of the present study is to develop a fundamental understanding of crack formation during fusion casting of αβ-alumina refractories. This is to be achieved through the development of a finite element method (FEM) based model to simulate the thermal behavior of a solidifying Monofrax-M crown block and the resulting stress/strain evolution during different stages of the standard production process at Falconer. The 'Monofrax-M' model is broken into two components – the thermal model and the mechanical, or stress model – which, are run separately and are uncoupled.

The geometry of the block necessitates a three-dimensional analysis in both the thermal and the mechanical models. The thermal model is based on the Fourier's law of heat conduction using the law of conservation of energy. The various stages of the casting process need to be properly accounted for in the thermal model to reflect the different steps in the manufacturing process. It is essential that both the refractory and the molding materials including those associated with the graphite mold and the annealing bin be included in the thermal model in order to properly account for the flow of heat in the block. Characterization of the various thermal boundary conditions and initial conditions is also necessary as is the quantification of the various thermo-physical properties. Moreover, since these materials are subject to a large range in temperature, properties such as the thermal conductivity and the specific heat need to be incorporated

into the model as temperature dependent. Once validated against thermocouple data, the resulting thermal history can then be input to the thermal stress model.

The stress model is solved based on the differential equations of equilibrium and the compatibility conditions. The temperature predictions obtained from the heat transfer model serve as input (thermal loads) to the stress model. Unlike the thermal model, only the fused-cast alumina refractory is involved in the stress analysis as the casting can be assumed to be free of interaction with the mold (surface traction free). Owing to the broad range of temperature that the casting experiences, the material properties such as the elastic modulus and the thermal expansion coefficient need to be implemented into the model as a function of temperature. In addition, the effect of the different thermal expansion or contraction behavior of the αβ-alumina and the β-alumina has also to be addressed. This entails the incorporation of an algorithm into the model in which the regions of αβ-alumina and β-alumina can be distinguished. Assessment of the effect of void formation will also be required due to a decrease in elastic modulus or strength in the void region. The resulting evolution of stress and strain in the refractory during various stages of the casting process can be linked to the occurrence of crack defects. Mechanisms can then be formulated and remedial actions can be prescribed for their elimination.

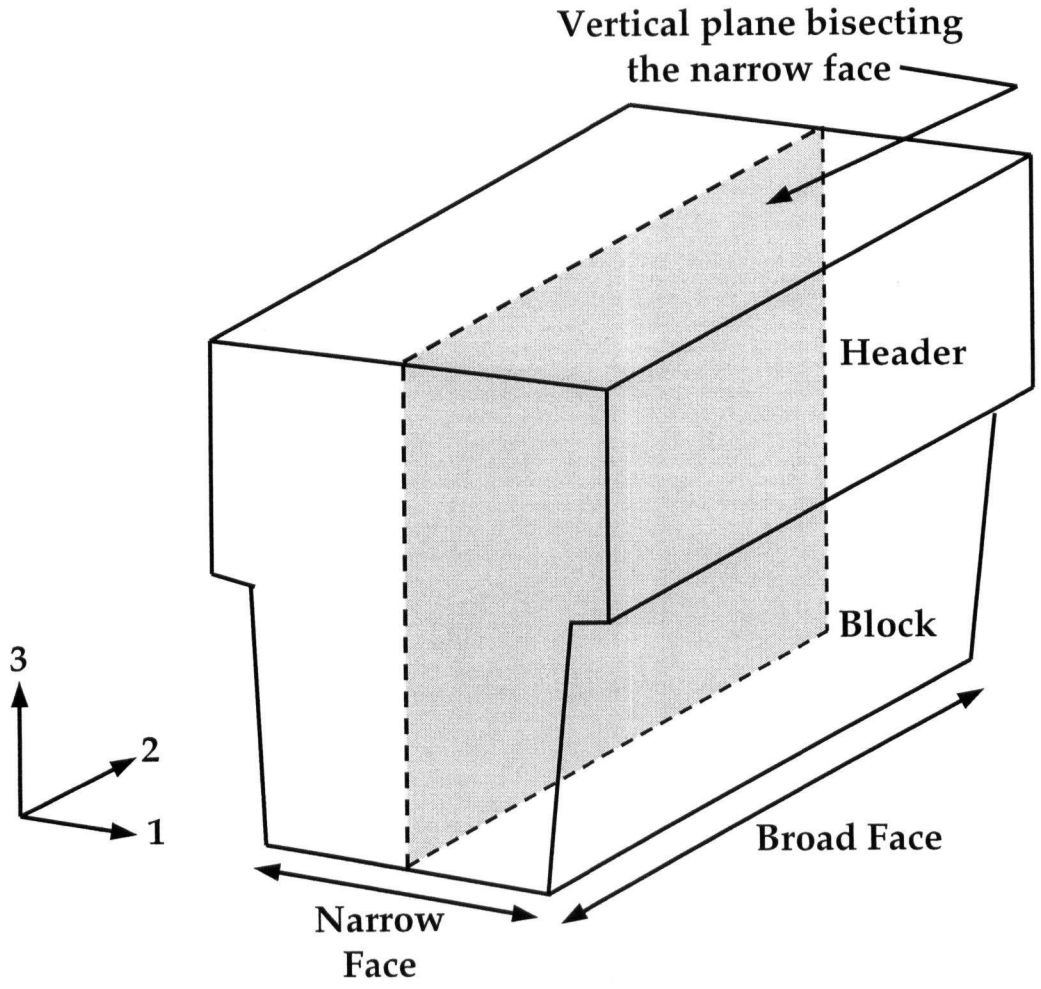

Figure 1.1 – Schematic illustration of a fused-cast αβ-alumina refractory casting with an oversized header (not to scale).

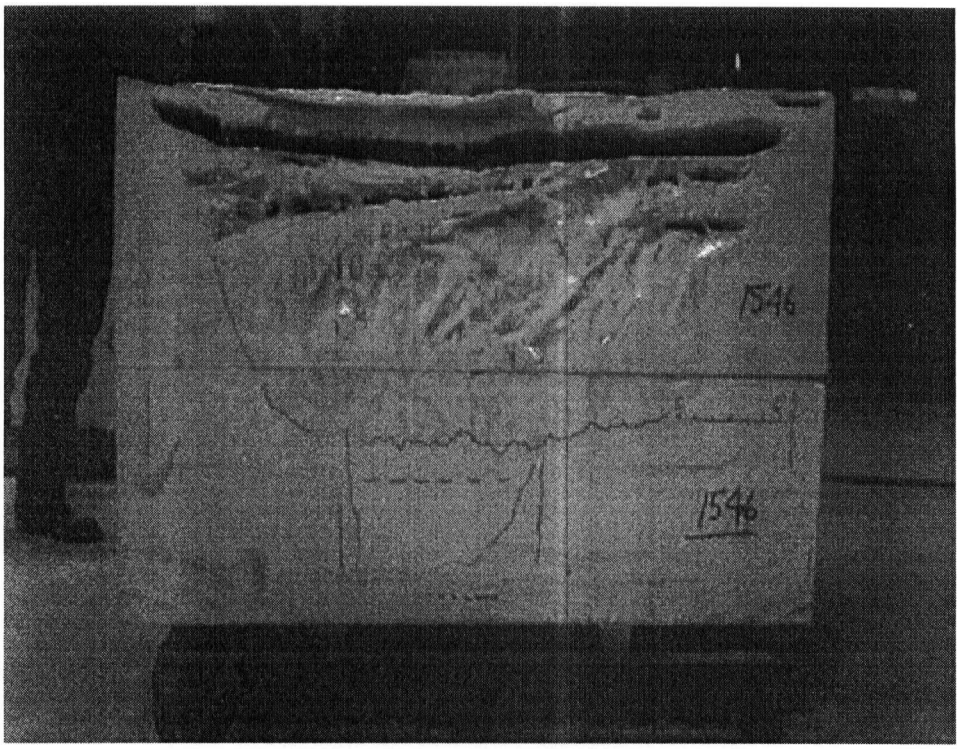

Figure 1.2 – Cross-section of a Standard Operating Practice (SOP) Monofrax-M block taken at the vertical plane bisecting the narrow face of the casting (refer to Figure 1.1). Cracks and voids can be observed and the β-alumina region is being outlined. Note that the cracks are vertical and perpendicular to the broad face of the block resulting from the tensile stress acting parallel to the broad face (tensile stress in direction-2 in Figure 1.1).

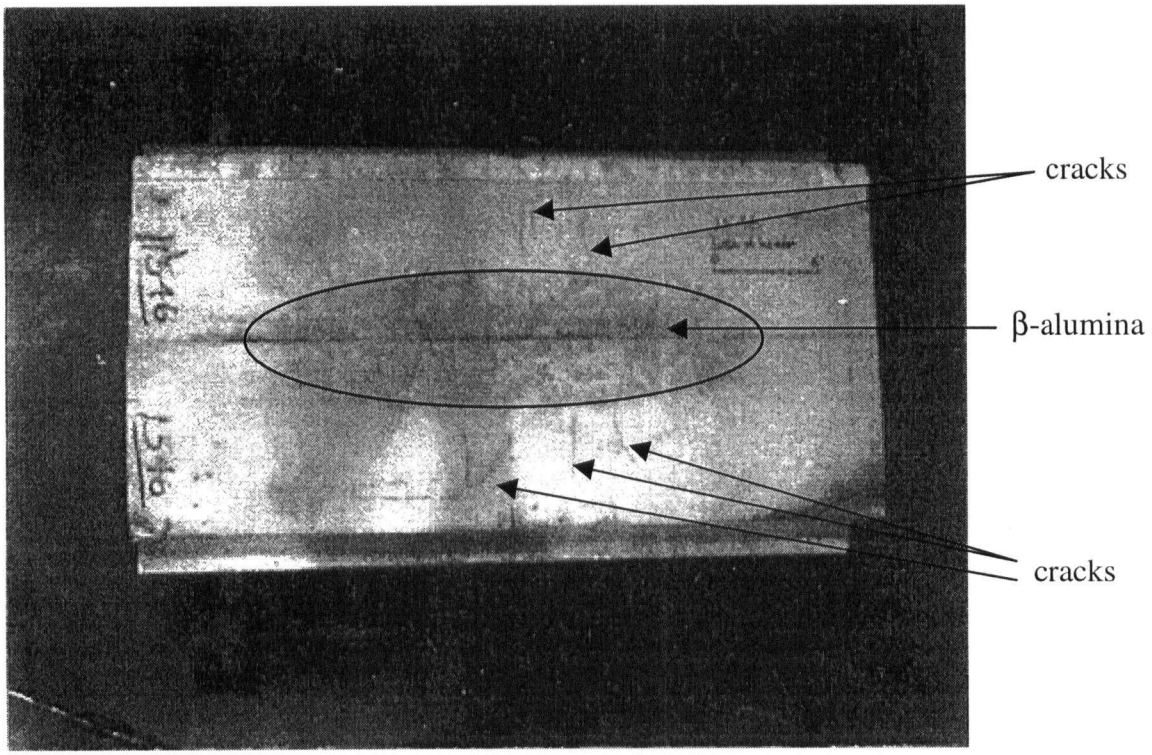

Figure 1.3 – Top view of a SOP Monofrax-M block taken at the horizontal plane just below the header. The β-alumina region can be observed in the center of the casting and the cracks appear to emanate from or terminate at the αβ/β-alumina interface.

CHAPTER 2

LITERATURE REVIEW

A review of the literature has indicated a scarcity of information on the processing of fused-cast refractories. The few studies that do exist are presented below together with some relevant literature on metal-casting processes. The review of metal casting processes focuses on those studies that apply fundamental based mathematical models to understand the development of crack defects. In addition, the constitutive behavior of fused-cast refractories is also examined.

2.1 Casting Processes

Crack defect formation is found in many metal castings owing to thermal stresses [4-6]. In the continuous casting of steel billets, for example, crack formation arises due to the generation of thermal stresses in the solid shell owing to the high heat-extraction rates. Mathematical models of heat flow, together with the measured material properties of steel at various temperatures, have led to an understanding of the mechanisms responsible for defect formation and important improvements in billet quality [4].

In the manufacturing of thick parts of high-strength aluminum alloys, which are often rolled, forged, or extruded, significant distortion of the products arises from the generation of thermal stresses resulting from a drastic quenching of the component during casting [5]. To help develop methodologies for control of such complex phenomena, finite element (FE) calculations have been applied by Jeanmart and Bouvaist [5] to determine the temperature distribution, thermal strains, and residual stresses arising during manufacture. In the investigation by Jeanmart and Bouvaist, a non-linear heat

transfer analysis was first performed followed by an un-coupled elastic-plastic stress analysis using the predicted temperature distribution as the 'thermal loads' input to the stress analysis. The elastic-plastic stress analysis was based on the Ramberg-Osgood relationship to model the stress-strain curve of the material using the formulation [5]

$$\sigma_e = \sigma_o + k\left(\varepsilon^p\right)^n \tag{2.1}$$

where, σ_e is the Von Mises effective stress, σ_o is the yield stress, k and n are constants and ε^p is the total equivalent plastic strain. Since plasticity data is required in the elastic-plastic stress analysis, tensile tests were carried out at various temperatures to characteristic the inelastic behavior of the material. The model predictions were shown to have good agreement with the measured values of residual stresses. Moreover, these computer simulations made considerable contributions to the physical understanding of the residual stress build-up during production.

In gray iron castings, the problems are similar to those found in the fused-cast refractory processes. In a study by Wiese and Dantzig [6], finite element analysis (FEA) was used to simulate the heat transfer and thermal stress evolution as the casting solidifies and cools. In this approach, stresses resulting from thermal displacements in the cooling casting were computed in an elastic-viscoplastic stress analysis requiring that the creep behavior of the gray iron to be evaluated in addition to the 'plastic' response. Due to the mechanical behavior of the gray cast iron, different properties in tension and compression were also incorporated into the model.

2.2 Computer-Based Mathematical Models on Refractory Components

In addition to metal castings, numerical techniques have also been applied to refractory components to address design problems [7-9]. According to Bradley et al. [7], who examined the thermal stress fracture of refractory components in high-temperature industrial furnace linings and metallurgical process vessels, heat flow may be assumed to be one-dimensional (1-D). A FEA conducted by the authors for selected cases revealed that, not surprisingly, the maximum principal tensile stress is directly proportional to elastic modulus, heating or cooling rate, and coefficient of thermal expansion.

In terms of applicability to the present study, there are several shortcomings to the Bradley study. Firstly, the study is too general in nature and thus limits its applicability to specific refractory lining structures. In general, the modeling of heat flow is a complex matter that requires a case-by-case analysis using a numerical method such as FE rather than assuming that the heat flow is always one-dimensional. The assumption, therefore, eliminates the possibility of multi-dimensional stresses and strains that may be generated in the refractory. Secondly, the material properties were assumed to be independent of temperature in Bradley's model. In fact, thermal conductivity is often non-linear and temperature dependent in many refractory materials. The analysis of two-dimensional stress distribution may therefore be somewhat limiting. In addition, the Bradley study was only concerned with the thermo-elastic model and failed to address any high-temperature inelastic or plastic deformation during service.

In another study by Chang et al. [8], segmented thick-walled refractory structures were analyzed. A major simplification was made by assuming that the thermal conductivity and thermal diffusivity were independent of temperature and position. The

resulting analytical temperature distribution was one-dimensional and dependent on time and position along the length of the refractory.

In the Chang study, the stresses were analyzed using a two-dimensional finite element model. A limited number of three-dimensional cases were also investigated. The calculated stress profiles indicated that the maximum tensile thermal stresses were always found along the centerline of the refractory. It was also found that the magnitude of stress decreased with increasing thermal diffusivity and that changes in length of the refractory did not appear to reduce the probability of thermal stress fracture.

The Chang study has a similar drawback as the Bradley's model in obtaining the temperature distribution. The analytical thermal profile is simplified, being one-dimensional, and caution should be exercised due to this limitation. It should also be noted that like the Bradley study, the temperature dependency of thermal conductivity was not addressed in the Chang study. Furthermore, many candidate materials for basic oxygen furnaces exhibit substantial softening and creeping at high temperatures. The model, however, only dealt with elastic behavior. Thus, the predicted thermal stresses might be over-estimated in this case, which would affect the predicted probability of failure and accuracy of the model.

Unlike the previous two studies, Knauder and Rathner [9] evaluated both the temperature and stress distributions of the refractories based on FEM. In their thermo-mechanical analysis of basic refractories in a bottom blown converter, a quarter of the vessel bottom was modeled. A 2-D model assuming no circumferential heat flow was also developed for the 3-D quarter section of the bottom, which represented a symmetry plane with the 3-D model. A comparison of the 2-D and 3-D results confirmed that the

models were in agreement. Moreover, Knauder and Rathner analyzed the stress distribution based on the temperature results. A two-dimensional FEM elastic analysis was carried out to reduce computational effort. Three-dimensional results were also obtained for limited cases.

In the Knauder and Rathner study [9], the reported stresses were way above the uniaxial compressive strength of the refractory materials. This is mainly due to two reasons: 1) the assumption of linear elastic behavior and 2) the homogeneous continuum at the bottom. In regard to the constitutive behavior, it was noticed that the stress-strain curves of carbon-bonded refractories are highly non-linear and thus, for a given strain, the linear elastic model over-predicts stress. Hence, a more quantitative analysis should address stress relaxation due to creeping of the material, which may be significant at high temperatures. In regard to the second shortcoming, joints often present in the refractory lines can significantly alter the thermal stress field depending on gap clearances and mortar material. A proper analysis should therefore include refractory-to-refractory contact as part of the compliment of boundary conditions. Nonetheless, the analysis, as a whole, is good for qualitative comparison.

2.3 Computer-Based Mathematical Models on Fused-Cast Refractories

Cockcroft and Brimacombe [10-11] performed thermal stress analysis on fused-cast AZS refractories using a three-dimensional finite element model. Uncoupled thermal and stress models were employed to estimate the temperature distribution, as well as stresses and strains in the solidifying shell of the cast refractory. The stress model assumed simple thermo-elastic behavior but included the thermal dilatational expansion associated

with the tetragonal-to-monoclinic phase transformation of ZrO_2. The model predictions revealed the critical role of the tetragonal-to-monoclinic phase transformation, which is predicted to generate tensile strains around the transformation zone. With the aid of the mathematical model, it is evident that the major thermal resistance to heat extraction from the molten refractory lies in the mold and that changes to the mold design and the control of the differential cooling are the solution to the problem. Therefore, to eliminate the cracking problems found in the AZS refractories, an understanding of the mechanisms responsible for crack formation is crucial.

Similar to the other refractory studies that employed the use of numerical techniques, the stress model by Cockcroft and Brimacombe [10-11] is based on elastic behavior of the AZS refractories. Owing to the glass constituents within the refractories, inelastic or irreversible deformation takes place at elevated temperature. It is likely that the stress predictions obtained from the model would be over-estimated and caution must be used in interpreting the results of this analysis.

In an attempt to consider the inelastic deformation of the fused-cast AZS refractories, Lu et al. [12] developed a finite element model to study the stress and strain evolution in the casting. Unlike the stress analysis by Cockcroft and Brimacombe [10-11], Lu et al. incorporated the Drucker-Prager plasticity into the model, which assumed a spherical block casting rather than the standard rectangular block. Uniaxial stress-strain behaviors in tension and compression were evaluated for the model input and it was found that there is considerable difference between the tensile and compressive flow stress in the refractories. Although there are several limitations in this model in terms of the shape of the block and the thermal histories, the analysis was able to identify critical

parameters that affect the inelastic strains, stresses, and the cracking that develop in the AZS castings.

In a recent study, Wang [13] investigated the effects of the geometric and physical parameters of a cooling system on the temperature distributions in the solidifying fused-cast αβ-alumina refractories. A two-dimensional thermal analysis was conducted using the finite difference method. Boundary conditions relating to heat transfer between the refractory and the mold, as well as the gap formation mechanism, were based on the fused-cast AZS refractory analysis by Cockcroft and Brimacombe [10-11]. It is found that the thermal conductivity of the insulation material as well as the geometric parameters of the annealing system play an important role in the temperature gradient of the casting.

The analysis by Wang can be used to begin to understand the complicated processes leading to crack formation in fused-cast αβ-alumina refractories. However, Wang's analysis falls short in that it was not three-dimensional and does not describe key features of the casting process. Moreover, the computer simulation of heat transfer in the casting process was not verified against industrial measurements and many of the required material properties were not characterized.

2.4 Constitutive Behavior of Refractories

In most of the above studies on refractories, inelastic behavior of the material is often neglected to simplify the analysis. However, most ceramics exhibit some degree of permanent deformation when under load at elevated temperatures. During the casting process, the αβ-alumina may be expected to be subject to a broad range of thermally

induced stresses as the block solidifies and cools to near room temperature. The two most common approaches (constitutive models) used to describe inelastic or permanent deformation in materials are plasticity and creep. Physically, the strain resulting from either plastic or creep deformation are indistinguishable from one another [14]. Thus, either approach could be used to quantify stresses and strains arising in the casting process.

Typically, time-dependent deformation or creep in ceramics takes place at high temperatures under modest stress levels [15]. This time-dependent deformation usually exhibits three distinct regimes: a primary creep stage during which the creep rate rapidly decreases, a secondary or steady-state stage with a nearly constant creep rate, and finally the tertiary stage during which the creep rate increases in an unstable manner just before rupture [16]. The power-law creep equation is one of the most widely used constitutive creep models. In this model, the creep strain rate is given by the relationship

$$\dot{\varepsilon} = A\sigma^{n}\exp\left(\frac{-Q_c}{RT}\right) \tag{2.2}$$

where, $\dot{\varepsilon}$ is the creep strain rate, A is a constant, σ is the stress, n is the stress exponent, Q_c is the activation energy for creep in J mol^{-1}, R is the molar gas constant (= 8.3144 J mol^{-1} K^{-1}), and T is the temperature in Kelvin [17]. This power-law creep equation is applicable to the steady-state (secondary) creep region exhibited by many materials including some ceramics. While the power law creep equation could address sensitivity to temperature and stress, its applicability for the quantification of the stress and strain field in the fused-casting process is unclear and will depend on the extent to which steady state flow conditions prevail.

In terms of available data, Munro [18] determined the steady-state creep constants, A and n, as well as the activation energy Q_c, for a sintered α-alumina (mass fraction of $Al_2O_3 \geq 0.995$, relative density ($\rho/\rho_{theoretical}$) ≥ 0.98 and nominal grain size is 5 μm). In another creep study, Wereszczak et al. [19] evaluated the steady-state compressive creep constants of 100% β-alumina and 50% α / 50% β-alumina refractories. Table 2.1 compares the creep characteristics and test conditions of the various alumina refractories.

It can be observed from Table 2.1 that the creep characteristics are sensitive to the various grades of alumina refractories and only the steady-state creep information is evaluated. Deformation associated with primary creep may also be important in transient loading applications such as those occurs in a casting process or in the early stages of thermal cycling.

Unlike creep equations based on steady-state creep, the plasticity approach has the ability to easily address the early stages of deformation. Analyses of casting processes that adopted the plasticity approach include the study by Jeanmart and Bouvaist [5] on an aluminum alloy and Lu et al. [12] on fused-cast AZS refractories. The well-known Von Mises yield criterion commonly used for metal plasticity can be used for materials exhibiting isotropic behavior. Temperature dependencies in the yield stress as well as the hardening behavior can be easily accommodated in most commercial FE packages. Some packages also permit strain rate dependent plastic behavior needed to address the varying loading conditions existing in the casting process. The one potential drawback of the plasticity approaches is that they fail to accumulate inelastic strain at a constant load –

i.e. exhibit time-dependent deformation, which may be expected to occur to some extent in the casting process.

2.5 Monofrax-M

Thermo-physical and Thermo-mechanical Behavior – In addition to the constitutive behavior of fused-cast αβ-alumina refractories, quantification of the thermal and stress/strain fields during solidification processing requires data describing the thermo-physical and thermo-mechanical behavior of this material over the temperature range experienced in the casting process. Some of these data are found in the product brochure [1]. For instance, typical data for the thermal conductivity, thermal expansion and compositions of Monofrax-M are shown in Figure 2.1. Since very little additional information can be obtained from the literature, most has had to be measured.

Volumetric Latent Heat of Fusion – The volumetric latent heat of fusion is another thermo-physical property that needs to be quantified for the heat transfer analysis. According to the Na_2O-Al_2O_3 phase diagram (refer to Figure 2.2) [3], a melt containing between 90 and 100 mole % Al_2O_3, would solidify by first forming primary α-alumina until a temperature of approximately 2000°C is reached at which point the β-alumina would form to complete the solidification process. Assuming equilibrium solidification, Monofrax-M, which consists of roughly 93.2 mole % Al_2O_3, starts solidifying as primary α-alumina at 2026°C, the liquidus, and reaches the solidus at 2000°C at which point the volume percent of α-alumina and β-alumina would be expected to be approximately 38 and 62, respectively. The latent heat of fusion for α-alumina is 111.086 kJ mol^{-1} [20] but no value for β-alumina is reported in the literature.

αβ-Alumina and β-Alumina – As discussed in Section 1.3, the effect of the different thermal expansion or contraction behavior of the αβ-alumina and the β-alumina needs to be examined. The investigation of Cockcroft and Brimacombe [10-11] on fused-cast AZS refractories, which included the thermal dilatational expansion associated with the tetragonal-to-monoclinic phase transformation, showed the critical role of the phase transformation on the generation of stresses and strains on the casting.

Void Distribution – In addition to addressing the αβ-alumina and the β-alumina distribution and the associated expansion and contraction behavior, the void formation occurring in the casting process also needs to be evaluated. No reported literature has been found on the assessment of the effect of void formation in the fused-cast refractories. However, the void distribution within the casting may have an effect on the generation of stresses and strains due to a decrease in elastic modulus or strength in the void region.

2.6 Summary

Based on the literature review, fundamental based mathematical models can be used to predict the temperature, stress and strain evolution of the fused-cast αβ-alumina refractories to understand the development of crack defects. Due to the nature of the casting process, the analyses are required to be three-dimensional and should incorporate the actual geometry of the casting and the molding materials. The temperature predictions obtained from the thermal analysis can serve as 'thermal loads' input to the stress analysis. In order to formulate the heat transfer and the mechanical models, validation of the thermal model through industrial measurements and proper

quantification of the boundary conditions, as well as the thermo-physical and themo-mechanical behavior of this material over the temperature range experienced in the casting process are required. The characterization of the αβ-alumina and the β-alumina regions and the void distribution needs to be addressed. Furthermore, strain rate sensitive inelastic behavior of the refractory needs to be examined and implemented into the stress model to properly reflect the deformation behavior taking place in the casting process.

Table 2.1 – Comparison of the creep constants obtained for various alumina refractories [18-19].

Refractories	A (s^{-1})	n	Q_c ($kJ \cdot mol^{-1}$)	Temperature (°C)	Applied Stress (MPa)
Sintered α-alumina	3.6×10^{11}	1.08	323	1200-1800	100-200
100% β-alumina	5.6×10^{-2}	0.9	151	1400-1593	0.17-1.03
50% α/50% β-alumina	1.1×10^{-10}	0.9	544	1400-1593	0.17-1.03

Technical Data
Typical Thermal Conductivity

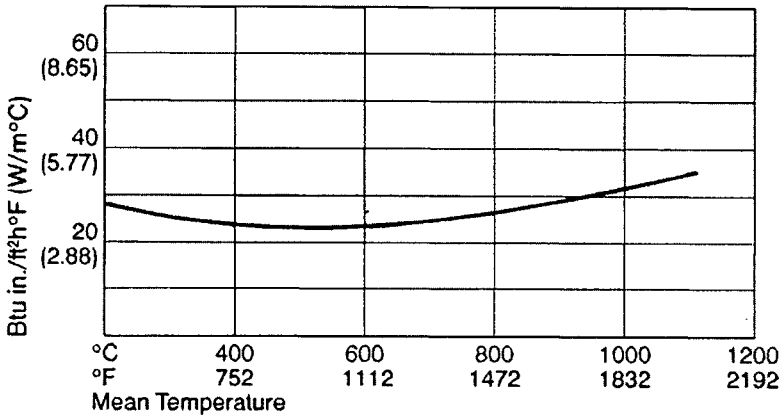

Typical Thermal Expansion

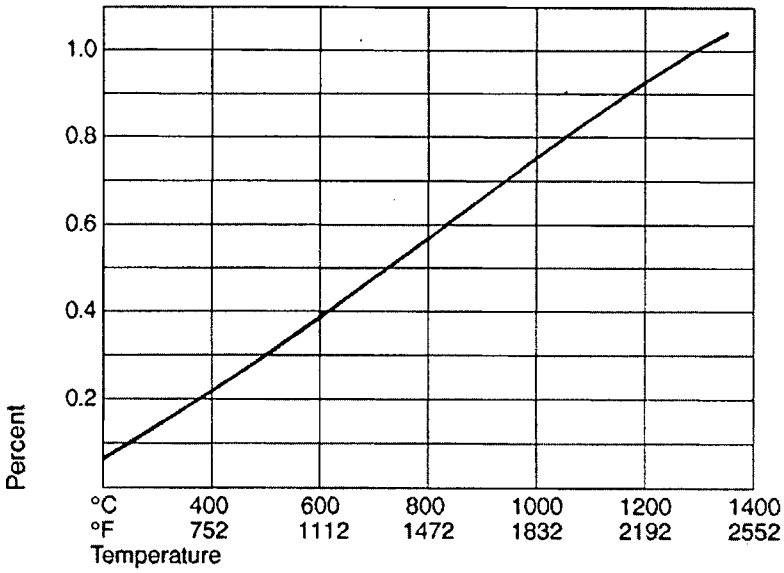

Typical Chemical Analysis:	%
Al_2O_3	94.5
Na_2O	3.8
SiO_2	0.8
Fe_2O_3	0.1
CaO	0.2
Other	0.6

Figure 2.1 – Thermal conductivity, thermal expansion and typical composition of Monofrax-M [1].

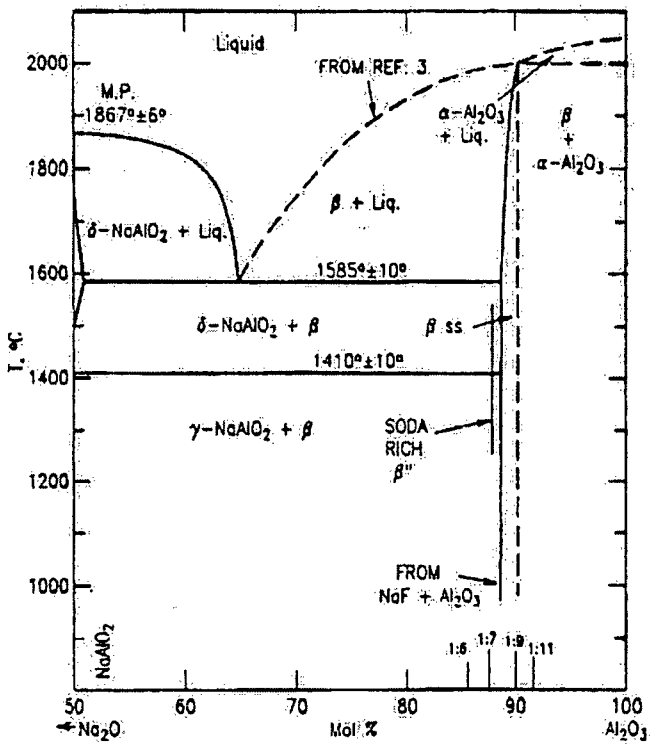

Figure 2.2 – Phase diagram of Na_2O-Al_2O_3 [3].

CHAPTER 3

SCOPE AND OBJECTIVES

3.1 Scope of the Research Programme

The purpose of this research programme is to develop a mathematical model capable of predicting the temperature, stress and strain distribution during the solidification and subsequent cooling of the Monofrax-M castings. The ultimate goal is to understand the mechanism(s) leading to the formation of cracks found in this type of refractory block.

To achieve this goal, fundamental based mathematical models were developed based on the commercial finite element code, ABAQUS[†]. The non-linear solution capabilities in ABAQUS are well-developed and robust making it well suited to solve the heat transfer and stress problem. Additional features of the code relevant to the Monofrax-M crown block include the ability to handle multiple thermal load steps as well as the addition and removal of materials such as is required in the simulation of graphite stripping, floating and annealing in alumina ore. Also, the recently introduced sparse matrix solver enables larger geometrically more complex 3-D models to be tackled with reasonable execution times. Other features of the code such as the ability to define field variables and specify field variable dependencies permit additional features of the Monofrax-M casting processes to be tackled including the β-alumina core and the solidification shrinkage void distribution.

Owing to a scarcity of the information in the literature, most of the input parameters for the heat transfer and mechanical models were evaluated by Monofrax Inc. or independent research laboratories. An assessment of the sensitivity of the models to

this data was performed to determine the effect of this data on the analyses. Once formulated, the thermal model was then validated by comparison to industrial plant data obtained from Monofrax Inc. Thermocouples embedded in the molds (both graphite mold and alumina ore annealing bin) were used to obtain local thermal histories for the purpose of verifying the assumptions made in formulating the model.

A good understanding of the high-temperature behavior of this refractory is essential to formulate crack formation mechanisms. The preliminary elastic stress analysis was formulated based on the elastic modulus values measured by a research laboratory. Additional information or the inelastic stress-strain behavior at elevated temperatures was also needed. Experiments were performed at ORNL (Oak Ridge National Laboratory in Oak Ridge, Tennessee) in an attempt to evaluate the inelastic behavior of this material. Preliminary results obtained from the elastic and elastic-plastic stress analyses were compared to determine the influence of assumptions relating to the constitutive behavior on the prediction of crack formation during solidification and cooling.

[†] ABAQUS is a registered trademark of Hibbitt, Karlsson & Sorensen, Inc.

3.2 Objectives of the Research Programme

The objectives of the present study are as follows:

[1] To formulate, develop and verify mathematical models capable of predicting the temperature and stress/strain field evolution in solidifying Monofrax-M blocks.

[2] To calculate the temperature and stress/strain distributions in solidifying blocks under typical process conditions which have led to the formation of cracks.

[3] To understand the mechanism(s) of the crack formation based on the links between the model predictions and the occurrence of crack defects.

CHAPTER 4

INDUSTRIAL AND LABORATORY MEASUREMENTS

As mentioned earlier, in-mold temperature measurements were obtained from an industrial trial performed at Monofrax Inc. These thermocouple measurements serve to validate the heat transfer model as well as characterize the boundary conditions at the refractory/mold interface. In addition, experiments were conducted at ORNL to evaluate the inelastic behavior of the refractory at elevated temperatures and provide data for input to the mechanical model.

4.1 Industrial Measurements

To understand the solidification of the fused-cast αβ-alumina refractories, temperature data was obtained from thermocouples embedded at various locations in the molds employed in the Monofrax-M casting process. A pyrometer was employed to measure the pour stream as well as the surface temperature of the refractory block. In the same industrial study, chemical analysis was also performed in which both the pour stream and the block chemistries were evaluated. This section discusses the experimental techniques employed in the industrial study and the corresponding results.

4.1.1 Experimental Techniques

The Monofrax-M casting process can be divided into two regimes of behavior in terms of the heat transfer. Stage I cooling in the graphite mold, characterized by high cooling rates lasting a short duration; and Stage II cooling in the annealing ore, characterized by

relatively slow cooling rates extending over a long period of time (of the order of weeks). In the instrumented test casting, thermocouples were inserted into the graphite mold to record the variation in temperature with time during Stage I cooling and in the alumina ore to record the evolution in temperature during Stage II cooling in the bin.

For Stage I cooling, three thermocouples were placed in the graphite mold. The thermocouples were located adjacent to the center of the broad face of the block at a vertical height of 0.3556 m (14 inches), measured from the base of the block. One was located approximately at the casting/graphite interface and the other two were located in the graphite 0.0254 m (1 inch) and 0.0968 m (3.8125 inches) from the interface. The casting/graphite interface thermocouple was located at the center of the broad face and a Type-R (Platinum-13% Rhodium vs. Platinum) thermocouple was employed. The 0.0254-m (1-inch) and 0.0968-m (3.8125-inches) thermocouples were offset from the center toward the block narrow face by 0.0762 m (3 inches) and were Type-K (Nickel-Chromium vs. Nickel-Aluminum) thermocouples. In addition, a pyrometer was used to obtain an estimate of the pour stream as well as the block surface temperature. A two-color optical pyrometer was employed and calibrated at Monofrax Inc. The pyrometer was calibrated against heated samples of Monofrax-M of a known temperature.

For Stage II cooling, a total of 6 thermocouples were inserted in the alumina annealing ore. The thermocouples were located approximately at the casting/ore interface, and at 0.0508, 0.0523, 0.1016, 0.2032, and 0.2921 m (2, 2.06, 4, 8 and 11.5 inches) from the refractory/ore interface adjacent to the broad face of the block. The 0.0508 and 0.1016-m (2 and 4-inches) thermocouples were offset from the center of the broad face toward the narrow face by 0.0762 m (3 inches), whereas the 0.2032 and

0.2921-m (8 and 11.5-inches), and the 0.0523-m (2.06-inches) thermocouples were offset from the center by 0.1524 (6 inches) and 0.2286 m (9 inches), respectively. Type-B (Platinum-30% Rhodium vs. Platinum-6% Rhodium) thermocouples were used for the casting/ore interface, and 0.0508 and 0.0523 m (2 and 2.06 inches, respectively) from the interface. For the remaining locations, Type-K thermocouples were selected.

4.1.2 Results

The results obtained from the industrial trial are presented below in three subsections: initial conditions, thermal responses and post-cast refractory autopsy.

4.1.2.1 Initial Conditions

Based on the pyrometer measurements on the pour stream, the molten liquid temperature was approximately 2049°C, which serves as the initial condition for the block in the model. The ambient air temperature was roughly 25°C, which serves as the initial condition for the various components of the mold and the annealing bin (including the graphite, the silica annealing sand platform, the alumina annealing ore and the steel bin) used in the model.

During the 'pouring' of the molten alumina into the graphite mold, a small sample was taken for chemical analysis. The results showed that the pour stream chemistries contained approximately 94.5 weight % Al_2O_3, 4.2 weight % Na_2O and other minor oxides.

4.1.2.2 In-Mold Temperature Responses

Among the three thermocouples that were inserted into the graphite mold, the one located at 0.0968 m (3.8125 inches) from the casting/graphite interface failed completely. Figure 4.1 shows the thermocouple measurements obtained from the graphite mold during Stage I cooling along with the pyrometer data of the surface temperature of the casting. It should be noted that here and in the remaining plots to follow, the frequency of the measured data is adjusted to distinguish various curves in the plots. As can be seen in Figure 4.1, there is initially a gradual increase in the temperature for the first approximately 40 seconds followed by a relatively rapid increase associated with the liquid level reaching 0.3556 m (14 inches) height. The graphite temperature at the interface is observed to reach a peak temperature just in excess of 1000°C, whereas the surface of the block is between 1539 and 1737°C as recorded by the pyrometer. The greater scatter in the second set of pyrometer data shown in Figure 4.1 is a result of the motion of the casting and the difficulty of maintaining focus on the center of the broad face of the Monofrax-M crown block.

Unlike the transient Stage I cooling, Stage II cooling involves slower cooling rates over a longer time in the alumina ore annealing medium. Of the 6 thermocouples that were installed in the alumina ore, 1 failed completely and the thermocouples that were placed 0.0508 and 0.0523 m (2 and 2.06 inches) from the casting/ore interface produced similar results. Figure 4.2 presents the thermal response obtained from the thermocouples that were inserted 0.0508, 0.1016, 0.2032, and 0.2921 m (2, 4, 8 and 11.5 inches) from the interface.

4.1.2.3 Refractory Autopsy

The results of the refractory autopsy are illustrated schematically in Figures 4.3 and 4.4. As shown in Figure 4.3, the cracks are vertical and perpendicular to the broad face of the block. Tensile stresses acting parallel to the broad face (tensile stresses in direction-2) likely give rise to such cracks. Moreover, these cracks appear below the β-alumina region. For the horizontal plane just below the header, Figure 4.4 shows that the cracks appear to emanate from or terminate at the αβ/β-alumina interface. Furthermore, crack morphologies indicate that the cracks are intergranular and formed at elevated temperatures.

In addition to examining the crack defects found in the fused-cast αβ-alumina refractories, chemical analysis was also performed on the casting along the vertical centerline of the plane bisecting the broad face. In the analysis, the amount of Al_2O_3 and Na_2O was measured to determine the distribution of β-alumina within the block. Figure 4.5 presents the plot of the amount of β-alumina in mole % evaluated from the base to the top of the block. The data can be used in the model to distinguish between the αβ-alumina and the β-alumina regions.

4.2 Laboratory Measurements

As discussed earlier, an understanding of the high-temperature mechanical behavior of Monofrax-M is needed for the stress analysis. Four-point flexural tests were carried out at ORNL to evaluate the stress-strain behavior of the casting at elevated temperatures.

This section presents the experimental procedures used to perform the flexural tests and the corresponding results.

4.2.1 Experimental Procedures

The specimens used in the flexural tests at ORNL were machined from the same casting as the thermocouple trial discussed in Section 4.1.1. The nominal size of the rectangular specimens is 80 mm by 10 mm by 10 mm. The test frame for the flexural tests was comprised of components capable of operating at high temperatures and under either the load-control or displacement-control mode. The four-point bending tests in this study were performed using the displacement-control function owing to the need to examine the strain rate sensitive inelastic behavior of the material. The test conditions such as the strain rates or the displacement rates, as well as the temperatures, were selected based on the temperature evolution of the refractory predicted with the thermal model during casting.

Figure 4.6 shows the photograph of flexural test apparatus with the furnace opened. As can be seen, the load train consisted of a silicon carbon (SiC) load rod and a SiC support rod. During the experiments, the specimens were supported by the SiC fixtures. Figure 4.7 displays the configurations of the four-point bending tests on the Monofrax-M specimen with the SiC fixtures. Test temperatures were 1100, 1350, 1500, 1600, and 1700°C and test strain rates were $1x10^{-4}$, $1x10^{-5}$, $1x10^{-6}$, $5x10^{-7}$, and $2x10^{-7}$ s^{-1}. The strain rates that the casting experiences during Stage I cooling are covered by the test conditions whereas for Stage II cooling the strain rates are in the range of $1x10^{-7}$ to $2x10^{-9}$

s^{-1}. The limitation of strain rates for Stage II cooling is due to the flexural testing machine at ORNL, which is not capable of loading the system below $2x10^{-7}$ s^{-1}.

For each test, the experimental set-up was arranged as shown in Figures 4.6 and 4.7. Prior to commencing the test, the furnace was pre-heated to the selected temperatures for 30 to 90 minutes. After the temperature was stabilized, the specimen was loaded at a constant strain rate. The tests were conducted at a constant temperature and were terminated after the maximum force was reached. Results obtained from the experiments were the force and corresponding displacement. It should be noticed that the flexural test results also included displacements of the load train. As a result, flexural tests of SiC bend bar, which was made of the same material as the load train and same size as the Monofrax-M specimens, were also conducted at various test temperatures in order to make corrections to the displacements to reflect the actual displacements of the fused-cast alumina refractories.

4.2.2 Results

A total of 28 bending tests were carried out and the initial results were gathered in load-displacement format. As mentioned earlier, the displacements of the flexural tests on the Monofrax-M specimens consist of the displacements of both the testing samples and the SiC load train. Additional bending tests on SiC bend bar were conducted at all the test temperatures to evaluate the displacements of the load train. Corrections of the displacements were made using the relationship

$$\delta = \delta_{Monofrax\text{-}M + load\ train} - (\delta_{load\ train} - \delta_{SiC\ bend\ bar}) \qquad (4.1)$$

where, $\delta_{Monofrax\text{-}M\ +\ load\ train}$ was the displacement obtained from the flexural tests on the Monofrax-M specimens, $\delta_{load\ train}$ was the displacement gathered from the flexural tests on the SiC bend bar, and $\delta_{SiC\ bend\ bar}$ was the load-point displacement based on the elastic deflection of the SiC bend bar according to the following equation

$$\delta_{SiC\ bend\ bar} = \frac{Pa}{2Ebh^3}\left(3L^2 - 16a^2\right) \tag{4.2}$$

where, P is the applied load, a is the distance from the support to the load applicator when the specimen is straight, E is the modulus of the SiC bend bar, b is the specimen width, h is the specimen height, and L is the span length between the lower supports (refer to Figure 4.7) [21].

After the corrected displacements were evaluated using Equation 4.1, stress-strain behavior of Monofrax-M was calculated based on the corresponding load-point displacement and applied load. The stress and strain calculations shown in the following equations were derived based on simple beam theory assuming that the material is isotropic and homogeneous, the moduli of elasticity in tension and compression are identical, and the material is linearly elastic [21-22]

$$\sigma = \frac{3}{2}\frac{P}{bh^2}(L-U) \tag{4.3}$$

$$\varepsilon = \frac{3}{2}\frac{h}{a}\delta\frac{1}{3L-4a} \tag{4.4}$$

where, U is the span length between the upper supports, ε is the outer-fiber tensile strain and δ is the corrected load-point displacement computed based on Equation 4.1.

The resulted stress-strain curves of Monofrax-M at various strain rates and temperatures are displayed in Figures 4.8 - 4.16. As a comparison, the plots also include

the elastic response of the refractory based on the interpolated values of the elastic modulus measured acoustically at various temperatures at United Technologies Research Center [23].

Figures 4.8 to 4.10 show the stress-strain response at 1100°C and indicate that the material exhibits largely elastic behavior up to the maximum stress. This is evident since the slopes on loading are in reasonable agreement with the stress-strain response based on perfectly elastic behavior using the measured elastic modulus. The departure from linearity that is observed near the peak stress likely reflects micro-cracking and damage accumulation and not significant plastic or creep deformation. Hence, the behavior at 1100°C may be assumed to be perfectly elastic up to a failure load or between roughly 12 and 17 MPa. It should be noticed that the unreasonable behavior of Sample 2-8 in Figure 4.10 could be attributed to experimental artifacts such as thermal instability, poor articulation, and wedging.

At higher temperatures, it can be seen from Figures 4.11 to 4.16 that the stress-strain curves deviate from the elastic behavior or linearity well before the maximum stresses have been attained indicating plastic or creep deformation. Thus, at some temperature between 1100 and 1350°C inelastic deformation mechanisms become important.

The results for the different strain rates tests at 1350°C indicate little sensitivity to strain rate. However, for the sample tests at 1500°C and above, this is not the case and the stress-strain response is sensitive to the deformation rate. At higher strain rates, the material is generally 'stiffer' as would be expected.

Overall, the stress-strain or constitutive behavior of Monofrax-M over the range of temperatures experienced in the casting process is complex, exhibiting at elevated temperature, strain rate sensitive inelastic behavior. The approach adopted in the stress analysis is to greatly simplify this behavior by assuming that the αβ-alumina is an elastic-plastic material that does not exhibit any strain rate sensitivity. To prepare that data for input to ABAQUS (to be discussed later in Chapter 6), the stress-strain data was further processed.

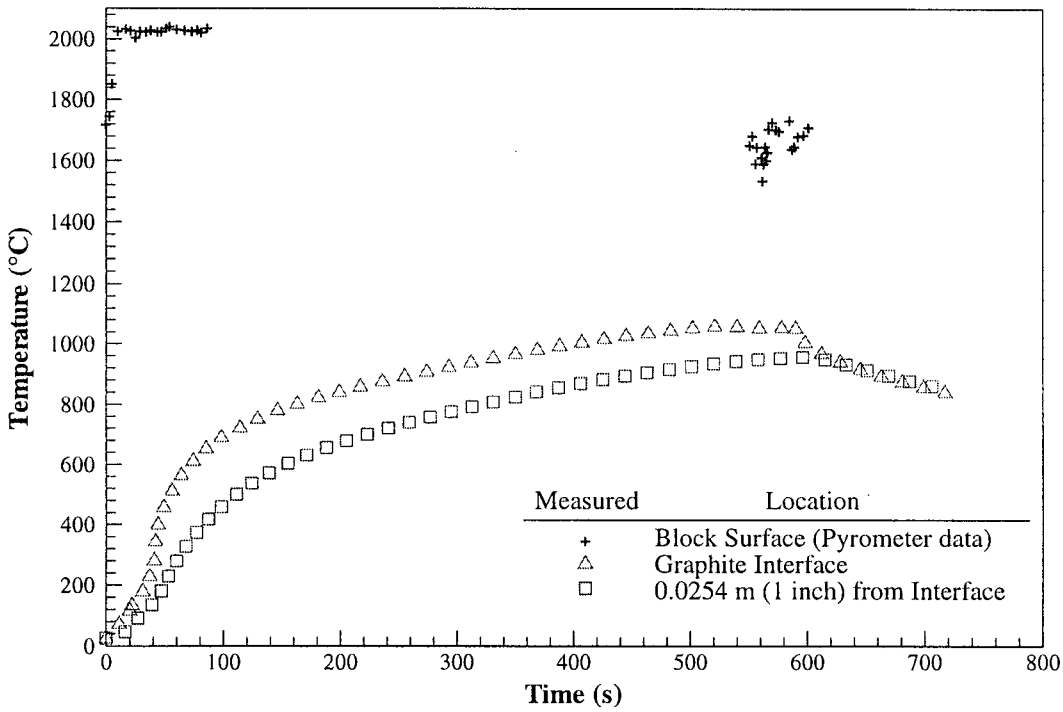

Figure 4.1 – Thermocouple measurements and pyrometer data from Monofrax-M industrial trial for Stage I cooling in the graphite mold.

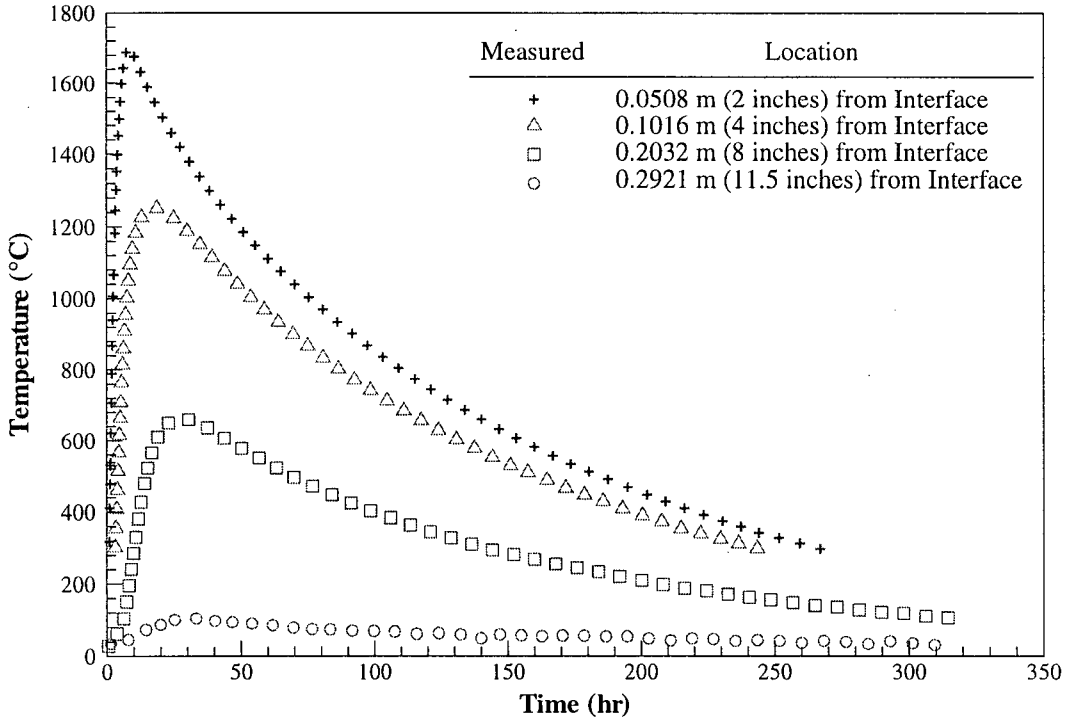

Figure 4.2 – Thermal response obtained from Monofrax-M industrial trial for Stage II cooling in the alumina ore.

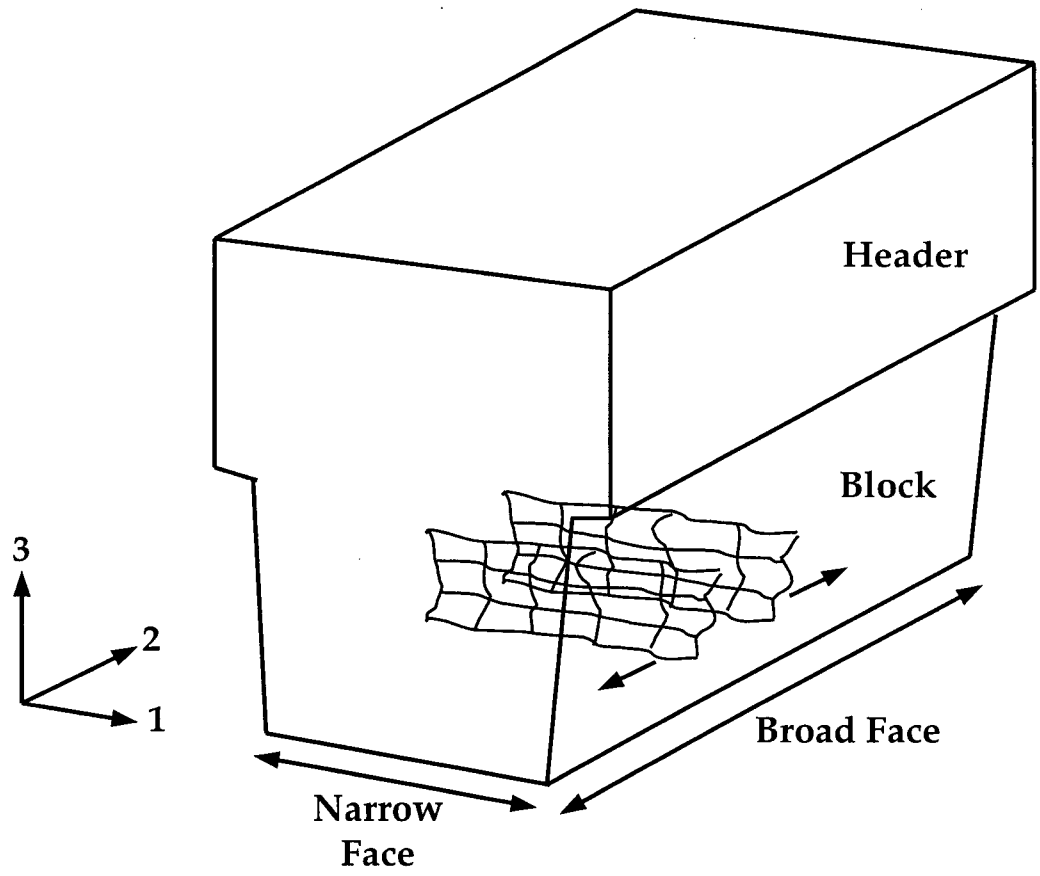

Figure 4.3 – Schematic illustration of typical cracks found in Monofrax-M (not to scale).

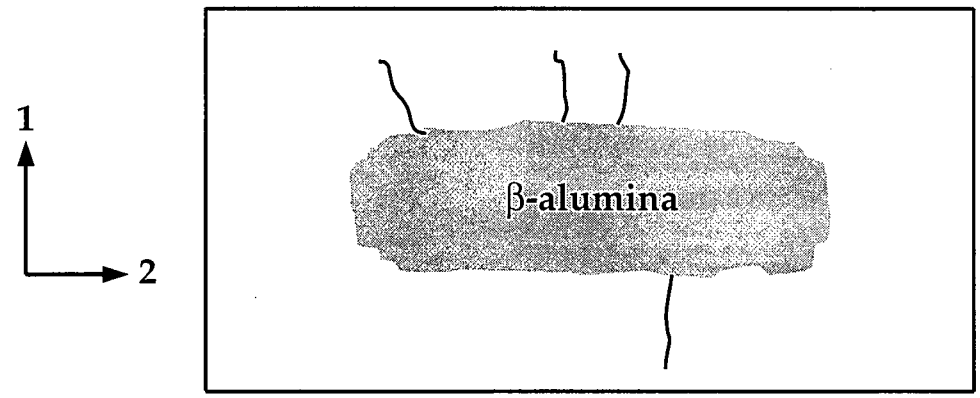

Figure 4.4 – Schematic illustration of typical cracks found in Monofrax-M at the horizontal plane just below the header (not to scale).

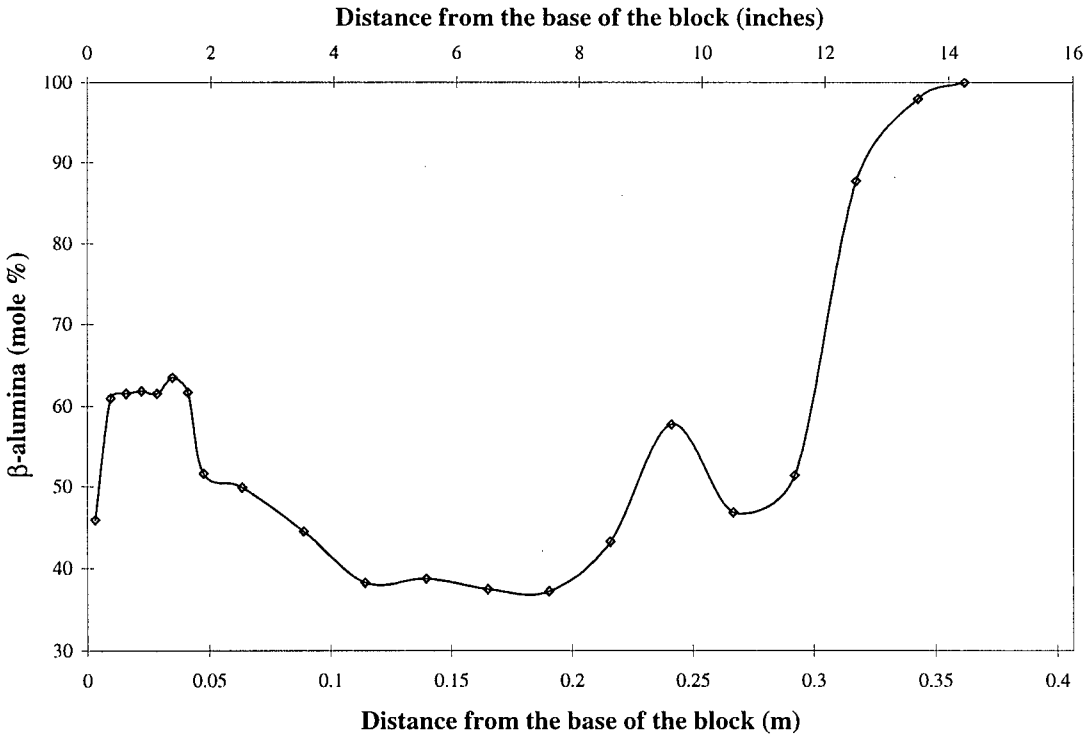

Figure 4.5 – Chemical analysis results obtained from Monofrax-M crown block measured at the vertical centerline of the plane bisecting the broad face of the casting.

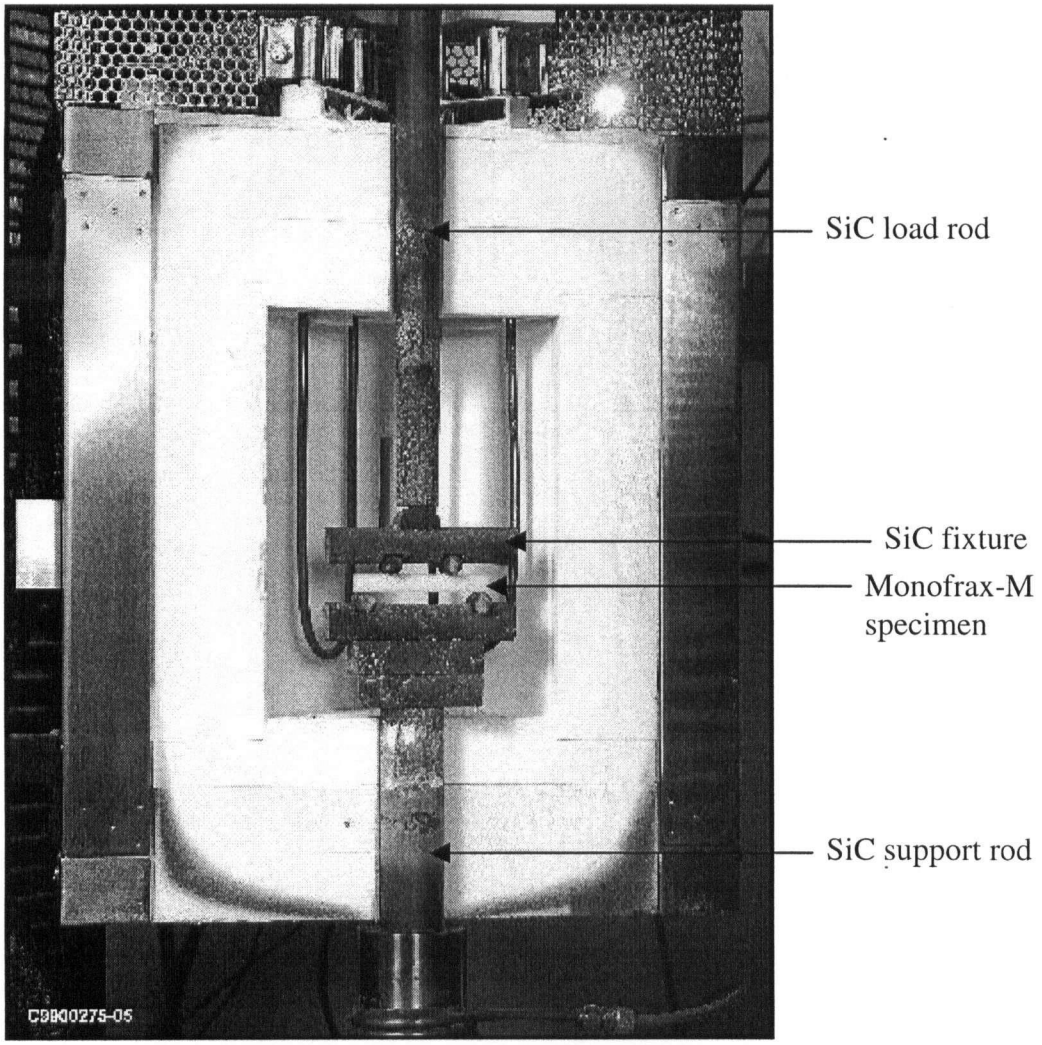

Figure 4.6 – Photograph of flexural apparatus with the furnace opened.

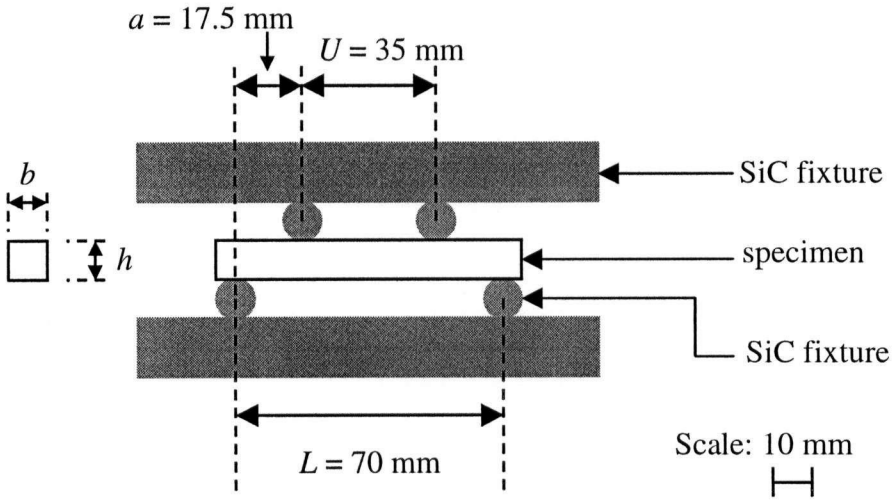

Figure 4.7 – Schematic of the configurations of the flexural tests performed at ORNL.

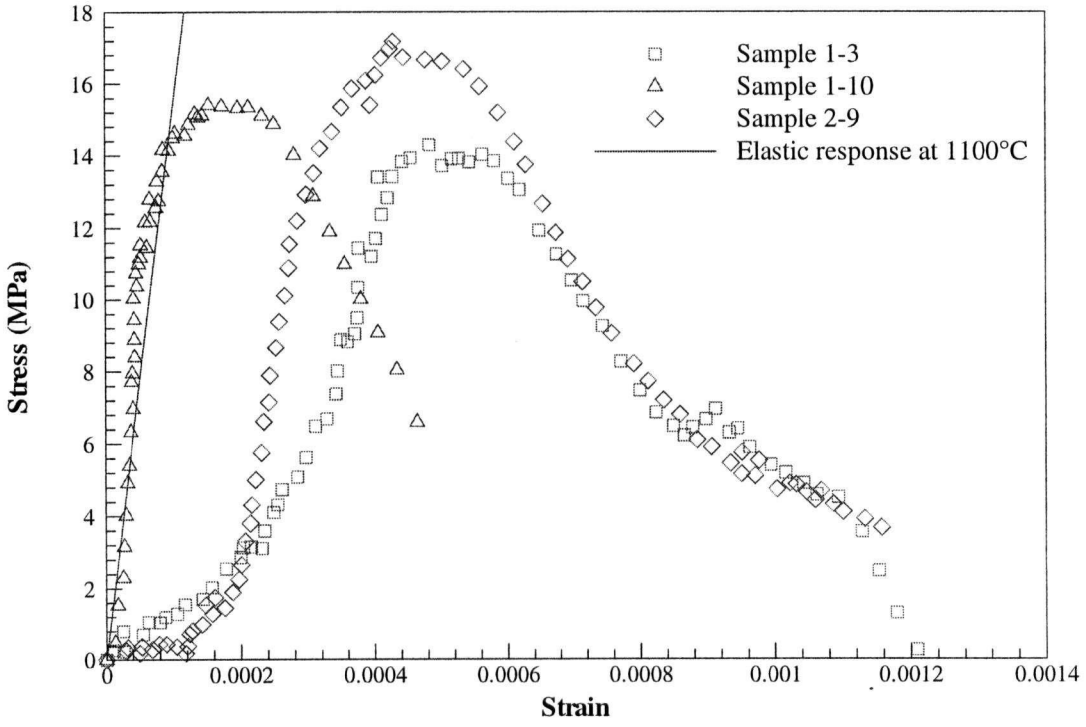

Figure 4.8 – Stress-strain curve of Monofrax-M specimens at 1100°C at a strain rate of $1x10^{-6}$ s^{-1}.

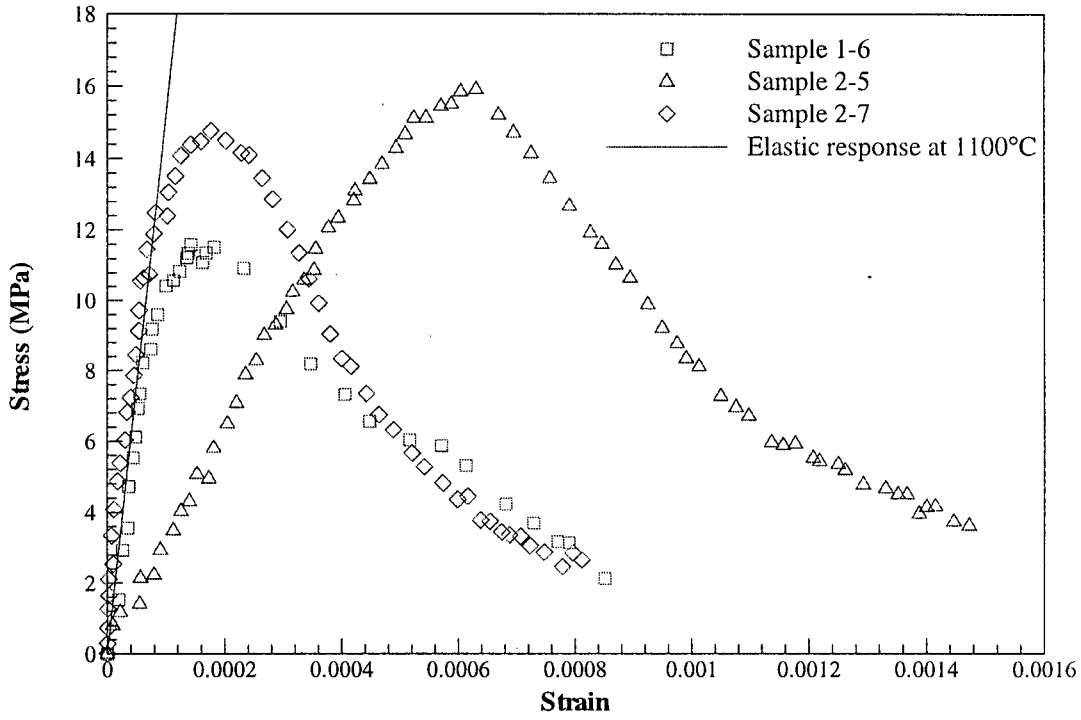

Figure 4.9 – Stress-strain curve of Monofrax-M specimens at 1100°C at a strain rate of $5x10^{-7}$ s^{-1}.

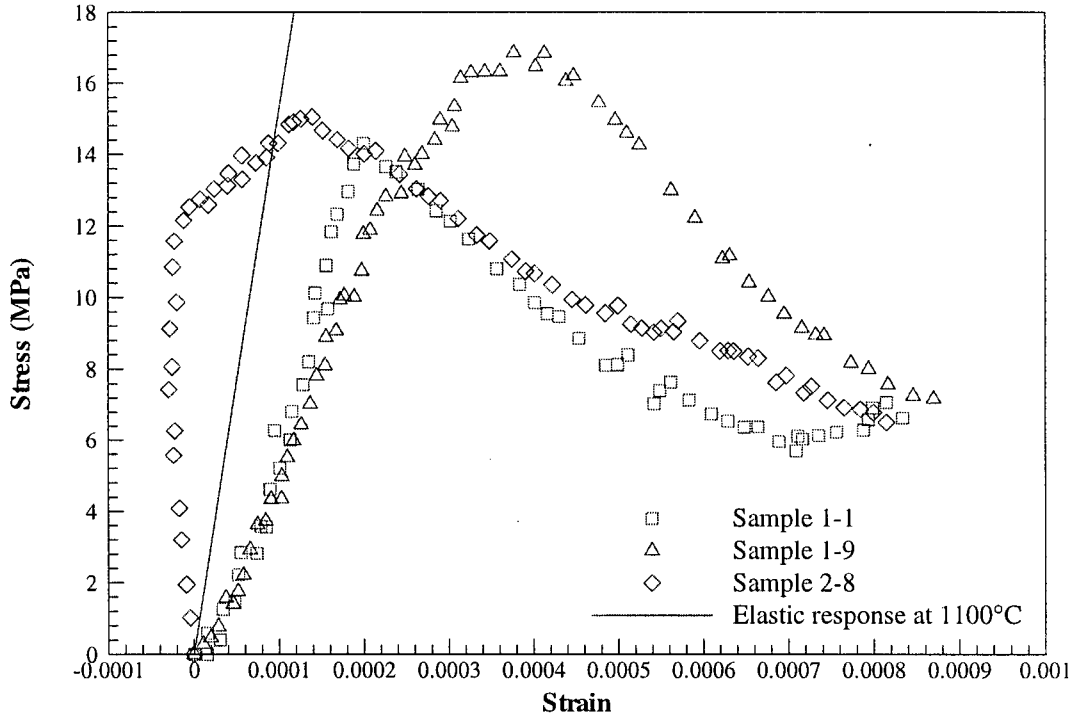

Figure 4.10 – Stress-strain curve of Monofrax-M specimens at 1100°C at a strain rate of $2x10^{-7}$ s^{-1}.

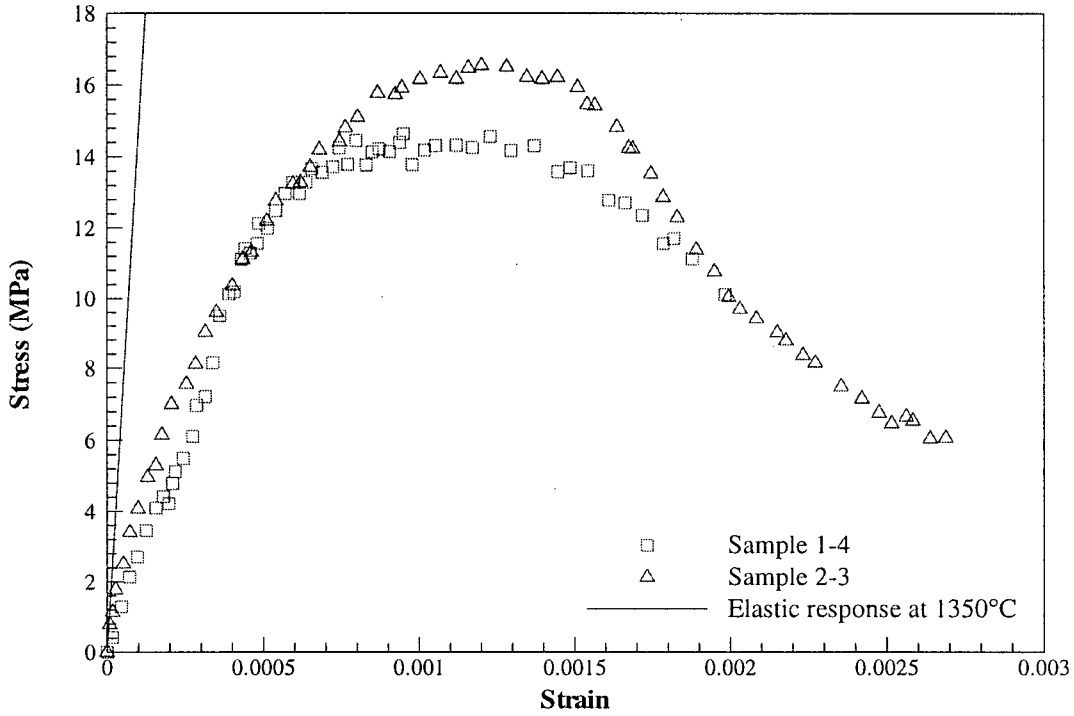

Figure 4.11 – Stress-strain curve of Monofrax-M specimens at 1350°C at a strain rate of $1x10^{-6}$ s^{-1}.

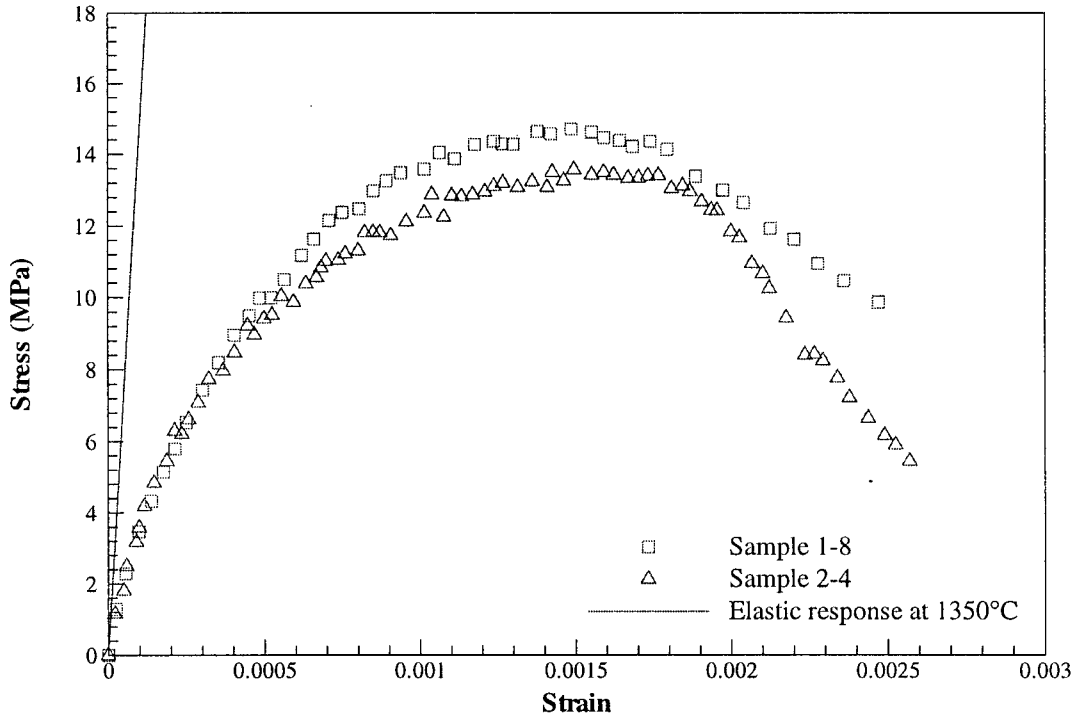

Figure 4.12 – Stress-strain curve of Monofrax-M specimens at 1350°C at a strain rate of $5x10^{-7}$ s^{-1}.

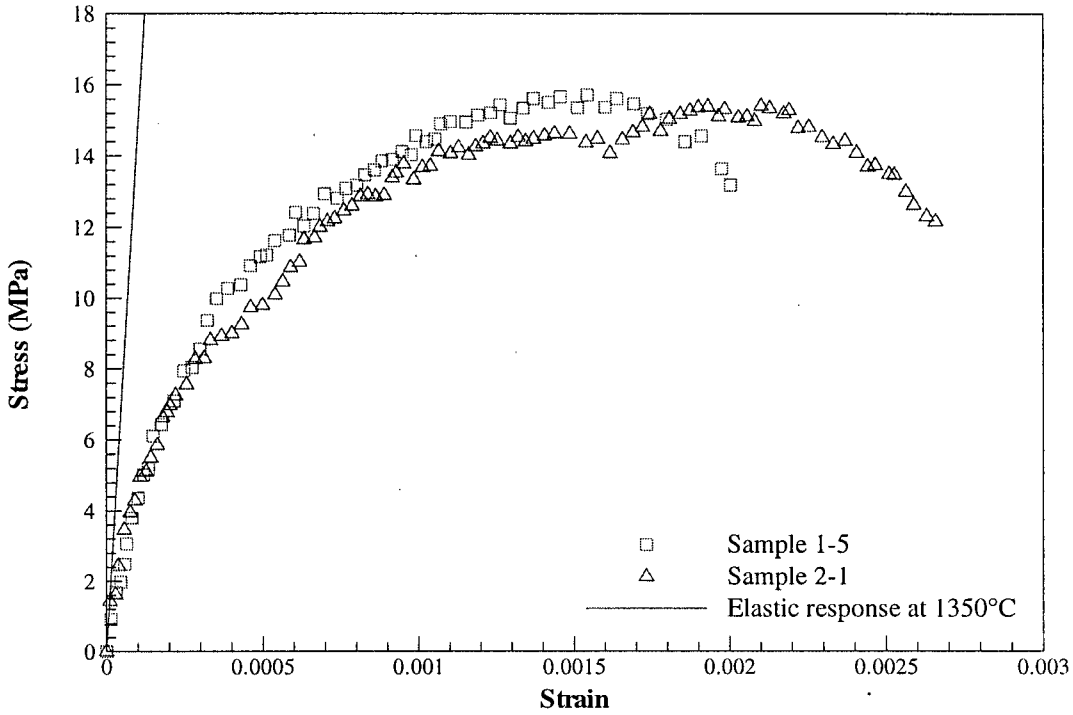

Figure 4.13 – Stress-strain curve of Monofrax-M specimens at 1350°C at a strain rate of $2x10^{-7}$ s^{-1}.

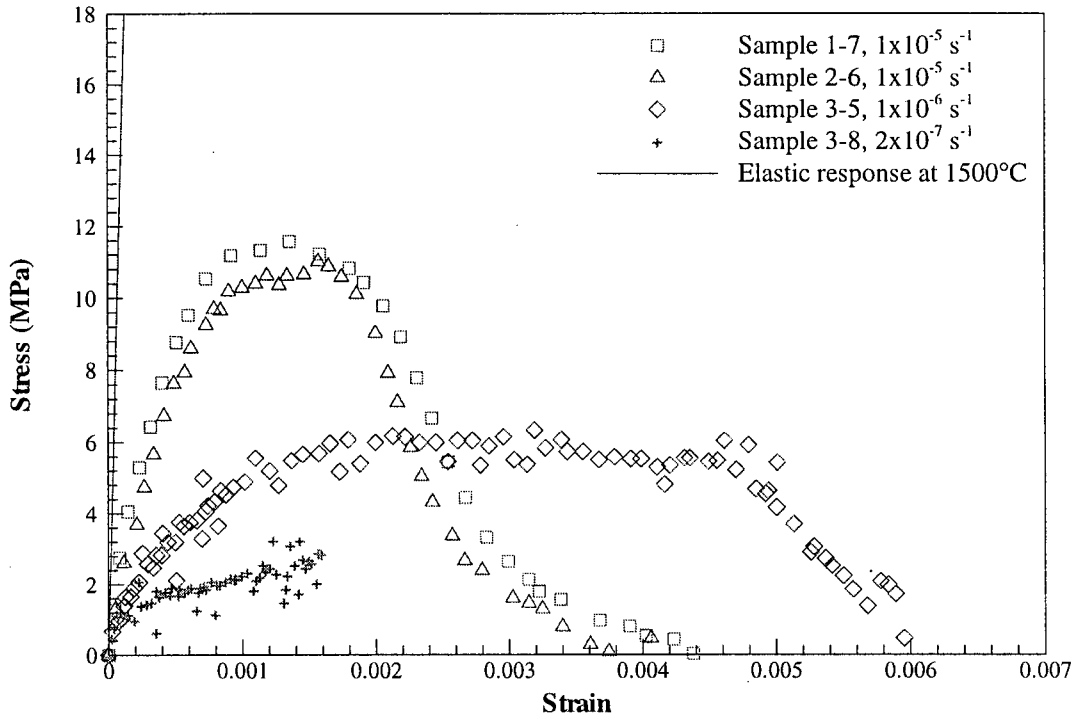

Figure 4.14 – Stress-strain curve of Monofrax-M specimens at 1500°C at various strain rates.

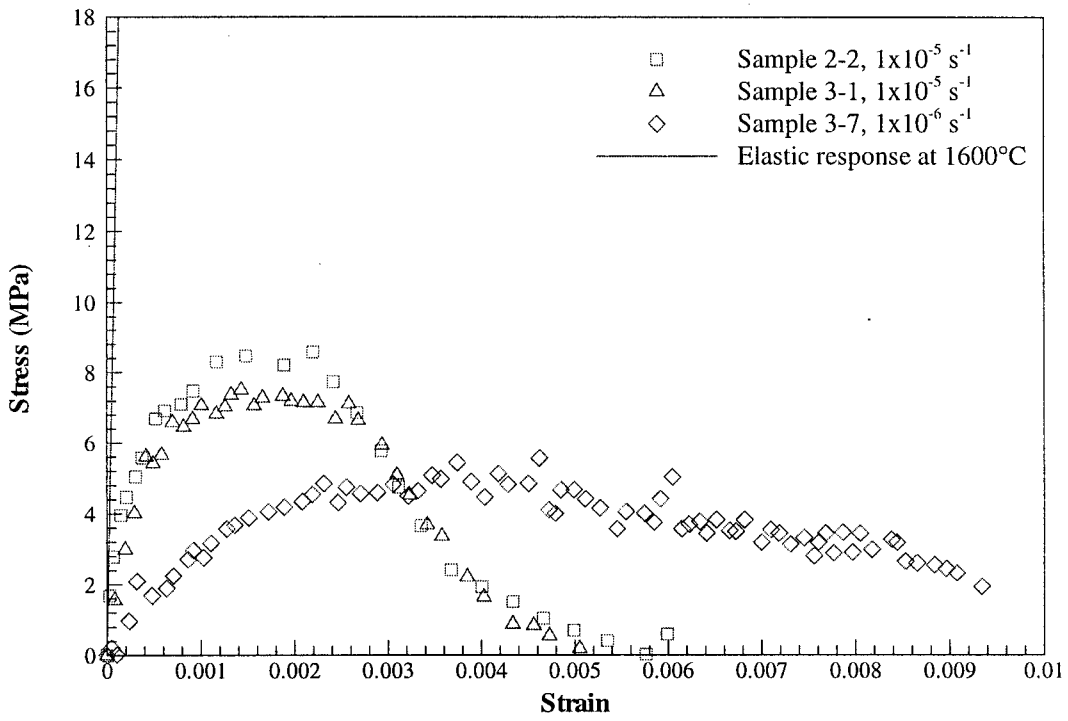

Figure 4.15 – Stress-strain curve of Monofrax-M specimens at 1600°C at various strain rates.

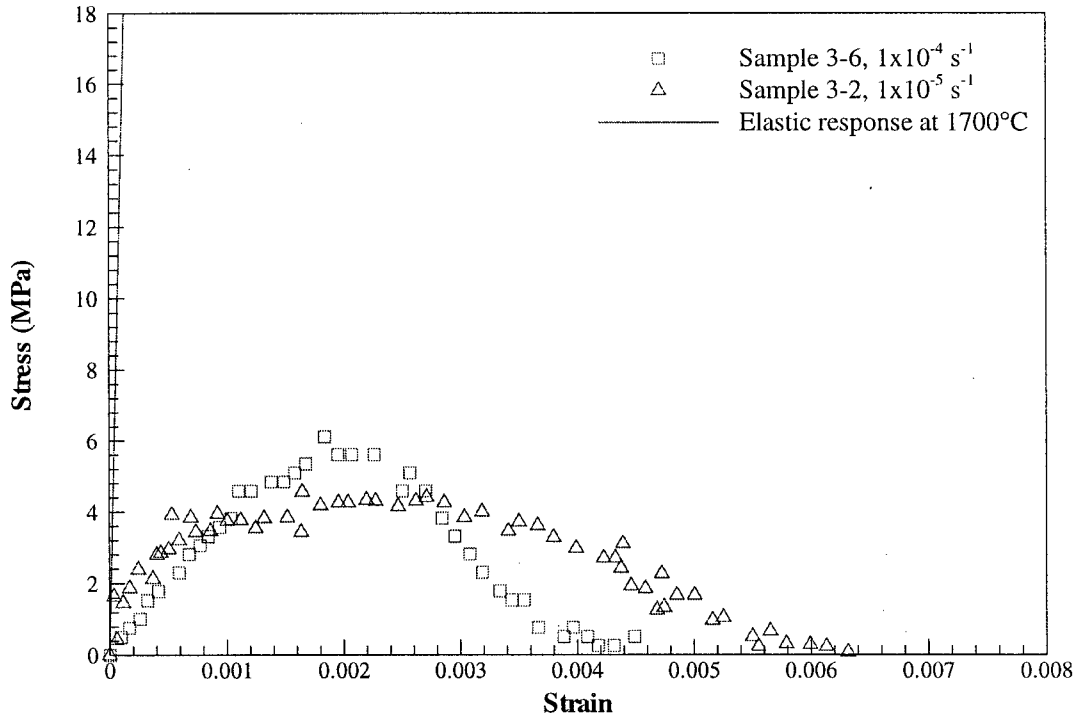

Figure 4.16 – Stress-strain curve of Monofrax-M specimens at 1700°C at various strain rates.

CHAPTER 5

THERMAL MODEL

Based on the modeling work reviewed in Chapter 2, the finite element method seems best suited to develop a mathematical model capable of predicting the evolution of temperature, stress and strain in a Monofrax-M crown block casting [4-12]. The approach adopted in the present study is a thermal analysis followed by an un-coupled elastic-plastic stress analysis similar to that applied by Jeanmart and Bouvaist [5] on an aluminum alloy and Lu et al. [12] on fused-cast AZS refractories. The commercial finite element package ABAQUS has been used to develop the thermal model and the thermal-stress (mechanical) model of the crown block. This section focuses on the development of the thermal model, and its validation.

5.1 General Thermal Model Formulation

Due to the time-dependent nature of the Monofrax-M casting process, the heat transfer model of the Monofrax-M crown block must be transient and must also account for the variation in temperature with time in the molding materials including the graphite mold, the silica annealing sand platform (on which the graphite mold was placed), the alumina ore, and the steel bin. In the thermal model, the governing partial differential equation is shown in Equation 5.1

$$\rho C_p(T)\frac{\partial T}{\partial t} = \nabla[k(T)\nabla T] + \dot{Q} \qquad (5.1)$$

where, ρ is the density, C_p is the specific heat, T is the temperature, k is the thermal conductivity, and $\dot{Q}$ is a volumetric source term associated with latent heat evolution.

Fluid flow in the liquid during filling of the mold and during the early stages of the casting process has been ignored and heat is assumed to be transferred by diffusion only. Temperature dependencies in the specific heat and thermal conductivity of the materials present have been included to the extent to which they are available. The density has been assumed to be temperature independent to conserve mass with a fixed mesh. Latent heat evolution associated with the solidification of the α/β alumina has been included. The casting and the molding materials have been assumed to exhibit isotropic behavior.

5.2 Geometry

As previously mentioned, the geometric aspects of the casting process dictate a three-dimensional analysis. In addition, the simulation of the Monofrax-M casting process requires the removal and addition of different mold materials during the various stages of the process. The various changes to geometry and the associated load steps utilized in the model to simulate the casting process are presented in Table 5.1.

In Stage I cooling, the model geometry encompasses the crown block, graphite mold and silica annealing sand platform. Four-fold symmetry in heat flow about the vertical center planes bisecting the broad and narrow faces can be assumed during Stage I cooling. Likewise, under ideal conditions, the block would be expected to be centrally located in the bin, and four-fold symmetry in the flow of heat would also be expected in Stage II cooling. The original model developed in the present study took advantage of this symmetry and analyzed only ¼ section of the crown block, Stage I mold and Stage II annealing bin. However, numerous runs with the ¼ section model failed to obtain

agreement between the predictions and the measured data taken from thermocouples located in the annealing ore. On close inspection of the bin geometry, it was realized that the crown block was not placed inside the annealing bin symmetrically. At a height of 0.3556 m (14 inches) up the block face (measured from the block bottom), it was found that there was approximately 0.2921 m (11.5 inches) of alumina ore adjacent to one side of the broad face and roughly 0.4128 m (16.25 inches) of alumina ore on the other. Adjacent to the narrow face, the asymmetry was less, with approximately 0.2616 m (10.3 inches) and 0.2350 m (9.25 inches) of alumina ore on either side of the bin. As a result, it was necessary to adopt only two-fold symmetry in heat transfer about a vertical center plane bisecting the broad face of the block. Thus, both Stage I and II geometry in the final model adopted only two-fold symmetry.

First-order, 8-node brick linear heat transfer elements (ABAQUS designation DC3D8) were employed in the current research. The resulting three-dimensional mesh employed in Stages I and II contained a total of 45619 elements comprising 54003 nodes. Of these, 6400 elements and 7497 nodes were located in the block. Figure 5.1 shows the Monofrax-M crown block mesh adopted for the thermal model. Figure 5.2 shows the mesh utilized for the graphite mold and the silica annealing sand platform in Stage I cooling and Figure 5.3 shows the mesh used for Stage II cooling in the annealing bin. The inclusion of the steel flasking segments and fins in the Stage II mesh was determined to be necessary as they were determined to have a small but not insignificant effect on block cooling.

5.3 Boundary Conditions

A key aspect in the development of the thermal model is characterization of the thermal boundary conditions, which govern the flow of heat between the various components in the mold and to the surrounding environment. Moving from the crown block outward, heat is transferred between the block and the graphite mold (Stage I) and annealing ore (Stage II) via a combination of contact conduction and radiation. Between the ore and steel flasking, heat is assumed to flow without any interface resistance. At the graphite mold exterior (Stage I) and flasking exterior (Stage II), heat transferred to the surrounding environment by a combination of natural convection and radiation.

5.3.1 Symmetry Boundaries

As previously outlined, conditions of symmetry have been applied with respect to heat flow perpendicular to a vertical plane bisecting the center of the broad face. Along this plane, a zero heat-flow, or adiabatic boundary condition has been applied, as in Equation 5.2

$$q = -k\frac{\partial T}{\partial n} = 0 \; for \; t > 0 \qquad (5.2)$$

where, q is the heat flux in Wm^{-2}, k is the thermal conductivity in $Wm^{-1}K^{-1}$, T is the temperature in K, n is the normal to surface direction and t is the time in seconds.

5.3.2 Casting-Mold Boundary

At the interface between the casting and the mold(s) (graphite in Stage I cooling and alumina ore in Stage II cooling), heat transfer is described by a Cauchy type boundary

condition. Across the interface, heat is transferred by a combination of contact conduction and radiation. Initially, contact conduction dominates and the rate of heat transport is high. As time proceeds, a gap is formed between the casting and the mold leading to a gradual decrease in contact conduction, a gradual increase in the radiation component and an overall reduction in heat transfer between the two surfaces. Equation (5.3) has been used in ABAQUS to quantify heat transfer at the interface.

$$\text{Gap Conductance} = f_c h_c + (1 - f_c) h_{rad} \tag{5.3}$$

In Equation 5.3, f_c is the fraction of contact between the two surfaces, h_c is the heat transfer coefficient due to contact conduction in $Wm^{-2}K^{-1}$, and h_{rad} is the effective heat transfer coefficient due to radiation in $Wm^{-2}K^{-1}$.

To account for gap formation, f_c was calculated based on the following expression:

$$f_c = \frac{-0.8}{t_{elapsed}} t + 1 \tag{5.4}$$

where, $t_{elapsed}$ is the elapsed time, or duration, of Stage I or II cooling, t is the current total model time, f_c = 1 at the beginning of Stage I or II cooling, and f_c = 0.2 at the end of Stage I and II cooling.

The radiative component of heat transfer, quantified by the effective heat transfer coefficient, h_{rad}, was calculated as follows:

$$h_{rad} = \sigma \varepsilon \frac{T_1^4 - T_2^4}{T_1 - T_2} \tag{5.5}$$

where, σ is the Stefan-Boltzmann constant (5.67×10^{-8} $Wm^{-2}K^{-4}$), ε is the effective emissivity, T_1 is the temperature of the casting in Kelvin and T_2 is the temperature of the

mold in Kelvin at the location being processed. The effective emissivity is a function of the emissivities of both the casting and the mold as given below in Equation (5.6)

$$\varepsilon = \frac{1}{\frac{1}{\varepsilon_1} + \frac{1}{\varepsilon_2} - 1} \tag{5.6}$$

where, ε_1 is the emissivity of Monofrax-M as a function of temperature and ε_2 is the emissivity of the mold.

5.3.3 Mold Exterior Boundary

Heat transfer from the mold exterior to its surroundings occurs by a combination of natural convection and radiation. The natural convection component is characterized by a Cauchy type boundary condition. The heat transfer coefficient for natural convection calculated for the mold exterior has been determined to be approximately 6 $Wm^{-2}K^{-1}$, based on an empirical expression for free-convection for vertical plates [24]. For the radiation component, a boundary radiation was prescribed in ABAQUS and the heat flux across the surface of the mold was evaluated as in Equation 5.7

$$q = \sigma\varepsilon\left(T_s^4 - T_a^4\right) \tag{5.7}$$

where, σ is the Stefan-Boltzmann constant, ε is the emissivity of the mold, T_s is the temperature of the casting surface in Kelvin and T_a is the ambient temperature in Kelvin.

5.4 Initial Conditions

The initial temperature of the casting was set to 2049°C, the approximate pour stream temperature measured at Monofrax Inc. The various components of the mold and

annealing bin (including the graphite, the silica sand, the alumina ore and the steel bin) were initially assumed to be at a uniform temperature of 25°C.

5.5 Thermo-Physical Properties

The thermo-physical data needed for Monofrax-M and the molding materials was obtained from various sources including Monofrax Inc., Virginia Polytechnic Institute, Orton Refractory Testing and Research Center, ORNL, and the Metals Handbook [2, 25-28] and is summarized in Tables 5.2 to 5.4. Because the behavior of these materials is modeled over a large range of temperature (25 - 2049°C), temperature dependencies must be accounted for in the thermal model. This has been done to the extent possible with the available data. In some cases, to be discussed below, it has been necessary to extrapolate this data beyond the upper limit in the empirical data.

The volumetric latent heat of fusion is another thermo-physical data that is required in the heat transfer model when phase transformations are involved. As discussed in Chapter 2.5, the liquidus and solidus of Monofrax-M were found to be 2026°C and 2000°C, respectively, assuming equilibrium solidification. In the thermal model, latent heat of 1089506 J kg^{-1} (111.086 kJ mol^{-1}, [20]) was released linearly between the transformation start and finish temperatures, 2026°C and 2000°C, respectively. In addition, a sensitivity analysis was performed to investigate the effect of releasing the latent heat non-linearly according to a more realistic solidification path.

5.6 Thermal Predictions and Comparisons to Measured Data

During solidification, the Monofrax-M crown block is subject to a broad range of cooling conditions. To validate the thermal model, thermocouple data has been obtained at Monofrax Inc. for both Stage I and Stage II cooling as discussed in Chapter 4.1.

5.6.1 Stage I – Graphite Cooling Model

A base-case FEM thermal model was developed and run prior to conducting an investigation of model sensitivity to variations in some of the key input parameters and formulation assumptions. The following conditions were adopted in the base-case model:

- The heat transfer coefficient due to contact conduction, h_c in Equation 5.3, was assumed to be 1000 $Wm^{-2}K^{-1}$.
- The fraction of contact between the refractory and the mold, f_c, was evaluated as in Equation 5.4.
- The Virginia Polytechnic Institute thermal conductivity data has been used and has been linearly extrapolated to the pour temperature. (Note: as both sets of measurements in Table 5.2 indicate a general trend to increasing conductivity at elevated temperature (refer to Figure 5.4), the trend in empirical conductivity data was used as basis for extrapolation. Moreover, according to Monofrax-M personnel [2], the thermal conductivity data obtained by laser flash tends to be more reliable than that by calorimeter.)

The temperature predictions obtained from the base-case thermal model are presented together with the thermocouple data in Figure 5.5. As can be seen, the agreement is poor. One obvious problem with the base-case model is that the model

predicts an initial rate of temperature increase that is too high. In the thermal model, the mold is assumed to be filled instantaneously, whereas in the process this takes a finite amount of time. Hence, the model initially over-predicts the heat transfer to the mold at the height of the thermocouples.

A second obvious shortcoming of the model is that the peak temperatures obtained in the mold are too low. An extensive parameter investigation with the model encompassing 18 runs, revealed that this problem was related to a failure to transfer enough heat from within the block to the block/mold interface, which is controlled principally by the thermal conductivity of Monofrax-M.

As can be seen in Figure 5.4, the laser flash data is relatively low at the upper range of temperature required in the model whereas the calorimeter data leads to comparatively high conductivities at the same range. In an attempt to improve model agreement, the average of the regression lines obtained from both data was adopted. In addition, the conductivity of Monofrax M at 2026°C was increased above the value obtained from extrapolation at 2000°C to take into account the effect of convective heat transport in the liquid pool. This is a common approximation used in the simulation of heat transfer in the liquid phase in casting processes and involves the use of a Liquid Conductivity Multiplication Factor (LCMF) [29].

The model was also found to be quite sensitive to the parameters quantifying casting/mold interface heat transfer – i.e. the gap conductance defined in Equation 5.3 and f_c in Equation 5.4.. To 'fine-tune' the thermal model, the two parameters were varied in a series of runs. The 'best' results appear to have been achieved with h_c set to 600 $Wm^{-2}K^{-1}$ and f_c evaluated based on Equation 5.8

$$f_c = \frac{-0.6}{t_{elapsed}} t + 1 \qquad (5.8)$$

where, f_c = 1 at the beginning of Stage I cooling, and f_c = 0.4 at the end of Stage I cooling.

Figure 5.6 shows the model results obtained with the modified Monofrax-M thermal conductivity with an LCMF of 4 and the modified h_c and f_c. As can be seen from the comparison, the results of the thermal model are now in relatively good agreement with the thermocouple data. The temperature predictions of the block surface are also improved, but remain too low (assuming the pyrometer data is correct).

Finally, a sensitivity analysis was conducted to assess the influence of rate of volumetric latent heat release on the temperature predictions. In contrast to a linear release of latent heat, assumed in the base-case model, the phase diagram indicates that approximately 38% of the latent heat should be released from 2026°C to 2002°C and the balance from 2002°C to 2000°C. Figure 5.7 compares the thermocouple measurements with the results obtained from the thermal model using the more correct solidification path. As can be seen in the figure, the revised model predictions deviate further from the measured data. It is believed that the thermal conductivity could be further adjusted to refit the heat transfer model. However, since accounting for the non-linear heat release doubles the computational time from 19 hours to 40 hours, it was felt that this change to the model was not justified. As a result, the current thermal model assumes linear release of latent heat. Future work should be performed to better reflect the nature of the solidification path of Monofrax-M.

5.6.2 Stage II – Alumina Ore Cooling Model

During Stage II cooling, the alumina ore represents the major resistance to heat transfer. Thus, factors that influence the conductivity of the ore are likely to have a significant impact on the predictions of the model – such as for example, process variability in the ore composition, different ore sources (suppliers) and extended exposure of the ore to high temperatures near the block face (sintering).

Prior to conducting a sensitivity analysis, a base-case model was run to serve as a benchmark for comparison. The base-case model used the thermo-physical properties for system alumina ore with a density of 1270 kg m^{-3} (79.3 pcf), which is consistent with the ore used in the instrumented test casting. In addition, it has been observed that approximately 0.0381 m (1.5 inches) of ore is 'hard' sintered immediately next to the surface of Monofrax-M crown block and another 0.0381 m (1.5 inches) of ore is 'weakly' or soft sintered adjacent to hard sintered ore (measured at the center of the broad face). Table 5.5 compares the measured thermal conductivity values for the various states of alumina ore. As can be seen, the thermal conductivity data of both hard and soft sintered ores is much higher than the system ore. Thus, sintering in the bin adjacent to the block face may be expected to have a significant effect on heat transport. Initially, however, no sintering behavior was incorporated in the base-case model, so that the effect of ore sintering could be assessed.

Figure 5.8 shows a comparison between the results obtained from the base-case thermal model and the thermocouple measurements during Stage II cooling. The model results were obtained at the corresponding thermocouple locations to within the limits in mesh resolution. As can be seen, the model predictions were in good agreement with the

thermocouple measurements. The peak temperature predicted at 0.0508 m (2 inches) from the refractory/ore interface, however, was slightly too low.

An important point to make is that the temperature predictions are very sensitive to thermocouple location. Figure 5.9 shows the model results obtained at locations 0.0254, 0.0762, 0.1524, and 0.2540 m (1, 3, 6 and 10 inches) from the refractory/ore interface. As can be seen, the peak temperature obtained from the thermocouple at 0.0508 m (2 inches) from the interface lies between the predicted peak temperatures at 0.0254 and 0.0508 m (1 and 2 inches) from the interface. Thus, any error in the location of the thermocouple will substantially alter the result. As errors of the order of ±0.0127 m (±0.5 inches) in the location of the thermocouples could be expected, the fit presented in Figure 5.9 seems reasonable.

In view of the sintering occurring in the ore and its effect on conductivity, the next step was to introduce this into the model. The sintering behavior in the ore is introduced into ABAQUS through a subroutine called *ufield* in which a field variable, f_s, can be defined reflecting the fraction, or degree, to which the ore is sintered. In the present model, when $f_s = 1$, the properties of the hard sintered ore are used, when $f_s = 0.5$, the properties of the weakly sintered ore are used, and when $f_s = 0$, the properties of the system alumina ore are used. The fraction of alumina ore sintered is calculated based on the peak temperature the ore experiences at a particular location in the bin. The criteria adopted uses 3 threshold temperatures as given in Equation 5.9

$$f_s = \begin{cases} 0 \text{ if } T < T_{th} \\ 0.5\left(\dfrac{T - T_{th}}{T_s - T_{th}}\right) + 0.5 \text{ if } T_{th} < T < T_s \\ 0.5\left(\dfrac{T - T_s}{T_h - T_s}\right) \text{ if } T_s < T < T_h \\ 1 \text{ if } T > T_h \end{cases} \tag{5.9}$$

where, T is the current temperature of the alumina ore (evaluated at each material integration point temperature within an element), T_{th} is the threshold temperature below which sintering does not occur, T_s is the temperature above which the alumina ore becomes weakly sintered and T_h is the temperature above which the alumina ore becomes hard sintered. Linear interpolation is used for temperatures between the threshold temperatures.

The temperatures, T_{th}, T_s, and T_h, were determined through trial and error to be 500, 1700 and 1900°C, respectively. Using these values, ~0.0381 m (~1.5 inches) of hard sintered ore was predicted to form next to the block surface at the center of the broad face and ~0.0381 m (~1.5 inches) of weakly sintered ore was predicted adjacent to the hard sintered ore. Figure 5.10 shows a comparison between the model results using sintering and the thermocouple measurements. As can be seen, the agreement for the peak temperatures at the various thermocouple locations are if anything worse. Figure 5.11 presents the contour plot of the fraction of alumina ore sintered at the end of the casting process. As can be seen, there is considerable variability in the amount (thickness) of material sintered, as would be expected based on variability in peak temperatures obtained at the various locations within the bin.

A sensitivity analysis was also conducted on parameters controlling heat transfer from the exterior steel bin to the environment and across the interface between the

refractory and the alumina ore. Varying these parameters within the model failed to improve agreement and decrease the peak temperatures predicted by the model.

One possible explanation for the excess peak temperature is that the sintering actually occurs over time rather than instantaneously at a given temperature, as was the case in the preliminary sintering model. To explore this, a second parameter, f_t, could be introduced into the sintering model to affect a time delay in sintering. Delaying sintering could have the desired effect of initially reducing conductive heat transfer close to the block face resulting in a decrease in the peak temperatures predicted by the model. It has been found, in general, that decreasing the amount of ore sintered had the effect of improving the agreement between the model and the measured temperature response.

As a result, it is observed that although a sintering algorithm was introduced to account for the increase in conductivity due to densification of ore on exposure to elevated temperature in the bin, optimal agreement was achieved with the sintering algorithm switched off.

In addition, similar to Stage I cooling, the influence of latent heat on the model predictions was assessed. The results obtained with the Monofrax-M solidification path of 38 and 62 volume percent of α-alumina and β-alumina, respectively, showed limited effect in Stage II cooling. Hence, the use of linear release of latent heat is not unreasonable because the major resistance to heat transfer during Stage II cooling is the thermal conductivity of the alumina ore.

Table 5.1 – Thermal model load steps in the Monofrax-M thermocouple trial.

Step #	Simulation Description
Step 1	Remove alumina ore and steel bin. Ramp Step.
Step 2	Stage I Cooling.
Step 3	Remove upper graphite section. Ramp Step.
Step 4	Strip upper graphite section.
Step 5	Remove graphite mold and silica annealing sand platform. Ramp Step.
Step 6	Float (crown block).
Step 7	Add 0.3048 m (12 inches) of alumina ore on the bin bottom and 1.2192 m (48 inches) of steel flasking segments. Ramp Step.
Step 8	Block remains inside the steel bin with 0.3048 m (12 inches) of alumina ore below it.
Step 9	Add alumina ore to top of bin to give total height of 1.2192 m (48 inches). Ramp Step.
Step 10	Block remains inside the annealing bin.
Step 11	Add additional 0.2286 m (9 inches) of alumina ore and 0.3048 m (12 inches) high flasking segment. Ramp Step.
Step 12	Complete Stage II Cooling.

Note: Elapsed times/duration's for the various load steps have not been included to avoid disclosure of proprietary data.

Table 5.2 – Thermo-physical properties of Monofrax-M [25-27].

Material	Temperature (°C)	Thermal Conductivity k ($Wm^{-1}K^{-1}$)	Temperature (°C)	Heat Capacity C_p ($J\ kg^{-1}$)	Density ρ ($kg\ m^{-3}$)
Monofrax-M	*From Virginia Polytechnic Institute (using laser flash)*				*From ORNL* 3598
	20	6.50			
	250	5.18			
	500	3.75			
	750	3.45			
	1000	3.57			
	1250	3.76			
	1500	4.08			
	1600	4.30			
	From Orton Refractory Testing and Research Center (using calorimeter)				
	101	4.49	22	787	
	195	4.24	127	942	
	394	3.99	206	1020	
	597	4.03	304	1100	
	797	4.28	402	1134	
	868	4.2	518	1177	
	982	4.41	602	1198	
	987	4.44	717	1220	
	1000	4.62	811	1235	
	1094	4.87	917	1246	
	1099	4.83	1003	1253	
	1207	5.57	1130	1262	
	1208	5.53	1324	1275	
	1305	6.57	1440	1282	
			1613	1292	

Table 5.3 – Thermo-physical properties of the molding materials [26].

Material	Temperature (°C)	Thermal Conductivity k ($Wm^{-1}K^{-1}$)	Temperature (°C)	Heat Capacity C_p ($J\ kg^{-1}$)	Density ρ ($kg\ m^{-3}$)
Graphite	25	110.8	17	838	1690
	500	60.3	129	1048	
	1000	42.0	207	1257	
	1500	31.3	304	1383	
	2000	25.9	449	1508	
	2500	24.1	521	1592	
			631	1676	
			720	1718	
			829	1760	
			1652	1760	
Silica Sand	0	1.0	0	821	1620
	100	0.48	100	900	
	403	0.50	200	969	
	803	0.64	300	1027	
	1200	0.87	400	1075	
			500	1111	
			600	1137	
			700	1152	
			750	1155	
			2000	1264	
Alumina Ore	24	0.23	0	782	1270
	400	0.29	400	1100	
	800.5	0.36	800	1208	
	1002	0.39	1200	1289	
	1205	0.37	1600	1363	
			2000	1436	

Table 5.4 – Thermo-physical properties of the steel annealing bin [28].

Temperature (°C)	Thermal Conductivity k ($Wm^{-1}K^{-1}$)	Temperature (°C)	Heat Capacity C_p ($J\ kg^{-1}$)	Temperature (°C)	Density ρ ($kg\ m^{-3}$)
0	51.9	50	477.0	0	7863
50	51.5	100	477.0	15	7859
100	51.0	101	493.7	50	7840
150	49.8	150	493.7	100	7831
200	48.5	151	510.4	150	7819
250	46.4	200	510.4	200	7803
300	44.4	201	527.2	250	7787
350	43.5	250	527.2	300	7770
400	42.7	251	543.9	350	7753
450	41.0	300	543.9	400	7736
500	38.1	301	564.8	450	7718
550	37.7	350	564.8	500	7699
600	35.6	351	589.9	550	7679
650	33.9	400	589.9	600	7689
700	31.8	401	615.0	650	7635
750	28.5	450	615.0	700	7617
800	25.9	451	648.5	750	7620
850	25.9	500	648.5	800	4621
900	26.4	501	694.5	850	7616
950	26.8	550	694.5	900	7600
1000	27.2	551	740.6	950	7574
1050	28.0	600	740.6	1000	7548
		601	778.2	1050	7522
		650	778.2		
		651	836.8		
		700	836.8		
		701	1447.7		
		750	1447.7		
		751	820.1		
		800	820.1		
		801	556.5		
		850	556.5		
		851	535.6		
		900	535.6		
		901	589.9		
		950	589.9		
		951	598.3		
		1000	598.3		
		1001	606.7		
		1050	606.7		

Table 5.5 – Thermal conductivity of various alumina ores [26].

System Alumina Ore		Weakly Soft Sintered Ore		Hard Sintered Ore	
Temp. (°C)	Thermal Conductivity ($Wm^{-1}K^{-1}$)	Temp. (°C)	Thermal Conductivity ($Wm^{-1}K^{-1}$)	Temp. (°C)	Thermal Conductivity ($Wm^{-1}K^{-1}$)
24	0.23	20	0.84	20	2.64
400	0.29	398	0.61	398	1.8
800.5	0.36	798	0.55	798	1.8
1002	0.39	1100	0.58	1100	2.41
1205	0.37	1202	0.52	1202	2.52

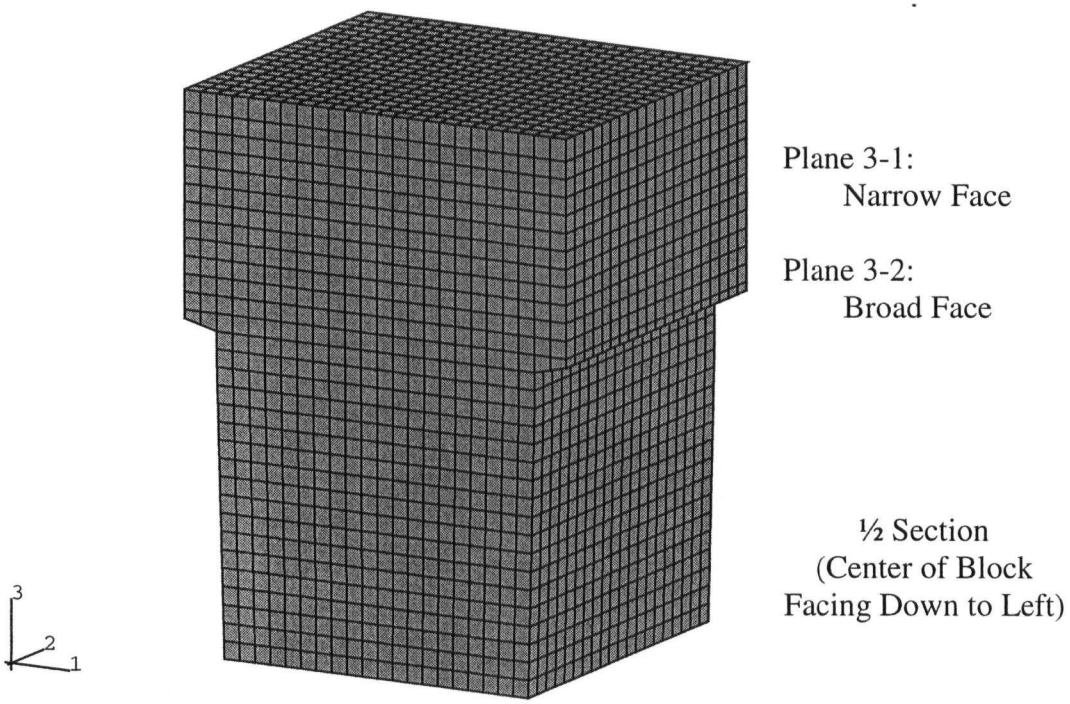

Figure 5.1 – Monofrax-M crown block mesh.

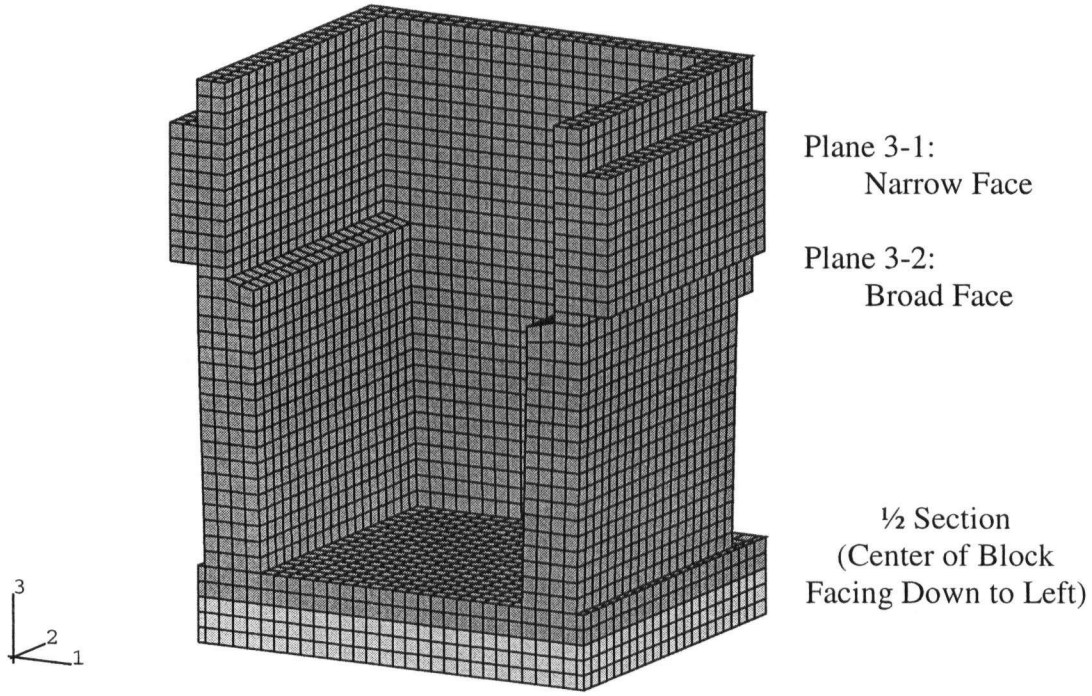

Figure 5.2 – Stage I cooling molding materials: graphite and silica annealing sand platform mesh.

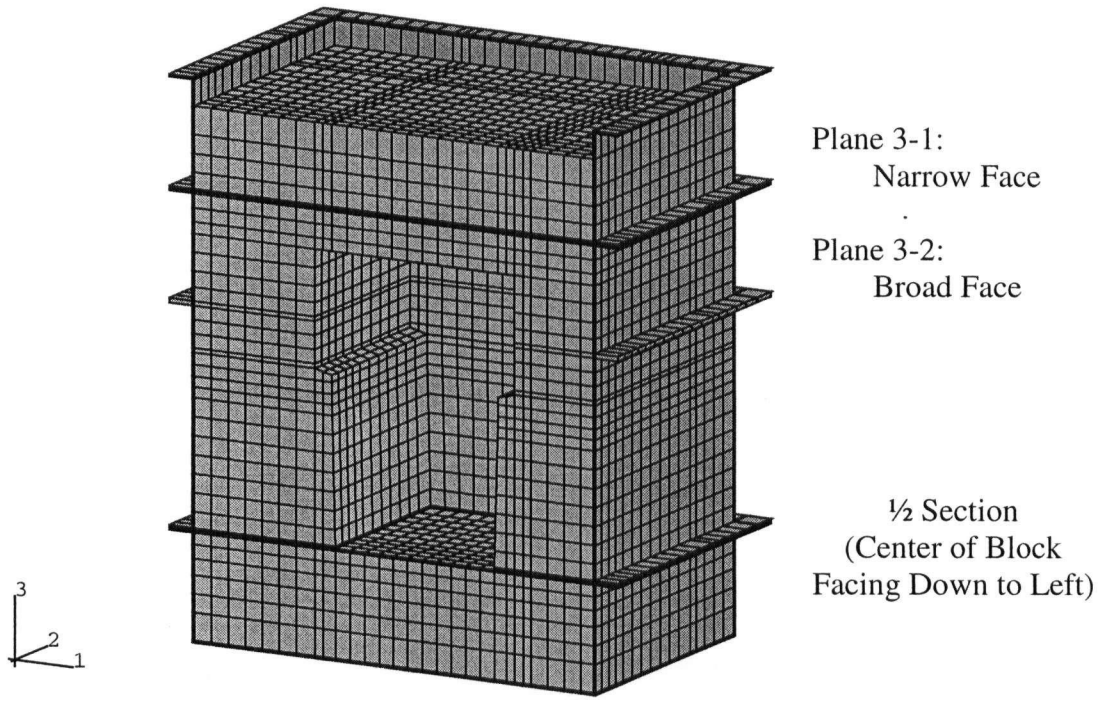

Figure 5.3 – Stage II cooling molding materials: alumina annealing ore and steel flasking bin mesh.

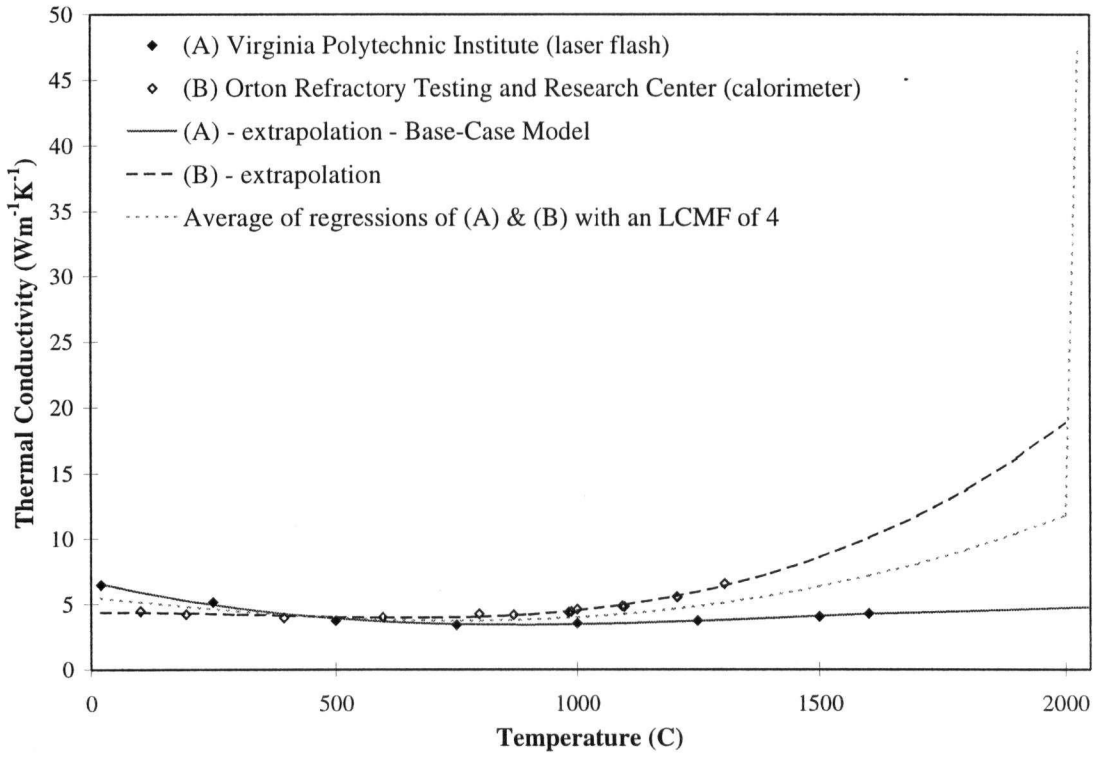

Figure 5.4 – Measured and modified thermal conductivity of Monofrax-M.

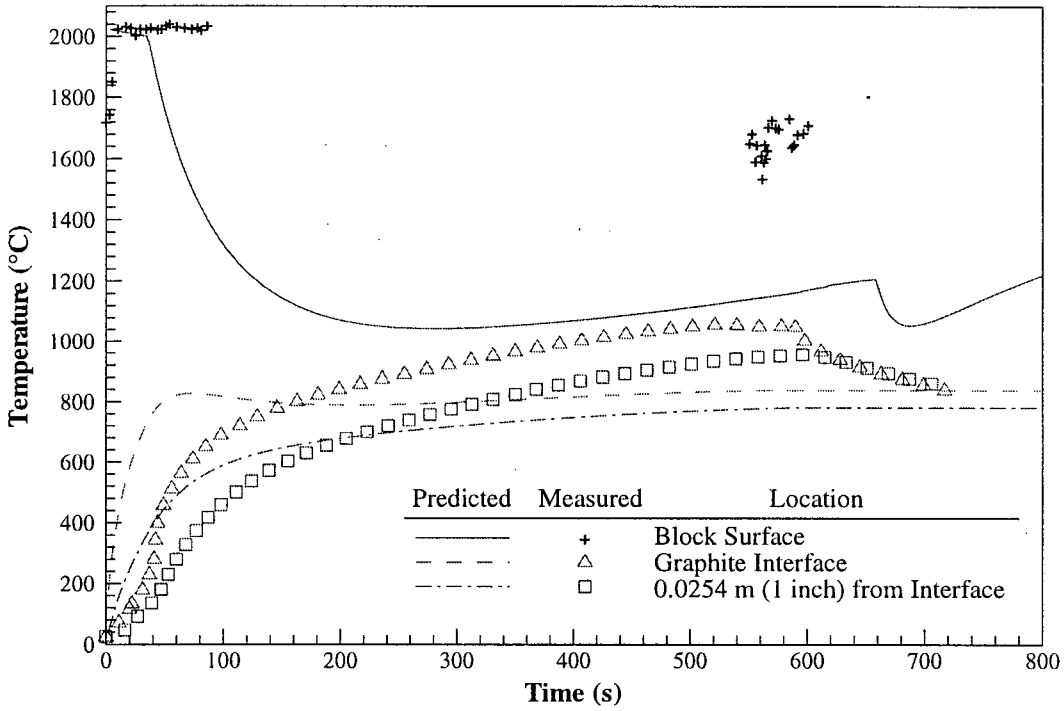

Figure 5.5 – Plot comparing thermocouple and pyrometer data with model predictions for the base-case thermal model during Stage I cooling.

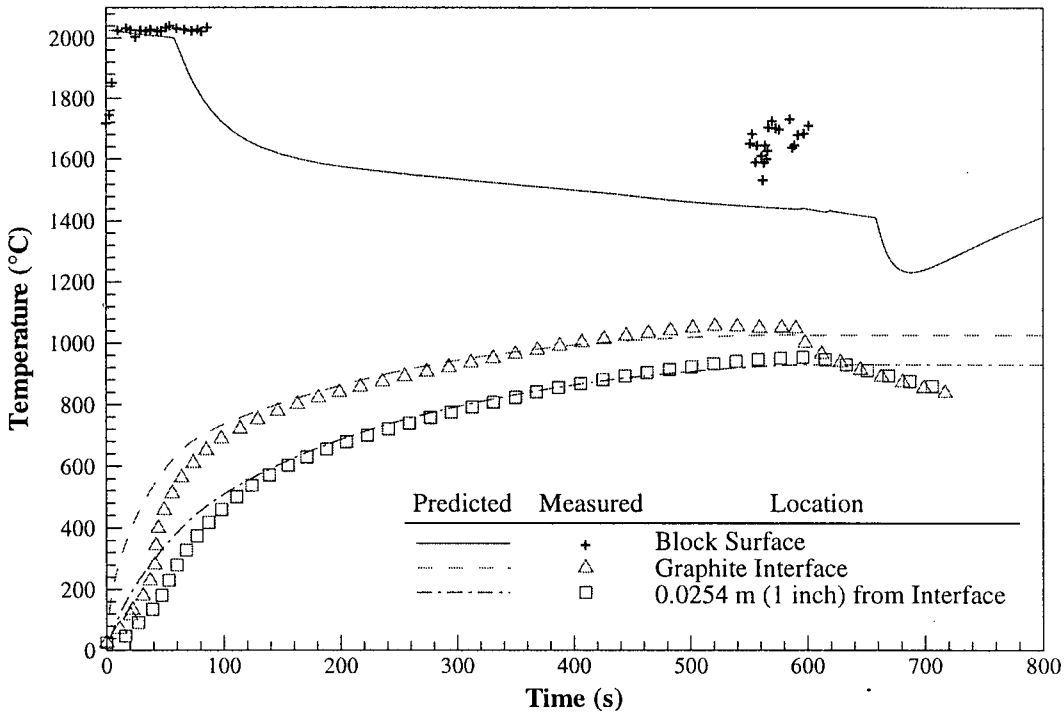

Figure 5.6 – Plot comparing thermocouple and pyrometer data with model predictions for the thermal model using modified thermal conductivity of Monofrax-M (an LCMF of 4) and modified casting/mold heat transfer parameters for Stage I cooling.

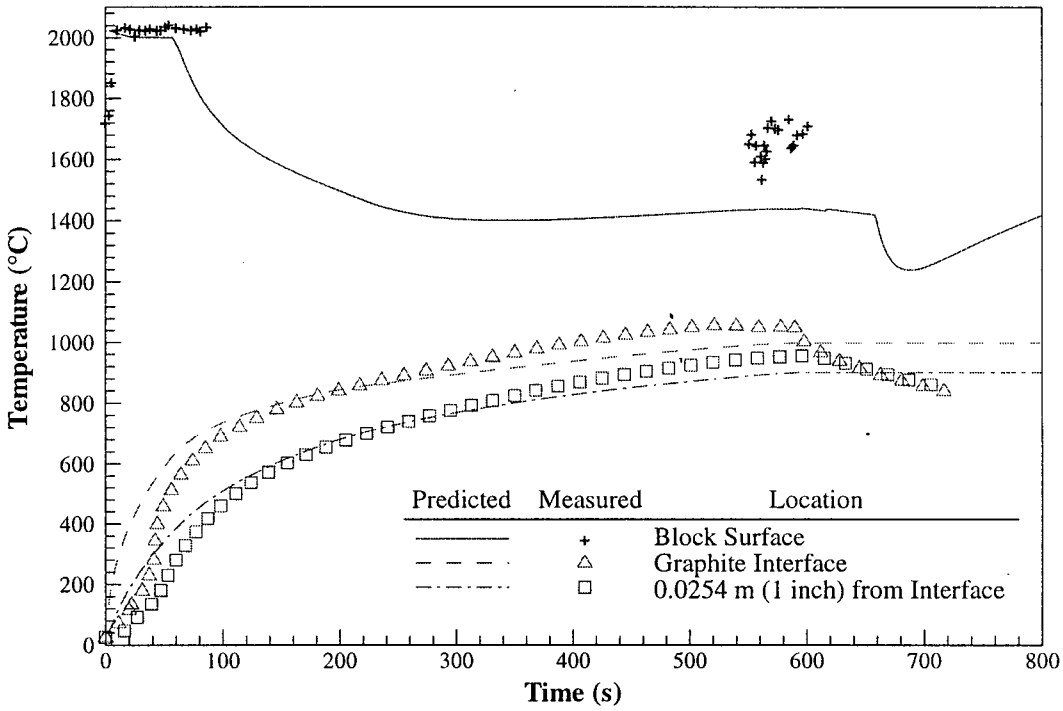

Figure 5.7 – Plot comparing thermocouple and pyrometer data with model predictions for the thermal model using modified latent heat to reflect a more correct solidification path of Monofrax-M for Stage I cooling.

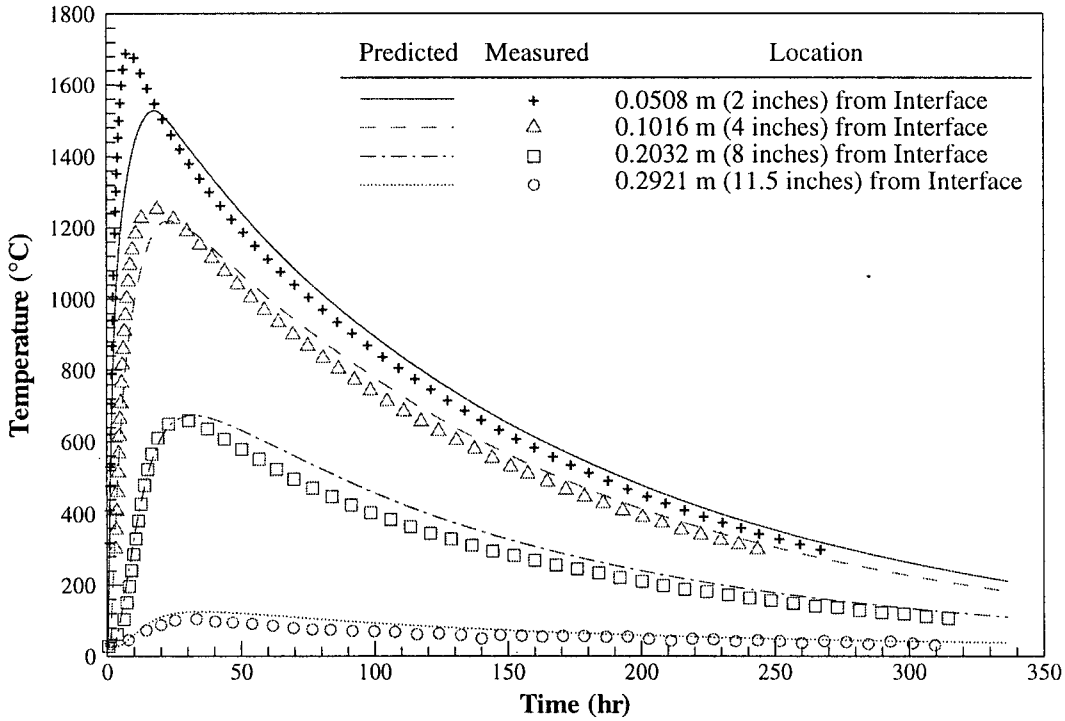

Figure 5.8 – Plot comparing thermocouple data with model predictions for the base-case thermal model for Stage II cooling.

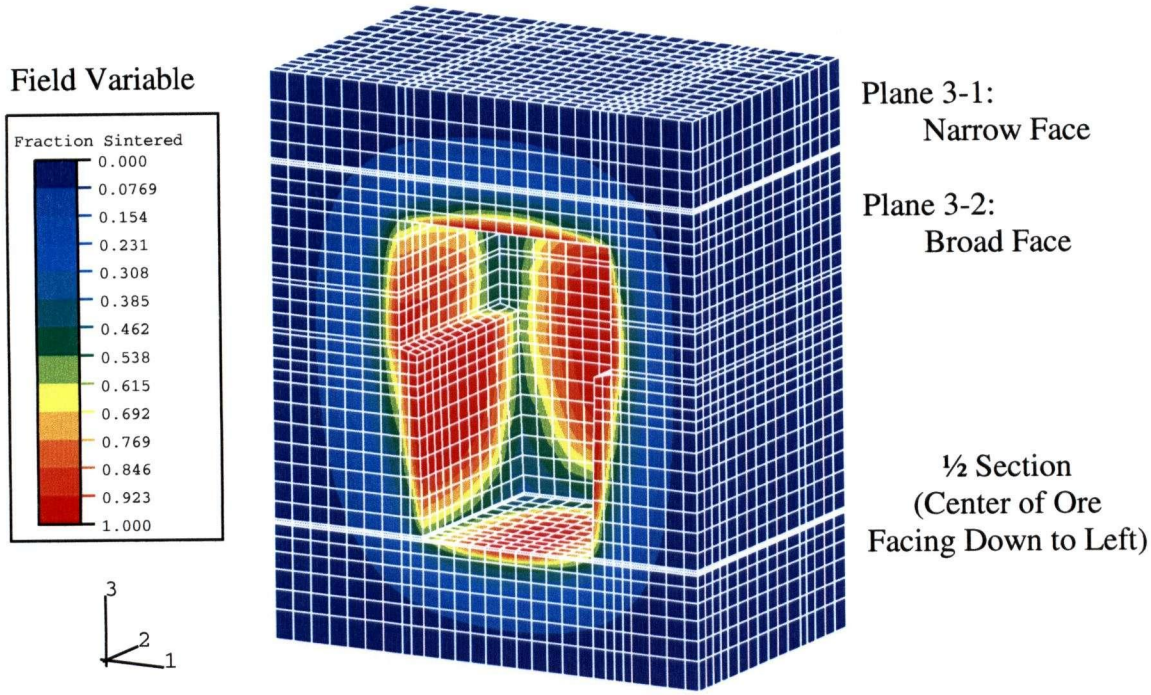

Figure 5.11 – Contour plot of fraction of alumina ore sintered.

CHAPTER 6

STRESS MODEL

The heat transfer analysis, presented in Chapter 5, provides part of the input necessary to perform a stress analysis and predict the evolution of stress/strain during the solidification and subsequent cooling of Monofrax-M crown blocks. Unlike the thermal model, which included the influence of the molding materials on the temperature evolution, the effect of the molding materials has been assumed to be negligible in the stress model. This section discusses the development of the Monofrax-M mechanical model and the preliminary stress/strain predictions. The resulting evolution of stress and strain in the refractory during various stages of the casting process is then linked to the occurrence of crack defects.

6.1 General Stress Model Formulation

The stress model is solved using the differential equations of equilibrium based on a force balance on an elemental volume and the compatibility conditions based on the displacement field and its relationship to strain in the body. The FEM equations can be developed through the minimization of virtual work within the element [30]. The temperature predictions obtained from the thermal model serve as 'thermal loads' input to the stress model in place of mechanical loads normally appearing in a structural analysis.

6.2 Formation of β-Alumina and Void Distribution

As previously discussed, Monofrax-M solidifies to form a multi-crystalline α-β solid comprised of roughly 38 % by volume of α-alumina and 62 % by volume of β-alumina at 2000°C assuming equilibrium solidification. In practice, however, the refractory solidifies with a β-alumina core surrounded by α-β shell. The β core forms due to segregation and rejection of Na_2O, a β stabilizer, at the solid/liquid interface, which accumulates in the center of the casting in the last section to freeze (refer to Figures 1.2 and 1.3 in which the β core can be seen). According to the study by Cockcroft and Brimacombe [10-11] on AZS refractories, the differential thermal dilatation associated with phase transformations can play a critical role on the generation of stresses and strains in castings. Similarly, for Monofrax-M, differences in the thermal contraction behavior of the αβ-alumina and the β-alumina can be expected to contribute to the generation of stresses and strains. Figure 6.1 shows the thermal expansion (heating) or contraction (cooling) behavior of the two phases. Adopting a reference temperature of 2000°C (solidus) for the onset of contraction, it is clear that the αβ-alumina contracts significantly more than the β-alumina.

The difference in mechanical properties associated with the β-alumina core can be introduced into ABAQUS through a subroutine called *ufield*. In *ufield*, a field variable, *fv1*, is defined at each integration point in the mesh reflecting the phase distribution in the as-cast material. Based on Figures 1.2 and 1.3, the shape of the β-alumina core is treated as a simplified ellipsoid in the stress model. Moreover, the β-alumina core is assumed to be present throughout the entire casting process. In the model, when *fv1* = 1, the

properties of the β-alumina are used and when *fv1* = 0.5, the properties of the 50% α-50%β-alumina are used. The 50% α-50%β-alumina is selected based on the average of the chemical compositions measured in the industrial trial (discussed in Section 4.1.2.3). Figure 6.2 shows the comparison between the measured β-alumina profile in mole % traversing a vertical line up the center of the casting and profile input to the model based on the simplified distribution. Figure 6.3 shows the β-alumina distribution in the form of a contour plot.

In addition to forming a β-alumina core, Monofrax-M crown blocks typically solidify with a substantial amount of shrinkage void in the header. It is not unreasonable to expect that the lower effective elastic modulus or stiffness within the void may influence the predicted stress or strain evolution in the mechanical model. The void has been included in the same *ufield* subroutine in ABAQUS as the αβ-alumina and β-alumina distributions. This has entailed defining a second field variable, *fv2*, in the subroutine to reflect the void distribution within the casting. The void region, based on Figure 1.2, is simplified as another smaller ellipsoid similar to the β-alumina core and is also assumed to form instantaneously and be present throughout the entire casting process. In the algorithm, when *fv2* = 1, the elastic modulus of the void region is assumed to be 20 Pa (since numerical solutions may not be achieved with a 0 Pa modulus) and when *fv2* = 0, the properties of either the αβ-alumina or β-alumina are used, depending on the first field variable, *fv1*. The contour plot of the void distribution used in the stress analysis is presented in Figure 6.4.

6.3 Constitutive Behavior

To explore the influence of constitutive behavior on the predictions of stress and strain, two material models have been employed to simulate the mechanical behavior of Monofrax-M. The two approaches are presented in two subsections entitled: Elastic Analysis and Elastic-Plastic Analysis.

6.3.1 Elastic Analysis

In the elastic stress model, the elastic strain can be calculated using the elastic modulus and Poisson's ratio of the casting. Similar to the thermo-physical properties in the thermal model, a temperature dependent elastic modulus is required due to the large temperature range the casting experiences. The elastic moduli of αβ-alumina and β-alumina are plotted in Figure 6.5 versus temperature (data was measured at the United Technologies Research Center [23] and was linearly interpolated). Based on the data of a 96% alumina [31], the Poisson's ratio of the αβ-alumina and the β-alumina is assumed to be 0.21. As can be seen in Figure 6.5, in both cases, the elastic modulus at 2049°C has been ramped to a low value of 1% of the modulus at 2000°C. The elastic modulus has been drastically reduced to minimize the influence of the liquid on the results of the stress analysis. Ideally, the liquid would be removed from the analysis as it is incapable of supporting shear. However, in a fixed domain analysis, such as the one applied here, specifying a small but finite elastic modulus approximates its removal.

Based on the literature review, most mechanical analyses of refractory structures adopt elastic material behavior due to the limited ductility associated with ceramics at low temperature and because of ease of implementation. In the present study, an elastic

analysis has also been performed to serve as a benchmark against which the influence of adopting plasticity can be assessed. The shortcoming of this analysis is that inelastic deformation, which likely takes place in the refractory at elevated temperature, is not considered. Consequently, the evolution of stress predicted by the elastic model will be only qualitative at best. While this does not preclude an attempt to develop correlation between the model predictions and typical cracks found in as-cast blocks, the limitations of the approach should be borne in mind while drawing conclusions.

6.3.2 Elastic-Plastic Analysis

Plasticity and creep are the two mathematical constructs commonly used to describe inelastic or permanent deformation in materials. Of the plasticity approaches available, the Von Mises yield criterion, also called 'Metal Plasticity' (discussed in Chapter 2), is probably the most widely used. Of the creep equations available, most are based on steady state creep behavior.

As discussed in Chapter 4.2, stress-strain data was measured at ORNL employing flexural tests. This data has been adopted for use in the present model assuming symmetric tensile and compressive behavior – see the following section. After careful considerations of the options available, an elastic-plastic model was developed for analysis of the Monofrax-M crown blocks.

Note: While plasticity can be used to quantify both stresses and inelastic strains arising in the material at elevated temperatures, it has certain limitations in application to the present problem. One problem with the elastic-plastic approach is that it fails to address creep – e.g. continued accumulation of strain at constant load, a condition that can be

approached in casting processes. Since time-dependent deformation or creep in ceramics often takes place at high temperatures, this could result in error. The power-law creep relation in Equation 2.2, for example, could be used to address time-dependent deformation. However, its applicability depends on the extent to which steady state flow conditions prevail. It should be noticed that during the transient stage loading conditions that occur in a casting process, deformation associated with primary creep may also be important. As a result, it is essential to have proper mechanical data measuring both the primary and secondary creep behavior for a large range of temperatures for Monofrax-M. Due to the limited availability of the creep data, an elastic-creep analysis has not been undertaken in the present research.

6.3.2.1 Manipulation of ORNL Data for Input to ABAQUS Plasticity Model

To prepare the data for input to the stress model in ABAQUS, the stress-strain data presented in Section 4.2.2 was further processed to evaluate separately the plastic strain from the total strain. This was done by subtracting the elastic strain, based on the measured elastic moduli, from the total strain obtained from the flexural tests. Since the results for the different strain rates tests at 1100 and 1350°C indicate little sensitivity to strain rate, the average of the measured data were adopted. Due to the limited number of tests performed, data at the low strain rate ($2x10^{-7}$ s^{-1}) for temperatures of 1600°C and higher was not available. An attempt to fit a simple plasticity hardening law (the Ramberg-Osgood relationship in Equation 2.1) was made to allow extrapolation to elevated temperatures. Unfortunately, the k and n constants evaluated at each strain rate and test temperature could not be correlated in a logical and consistent manner. As a

result, the data at $1x10^{-5}$ s^{-1}, which was the only data available at a consistent strain rate at all the test temperatures, was employed to generate the data for input to the stress model. Thus, strain rate sensitivity could not be addressed. Figure 6.6 summarizes the resulting stress-plastic strain curves input to the model. It should be noticed that the material was assumed to be elastic-perfectly plastic at 1100°C.

6.4 Geometry

The same 3-dimensional Monofrax-M refractory casting mesh utilized in the thermal model, shown in Figure 5.1, was employed in the stress analysis. The mesh consists of 8-node linear brick stress/displacement elements available within ABAQUS.

6.5 Boundary Conditions

As previously discussed, the stress analysis has been limited to the fused-cast refractory. Since interaction with the surrounding molding materials has been neglected, only the symmetry boundary needs quantification. The symmetry boundary used in the stress model follows directly from the assumption of symmetry in the heat transfer model. On the vertical plane which bisects the broad face of the casting, displacement in the direction normal to the plane of symmetry has been suppressed, as the thermal loads are assumed to be equal and opposite.

6.6 Predictions Obtained from the Elastic Stress Model

In the elastic stress analysis, the stress evolution predicted by the model can be observed via plots of stress versus time or contour plots of the stress distribution in the casting.

Referring to the coordinate system defined in Figure 1.1, the three normal components of stress in the 1, 2 and 3 directions and three components of strain can be output from ABAQUS, together with other quantities such as the principal stresses and Von Mises stress, if desired. One of the challenges in interpretation is selecting the appropriate output so as to avoid being overwhelmed by the large volume of data available for output. Fortunately, as previously discussed, tensile stresses acting parallel to the broad face, S22, are consistent with the orientation of the cracks that have been found in the crown blocks. Interpretation of the data is thus focused on the tensile stresses and strains in direction-2. Further, based on the β-alumina distribution and the location of the cracks formed – refer to Figures 1.2 and 1.3 – a detailed analysis of the data can be limited to only a few nodes to further reduce the volume of data. Figure 6.7 shows the three selected nodes (A, B, and C) located in the Monofrax-M crown block. As can be seen, node A is at the transition in phase from β to αβ-alumina, whereas, nodes B and C are in the αβ-alumina region. Furthermore, comparisons are also made with the measured modulus of rupture (MOR) of Monofrax-M to evaluate the severity of the tensile stresses predicted by the model.

To determine the influence of the β-alumina formation and the void distribution on the stress evolution during the casting process, three stress analyses have been completed: one, based on a homogeneous αβ-alumina casting, a second including the β-alumina core formation, and a third with both the β-alumina formation and the void distribution. Further, the preliminary sensitivity analysis was limited to elastic material behavior only, to avoid the complication of plastic strain generation.

6.6.1 Benchmark Case – αβ-Alumina Crown

An elastic stress analysis performed based on the properties of αβ-alumina only serves as a benchmark case. The stress evolution developed in this model is mainly driven by the temperature gradient predicted by the thermal analysis. When the refractory has completely solidified and cooled, there should be no residual stresses remaining at the end of the casting process. During Stage I cooling, the shell of the casting has solidified while the core remains molten. Since the core of the refractory is liquid, it is in a near zero state of stress. The resulting force balance on the shell results in the outer cooler shell in tension and inner hotter shell in compression. The S22 stress (parallel to the broad face) is illustrated in Figure 6.8. The large tensile stress on the base edge of the block due to high heat extraction can also be observed in the figure.

Figure 6.9 shows the stress evolution at discrete points within the refractory during Stage I cooling, and for the early stages of Stage II cooling in the alumina ore. The temperature evolution is also included in the plot for comparison. As can be seen, the stresses at the surface node C are tensile and reach a peak magnitude of approximately 425 MPa at roughly 800 seconds. At the location of nodes A and B, the material is in a state of compression and peaks between 800 and 900 seconds. The stress at 0.1524 m (6 inches) from the block center (node B) is higher in magnitude than the stress at 0.0762 m (3 inches) from the block center (node A) consistent with a decrease in stress toward the block center. It should be noted that the measured MOR for this refractory is approximately 26 and 23 MPa at room temperature and 1510°C, respectively [2]. The unrealistic high tension and compression stresses obtained in this analysis are due to the assumption of pure elastic behavior of the material.

Figure 6.10 shows the stress evolution within the refractory during Stage II cooling. As can be seen, the S22 stresses rapidly decrease during the early stages of Stage II cooling, which is a result of thermal rebounding of the block surface temperature – see also Figure 6.9. The 'plateau' in temperature at nodes A, B and C, indicates continued latent heat evolution in the block associated with solidification. Shortly after solidification is completed, roughly at 20 hours of cooling, the stresses at nodes A, B and C rise to a second peak associated with the completion of solidification and the increase in stiffness in the center of the block. As cooling in Stage II proceeds, the stresses gradually moderate approaching zero as the block cools toward room temperature and gradients decrease.

6.6.2 Effect of β-Alumina Core Formation

To assess the influence of the β-alumina formation on the stress development within Monofrax-M crown block, the model was run with the β-alumina core – refer to Section 6.2. Unlike the previous analysis, both the temperature gradient as well as the different thermal dilatational behavior of αβ-alumina and β-alumina drive the stress evolution in the case of the refractory with the β-alumina core. The contour plot of S22 at the end of the casting process, shown in Figure 6.11, clearly illustrates this as it shows the β-alumina core in the high state of compression. Compression in the β-alumina zone develops because it has lower thermal contraction than the αβ-alumina.

Figure 6.12 shows the stress evolution obtained from the model during Stage I cooling. Comparing the results with the previous analysis, it can be observed that the stress development follows similar trend during Stage I cooling. Figure 6.13 presents the

Stage II cooling stress profile obtained from the analysis incorporating the β-alumina distribution. As can be seen, during Stage II cooling, the β-alumina formation has a pronounced effect on the stress evolution predicted by the model. Since the β-alumina core contracts less than the αβ-alumina, the material at node A is subjected to increasing compressive stresses as the refractory block cools. Similarly, nodes B and C, which are composed of αβ-alumina, increase in tension toward the end of Stage II cooling. Clearly, the β-alumina core has a major influence on the generation of tensile hoop stresses (S22) in the crown blocks and likely also plays a role in the generation of cracks.

6.6.3 Effect of β-Alumina Core Formation and Void Distribution

In addition to the β-alumina formation, the void distribution discussed in Section 6.2 was also introduced into the model and run to evaluate the effect of the void distribution on the model predictions. The contour plots of S22 for the whole casting (with header) and the crown block (header removed) at the end of Stage II cooling are shown in Figures 6.14 and 6.15, respectively. The void region, which has a reduced capacity to support any thermal load can be observed in Figure 6.14. As shown in Figure 6.15, high tensile stresses have developed adjacent to the αβ/β-alumina interface. This high tensile region correlates well with the occurrence of cracks.

Figures 6.16 and 6.17 present the stress evolution of Monofrax-M during Stages I and II cooling, respectively. As can be seen from both Figures, the stress profiles predicted by the model including the void are slightly modified (the magnitude of the stresses are smaller) when comparing to stresses predicted without consideration of the

void, Figures 6.12 and 6.13. This indicates that the stress distribution predicted by the model is only slightly sensitive to the void distribution.

6.7 Preliminary Predictions Obtained from the Elastic-Plastic Stress Model

Unlike the previous three elastic stress analyses, permanent or inelastic deformation is considered in the plastic stress model, which would occur predominantly at elevated temperatures in Monofrax-M. Both stresses and plastic strains developed in the casting process can be quantified in the plastic stress analysis. Since the cracks were found to be intergranular and formed at elevated temperature (refer to Section 4.1.2.3), the predicted plastic strain, in addition to the stress predictions, can be correlated against cracks in order to propose mechanisms for crack formation in Monofrax-M. Similarly, the interpretation of the results is focused on the stress and plastic strain in the direction-2, adjacent to the center of the broad face of the block consistent with the orientation and location of production cracks.

The drawback to the present plastic stress analysis is the lack of rate sensitivity in the plasticity data employed in the model – recall only the data for $1x10^{-5}$ s^{-1} was employed in the elastic-plastic stress analysis. Figures 6.18 and 6.19 show the absolute values of the predicted plastic strain rate for Stages I and II cooling, respectively. The temperature evolution has been included in the plots for comparison. As can be seen, the $1x10^{-5}$ s^{-1} rate used in the model is applicable only at the surface of the block during Stage I cooling whereas it is too high for application to the material in the center. Moreover, looking at Stage II cooling, Figure 6.19, it is somewhere between 4 and 5 orders of magnitude too high. Consequently, the results of the elastic-plastic model

during Stage I cooling are probably not unreasonable. However, during Stage II cooling, the plastic strain may well be significantly under-predicted by the model – e.g. the constitutive model used will be too stiff as it is valid at a much higher strain rate.

The contour plot of PE22 (plastic strain in the direction-2) predicted by the plastic stress model incorporating the β-alumina core and the void distribution at the end of the casting process is shown in Figure 6.20. Similar to the previous elastic stress predictions, the β-alumina region, which is under compression due to thermal dilatational behavior of the two phases, can be seen in the plot as a region that has accumulated significant compressive plastic strain. Also shown in the plot, is the region below the β-alumina zone in which high tensile strains can be observed consistent with the formation of cracks found in that location.

The evolution of stress and temperature predicted by the model for the refractory during Stage I cooling are shown in Figure 6.21. Comparing with the previous elastic stress predictions, the results obtained by the plastic stress model are more realistic as the values are slightly below the MOR of Monofrax-M. As shown in the figure, during graphite and air cooling, tensile stresses gradually develop on the surface of the casting. However, there is a peak in tensile stress at the block surface (location C) associated with the rapid drop in temperature caused by accelerated heat transfer. The temperature then rebounds – e.g. rapidly heats up. This rebound in temperature results in a change in state of stress at the surface of the refractory from tensile to compressive. Likewise, node B shifts from compression to tension. This sub-surface tension has the potential to give rise to the formation of subsurface cracks particularly if the inner, hotter material has less ductility.

Figure 6.22 shows the stress predictions for the crown during Stage II cooling. As can be seen, there is once again a stress reversal in that the surface and interior nodes are predicted to change stress states from compressive back to tensile (at the surface) and from tensile to compressive (subsurface). This behavior is due to both a moderation in temperature gradients experienced by the casting as well as the differential thermal contraction behavior of the αβ-alumina and the β-alumina. As the rate of the cooling decreases, the stresses at both the center and the surface related to temperature gradient decrease. However, the stresses associated with the β-alumina core (compressive in the β-alumina region and tensile in the αβ-alumina region) increase gradually placing the interior of the crown in compression and exterior in tension.

As discussed, the strain is an important parameter that may also be related to fracture or tearing in the fused-cast refractory. The plastic strain evolution predicted by the model during Stage I cooling is shown in Figure 6.23 together with the temperature variation. As can been seen, high tensile strain develops at the block surface. The strain at which damage begins to occur in Monofrax-M (the critical strain at which the peak stress is reached) observed from the flexural tests at 1350 and 1500°C (refer to Figures 4.11 to 4.14) is approximately 0.0015 to 0.002. As a result, the surface of the casting is susceptible to the formation of damage during Stage I cooling.

Figure 6.24 shows the plastic strain evolution of the refractory during Stage II cooling. As can be seen, the strains developed at node B change from compression to tension. The strains at nodes B and C are close to the critical strain values obtained from the flexural tests. Bearing in mind that the strains are likely underestimated during Stage II cooling because of the use of the 1×10^{-5} s^{-1} data, this suggests continued potential for

damage in Stage II cooling throughout the outer regions of the block extending outward from the β-alumina core.

Based on the stress/strain predictions, it is clear that the β-alumina core plays a major role in the generation of tensile stresses. The current process has the potential to generate large subsurface tensile stresses. Overall, it is likely that crack initiates subsurface and propagates outwards. However, without proper accounting for the effect of strain rate on the constitutive behavior of this material, the exact direction of propagation is unclear.

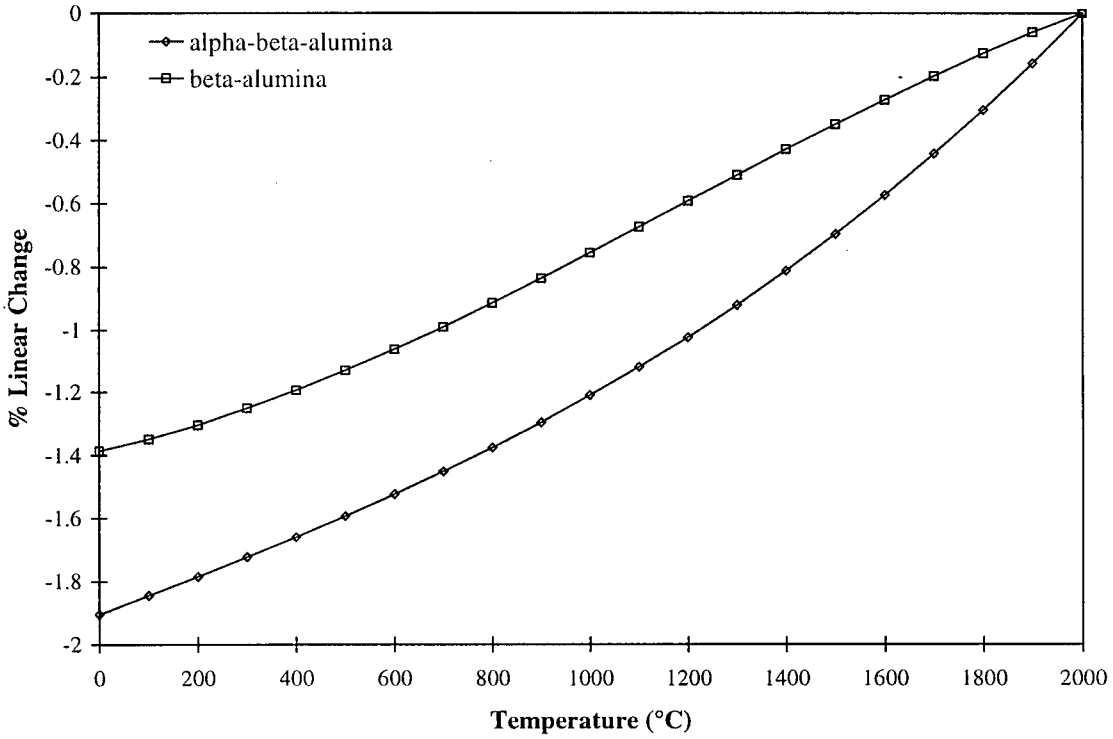

Figure 6.1 – Thermal expansion / contraction behavior of αβ-alumina and β-alumina.

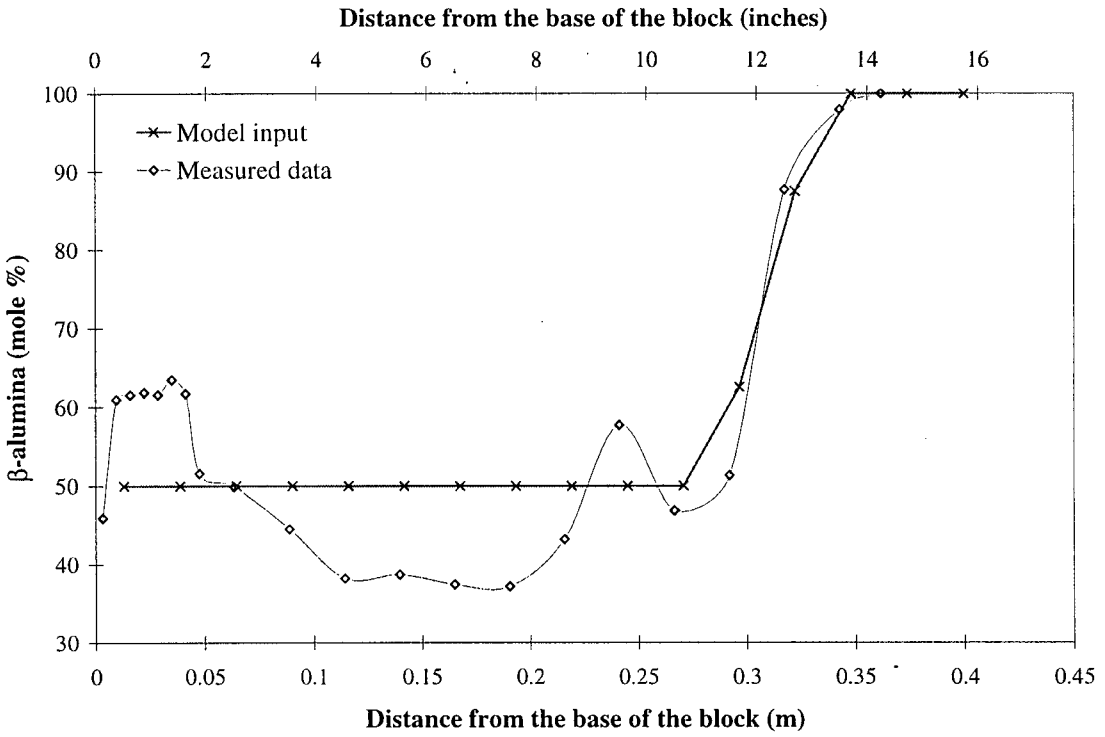

Figure 6.2 – Comparison of model input and chemical analysis results obtained from Monofrax-M crown block measured at the vertical centerline of the plane bisecting the broad face of the casting.

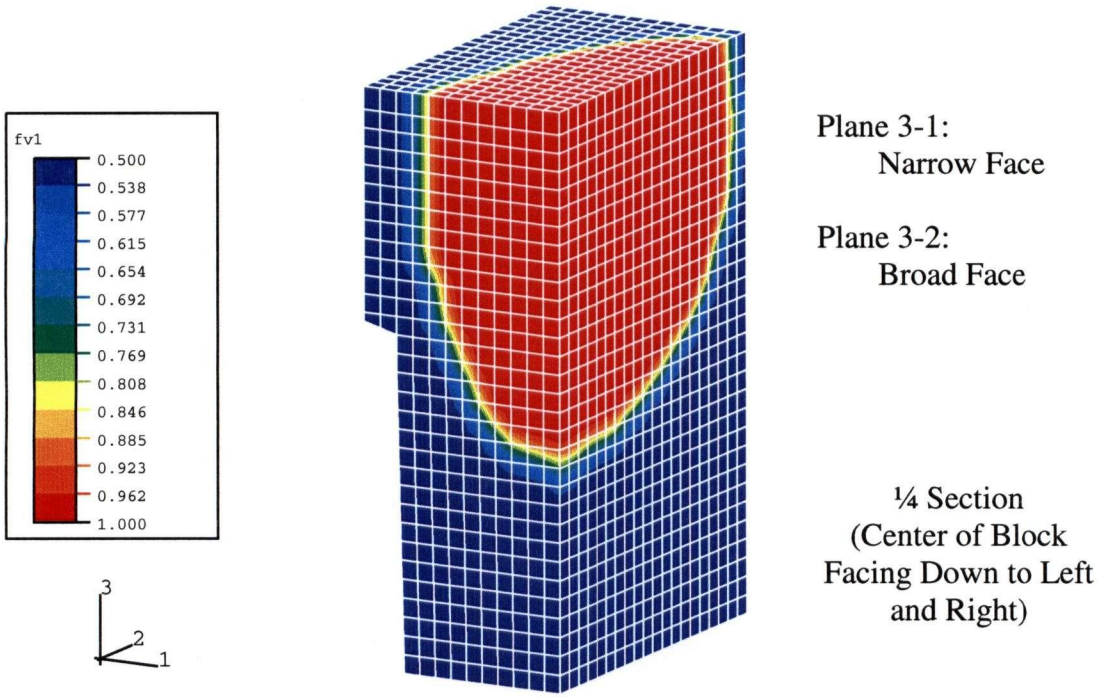

Figure 6.3 – Contour plot of the αβ-alumina and the β-alumina distributions used in the stress model.

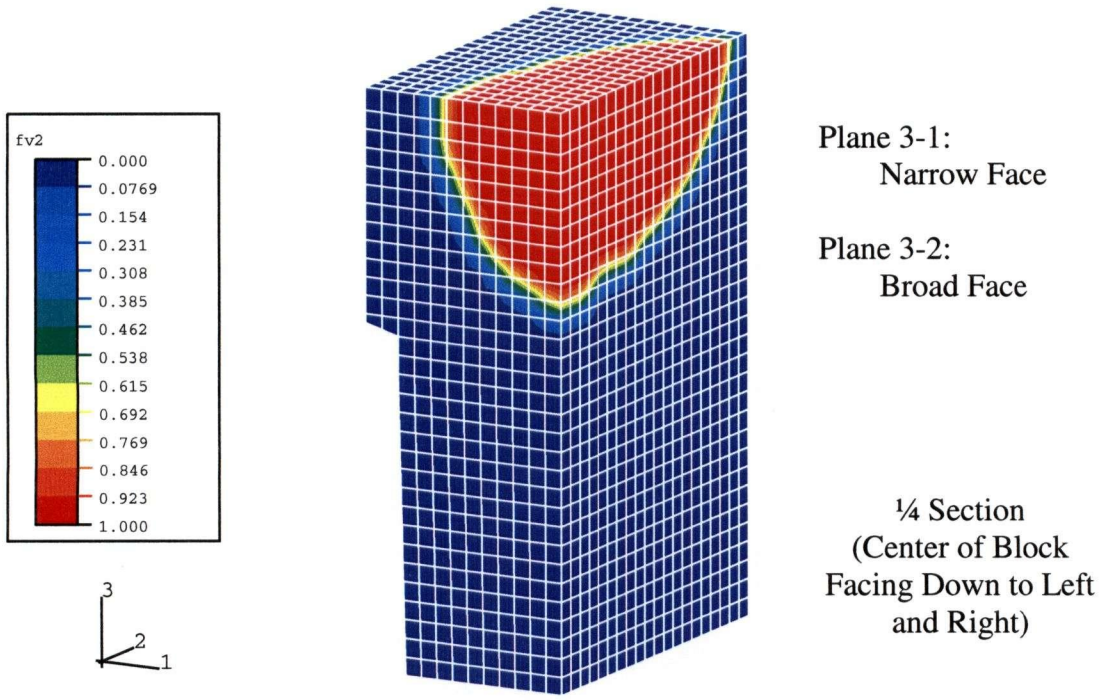

Figure 6.4 – Contour plot of the void distribution used in the stress model.

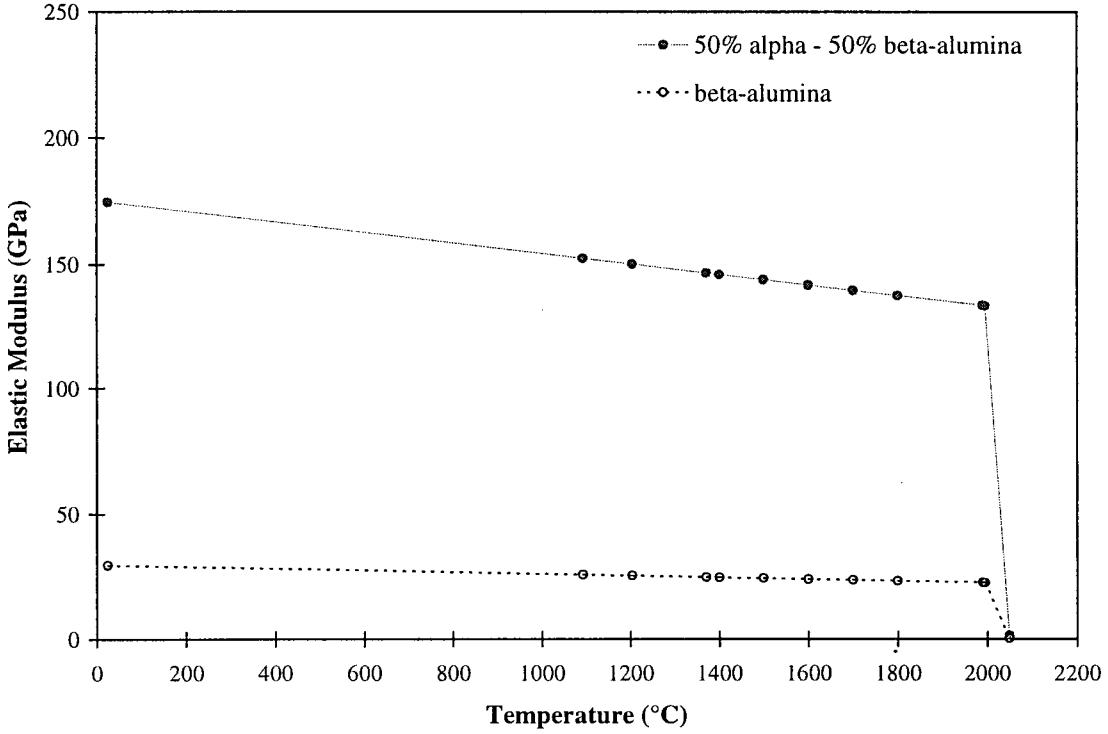

Figure 6.5 – Variation of elastic modulus with temperature for 50% α-50% β-alumina and β-alumina.

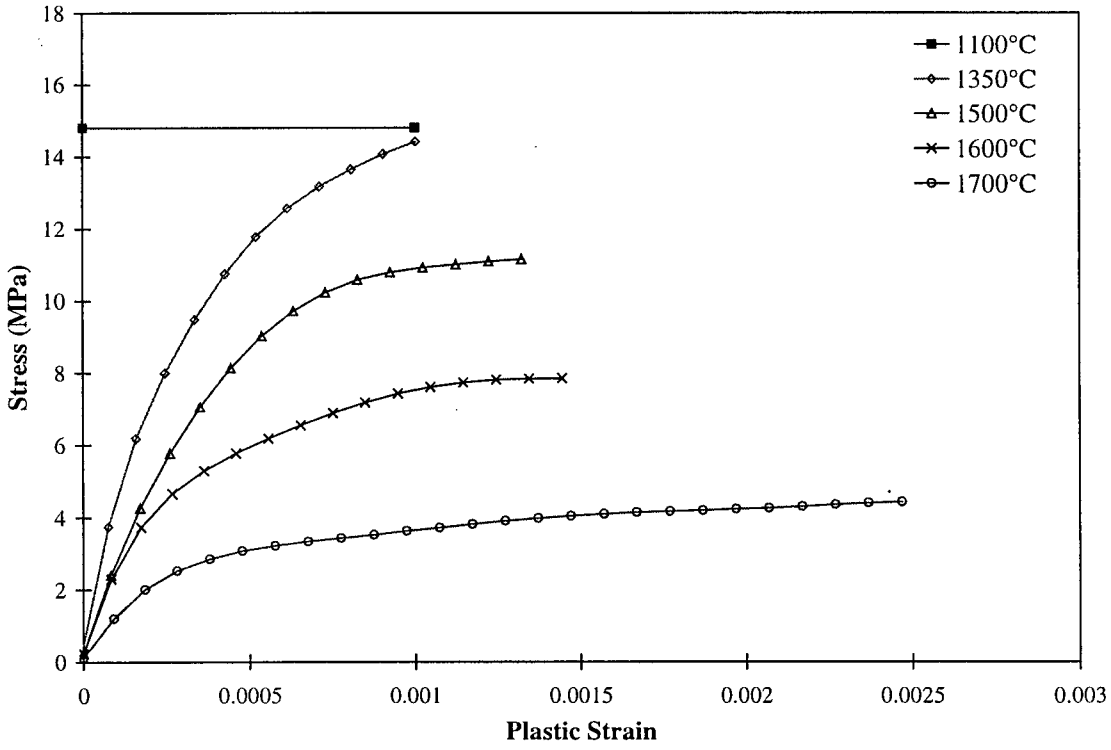

Figure 6.6 – Stress-plastic strain curves of Monofrax-M at $1x10^{-5}$ s^{-1} for input to ABAQUS plasticity model.

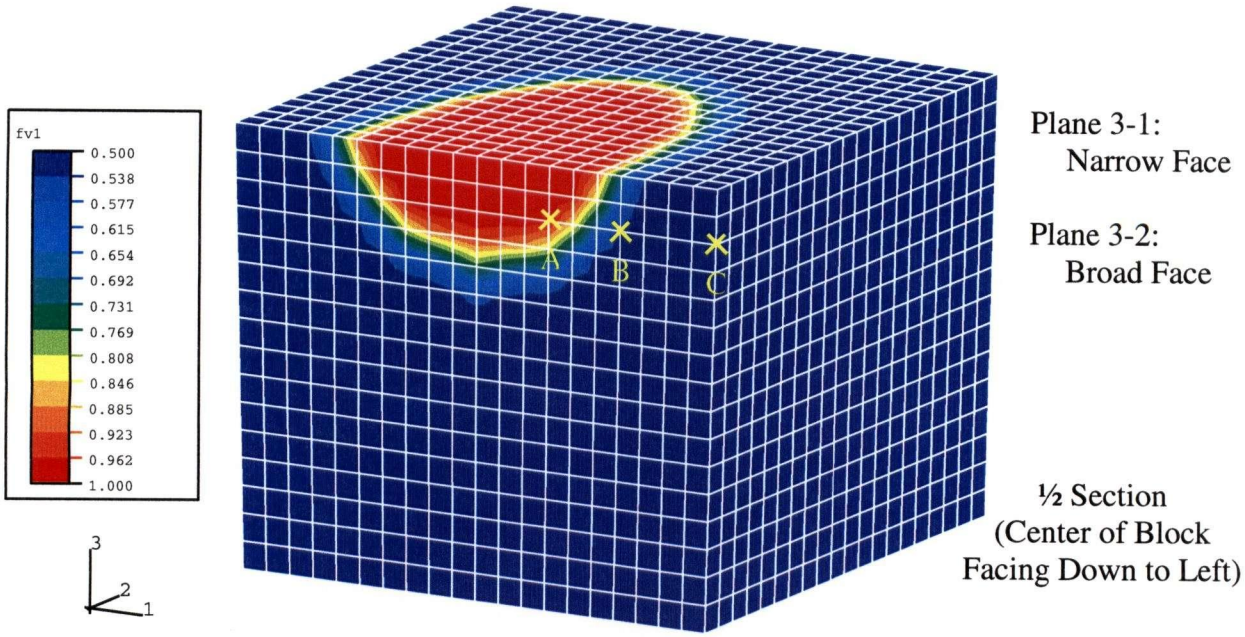

Figure 6.7 – Contour plot of the β-alumina distribution in the Monofrax-M crown block showing the selected nodes for interpretation.

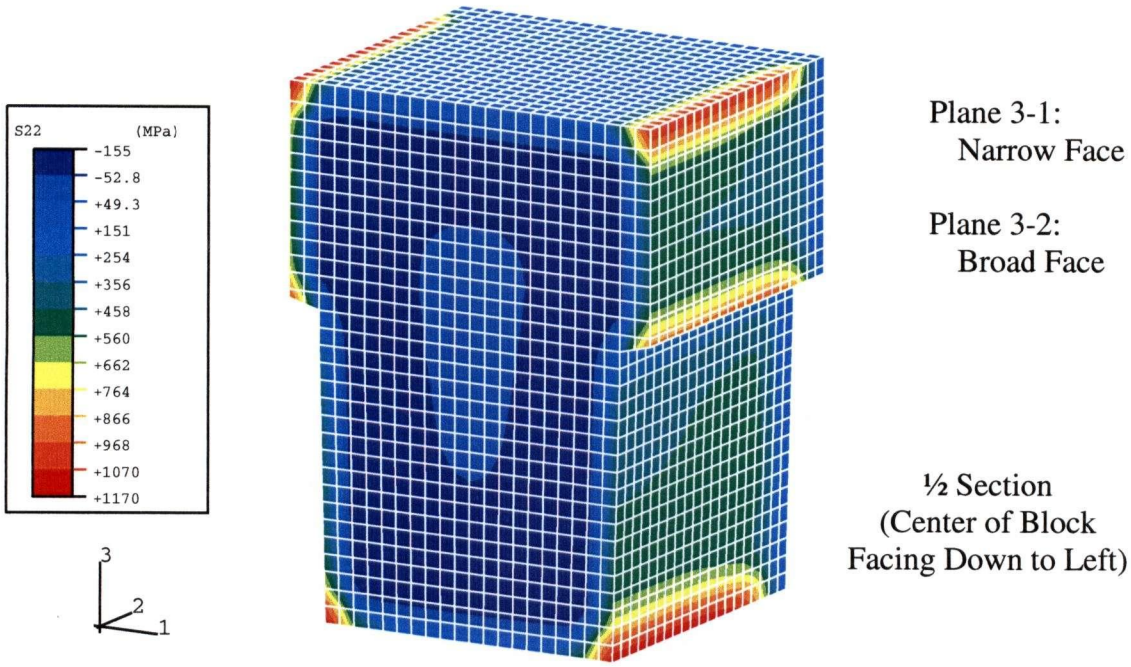

Figure 6.8 – Contour plot of S22 for Monofrax-M at the end of Stage I cooling for the elastic stress analysis with a homogeneous αβ-alumina casting.

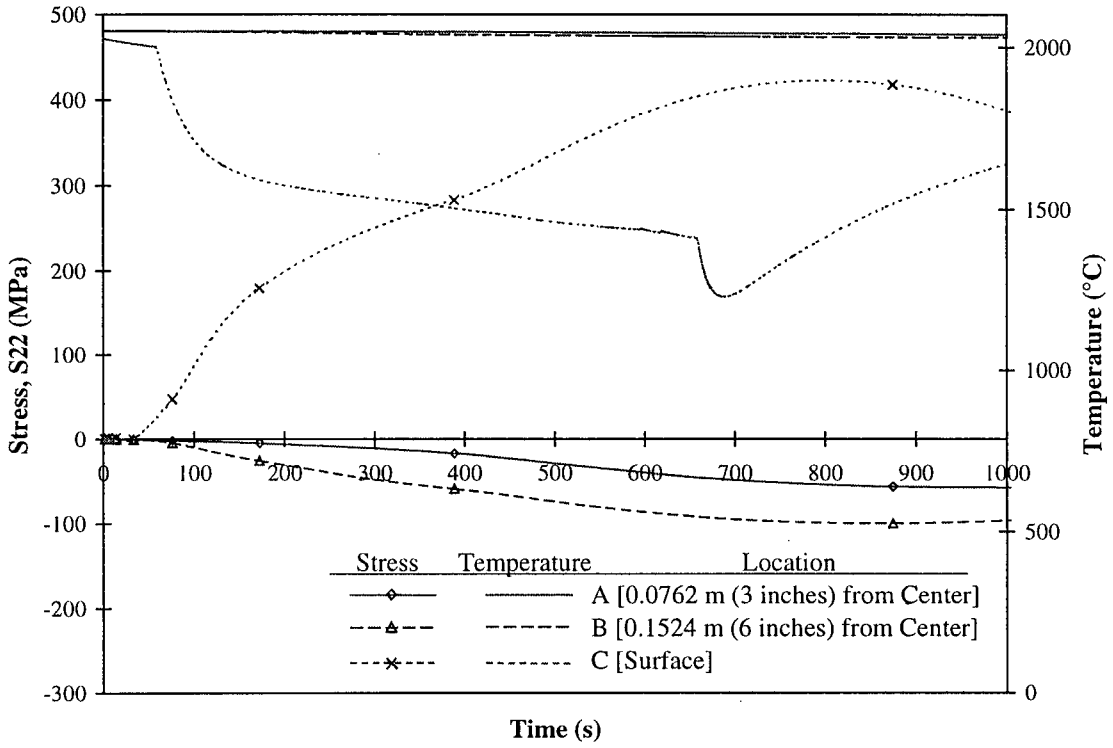

Figure 6.9 – Stress evolution of Monofrax-M during Stage I cooling for the elastic stress analysis with a homogeneous αβ-alumina casting.

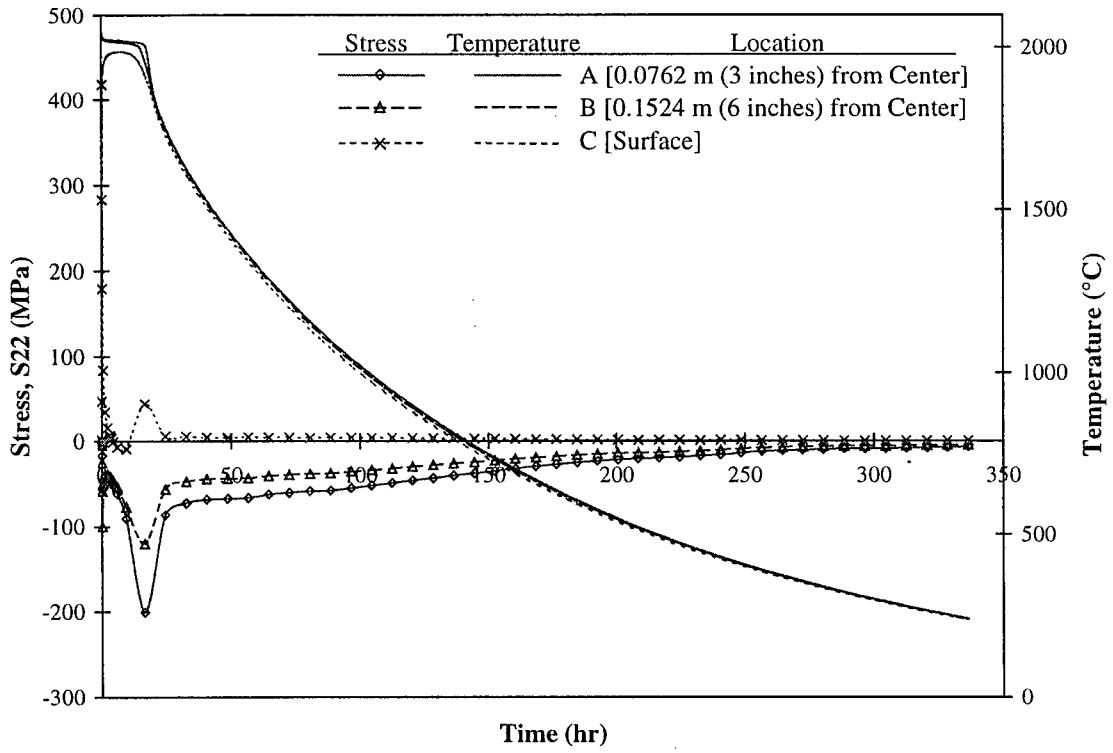

Figure 6.10 – Stress evolution of Monofrax-M during Stage II cooling for the elastic stress analysis with a homogeneous αβ-alumina casting.

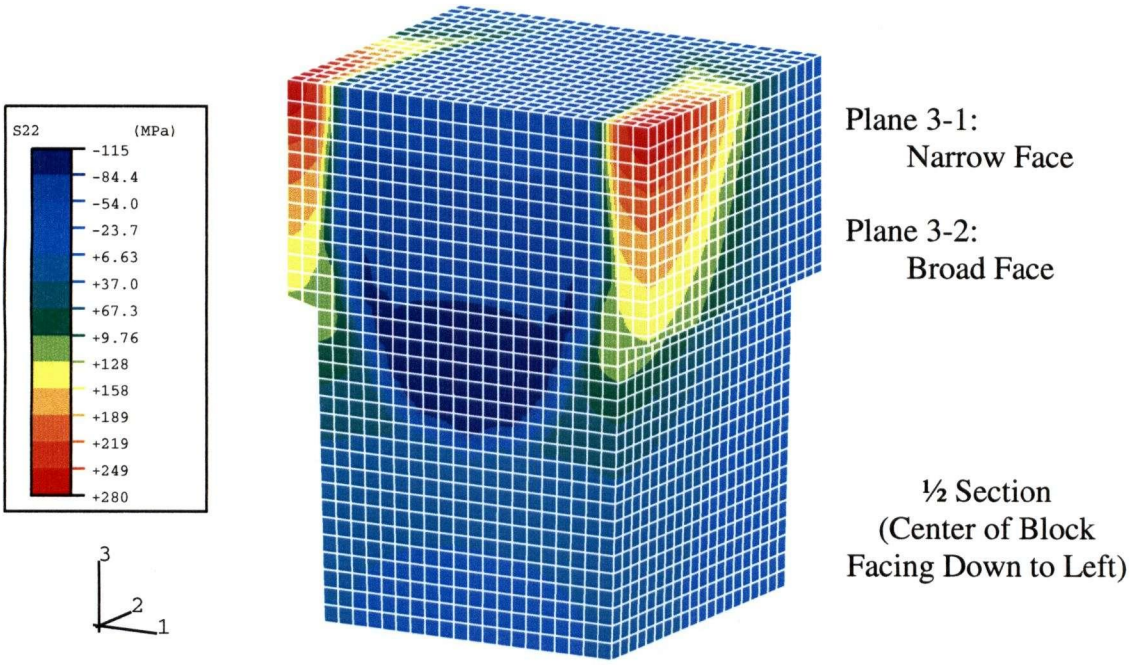

Figure 6.11 – Contour plot of S22 for Monofrax-M at the end of Stage II cooling for the elastic stress analysis with β-alumina core formation.

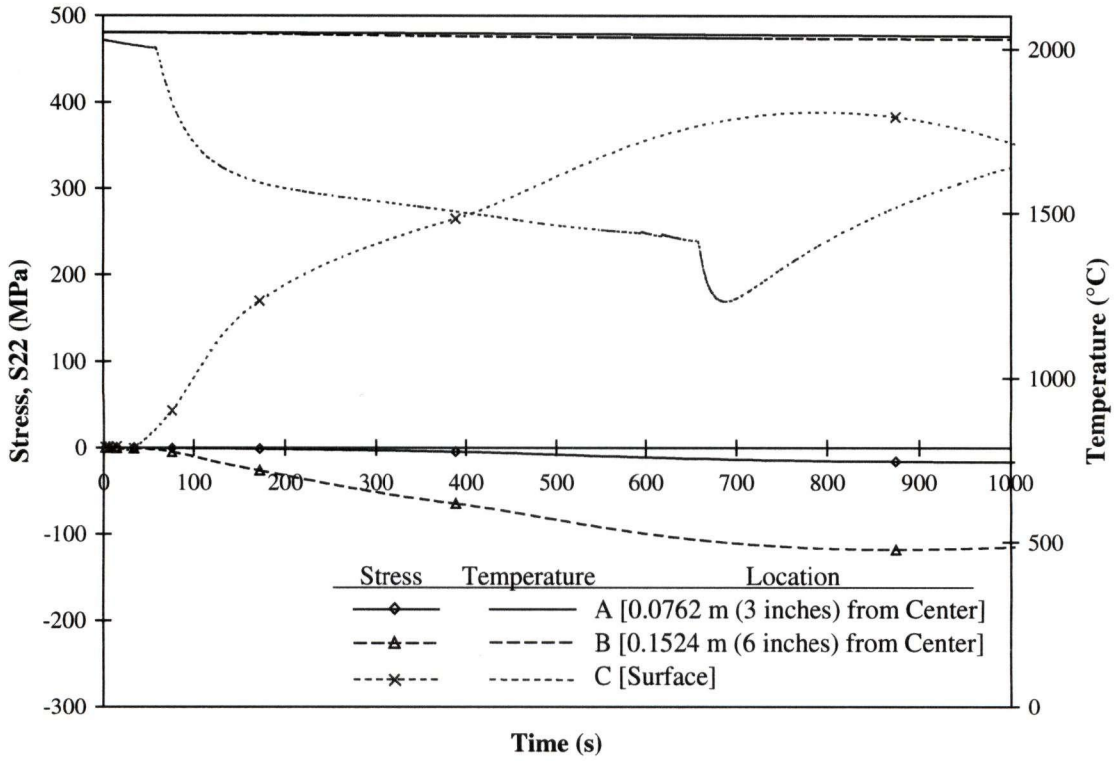

Figure 6.12 – Stress evolution of Monofrax-M during Stage I cooling for the elastic stress analysis with β-alumina core formation.

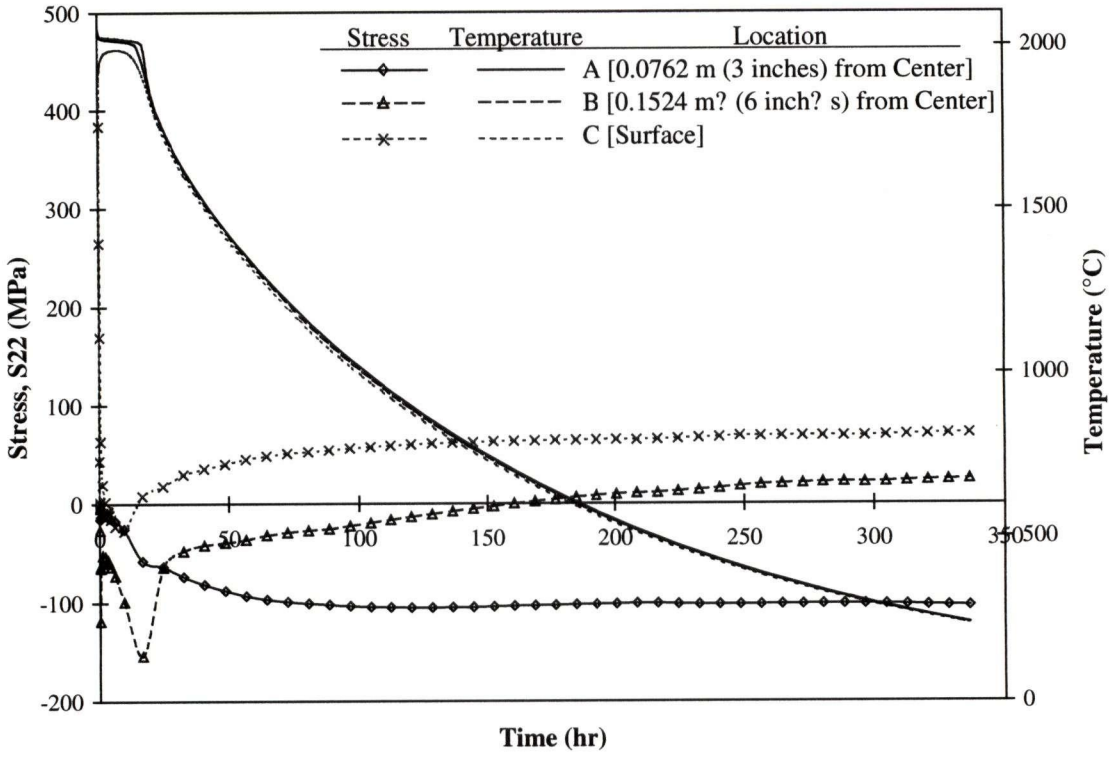

Figure 6.13 – Stress evolution of Monofrax-M during Stage II cooling for the elastic stress analysis with β-alumina formation.

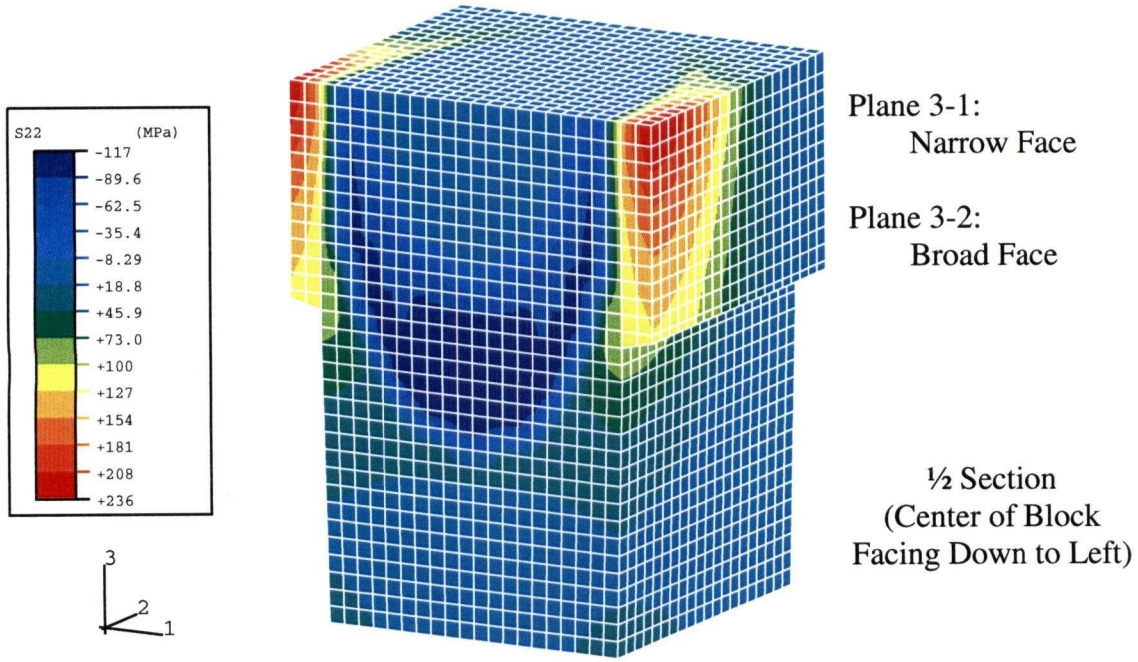

Figure 6.14 – Contour plot of S22 for Monofrax-M at the end of Stage II cooling for the elastic stress analysis with β-alumina core formation and void distribution.

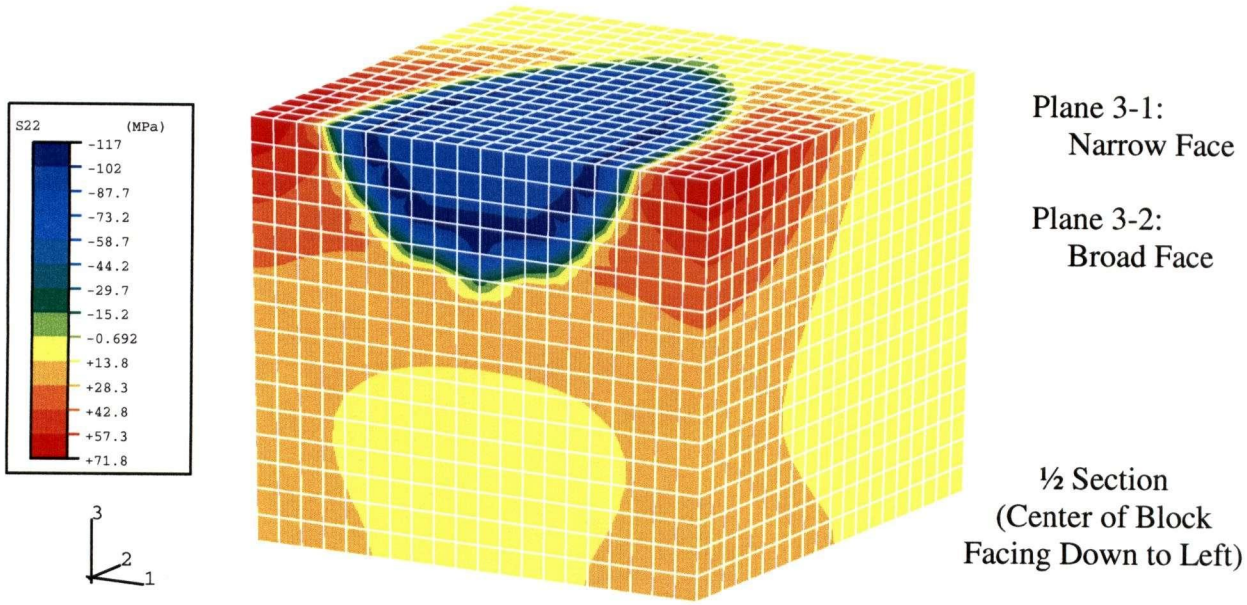

Figure 6.15 – Contour plot of S22 for the Monofrax-M crown block at the end of Stage II cooling for the elastic stress analysis with β-alumina core formation and void distribution.

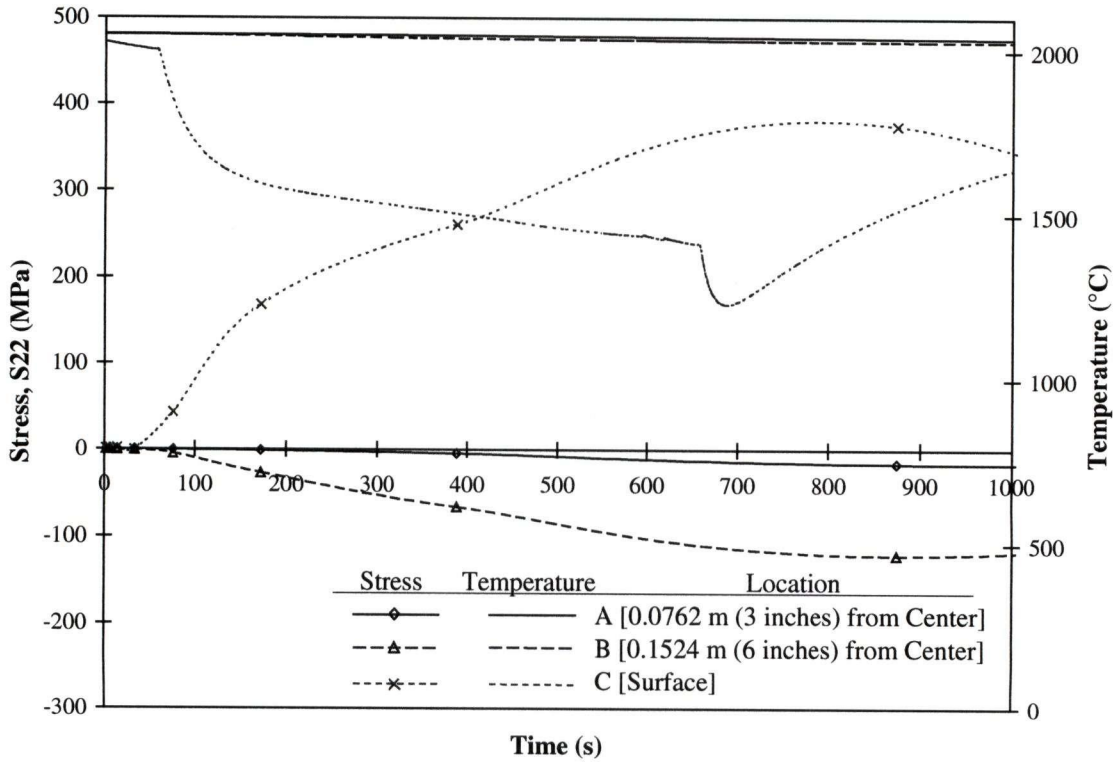

Figure 6.16 – Stress evolution of Monofrax-M during Stage I cooling for the elastic stress analysis with β-alumina core formation and void distribution.

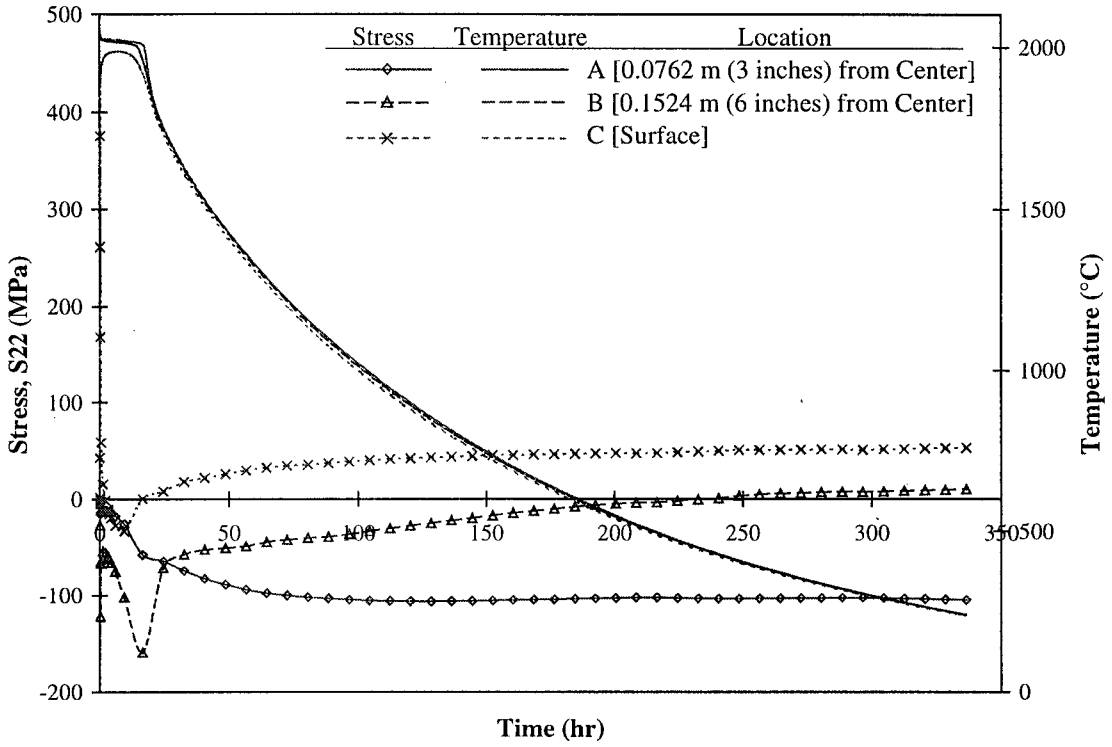

Figure 6.17 – Stress evolution of Monofrax-M during Stage II cooling for the elastic stress analysis with β-alumina core formation and void distribution.

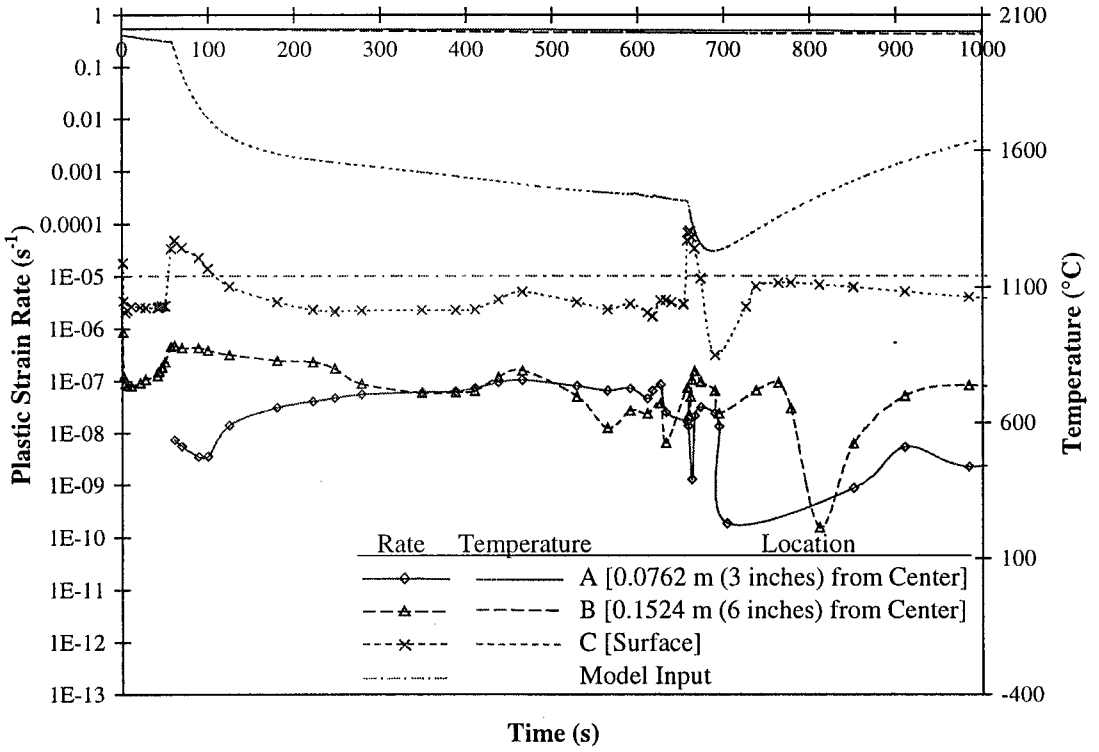

Figure 6.18 – Plastic strain rate evolution obtained from the elastic-plastic stress model of Monofrax-M during Stage I cooling.

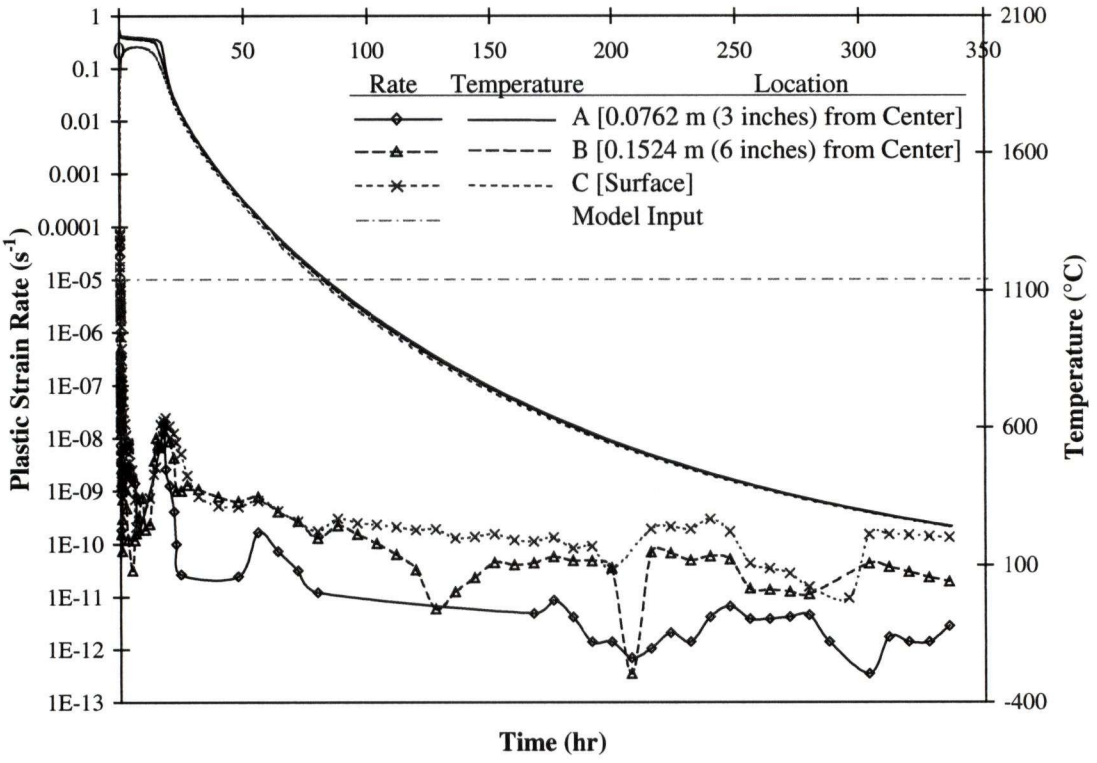

Figure 6.19 – Plastic strain rate evolution obtained from the elastic-plastic stress model of Monofrax-M during Stage II cooling.

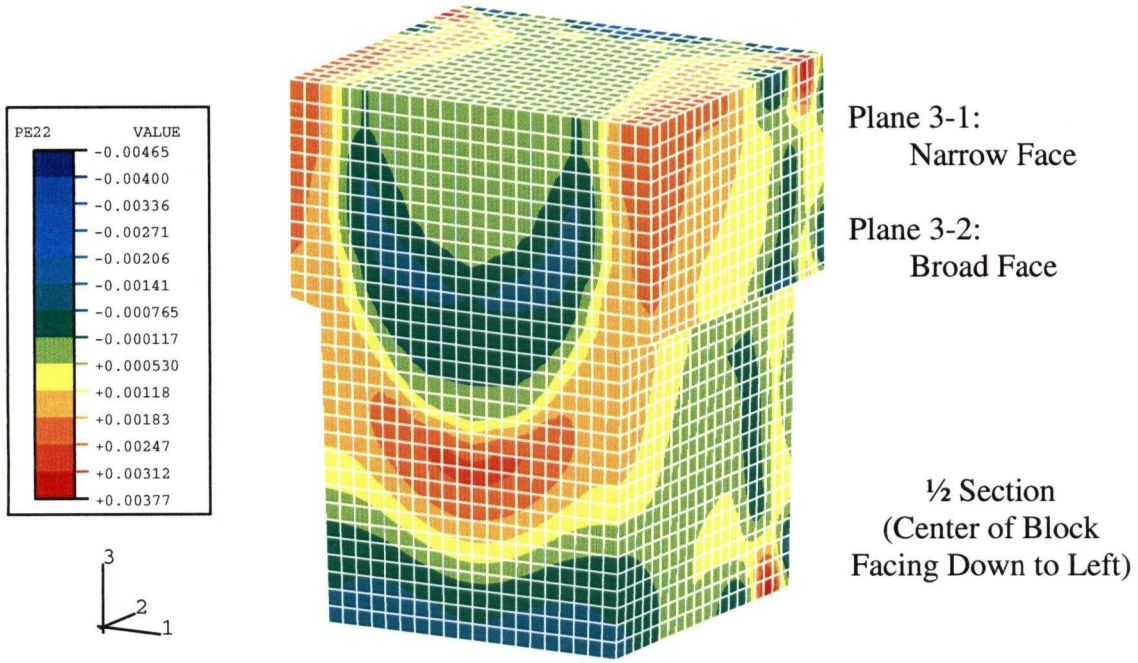

Figure 6.20 – Contour plot of PE22 obtained from the elastic-plastic stress model of Monofrax-M at the end of Stage II cooling.

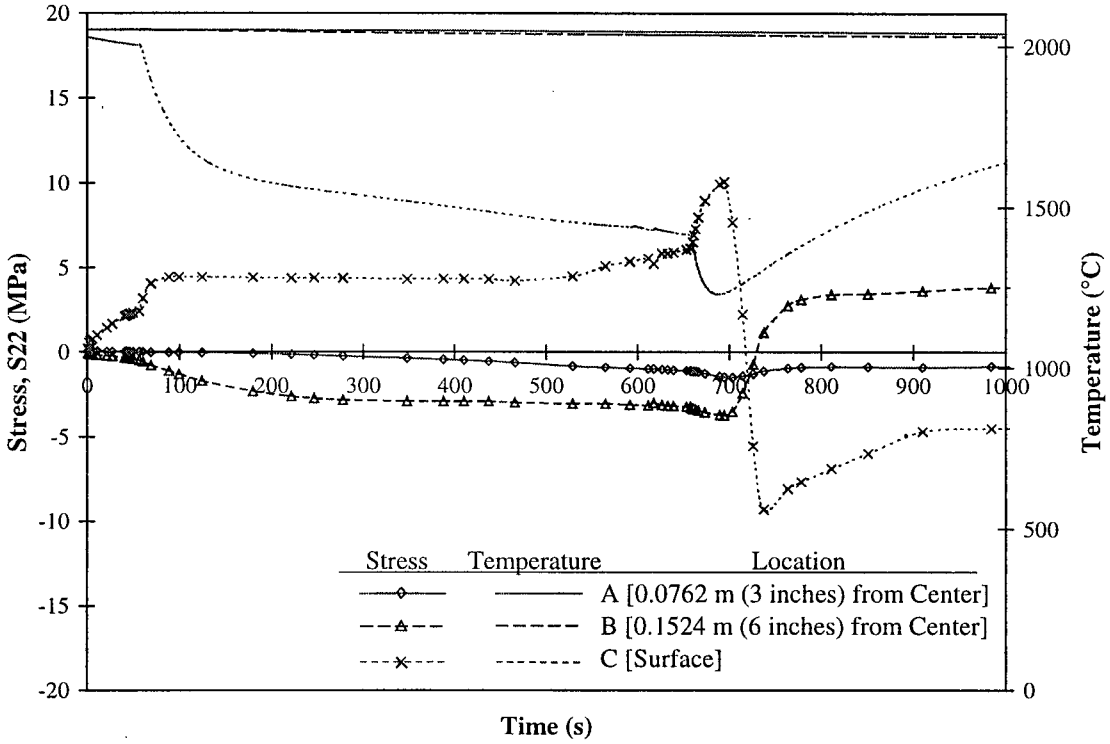

Figure 6.21 – Stress evolution obtained from the elastic-plastic stress model of Monofrax-M during Stage I cooling.

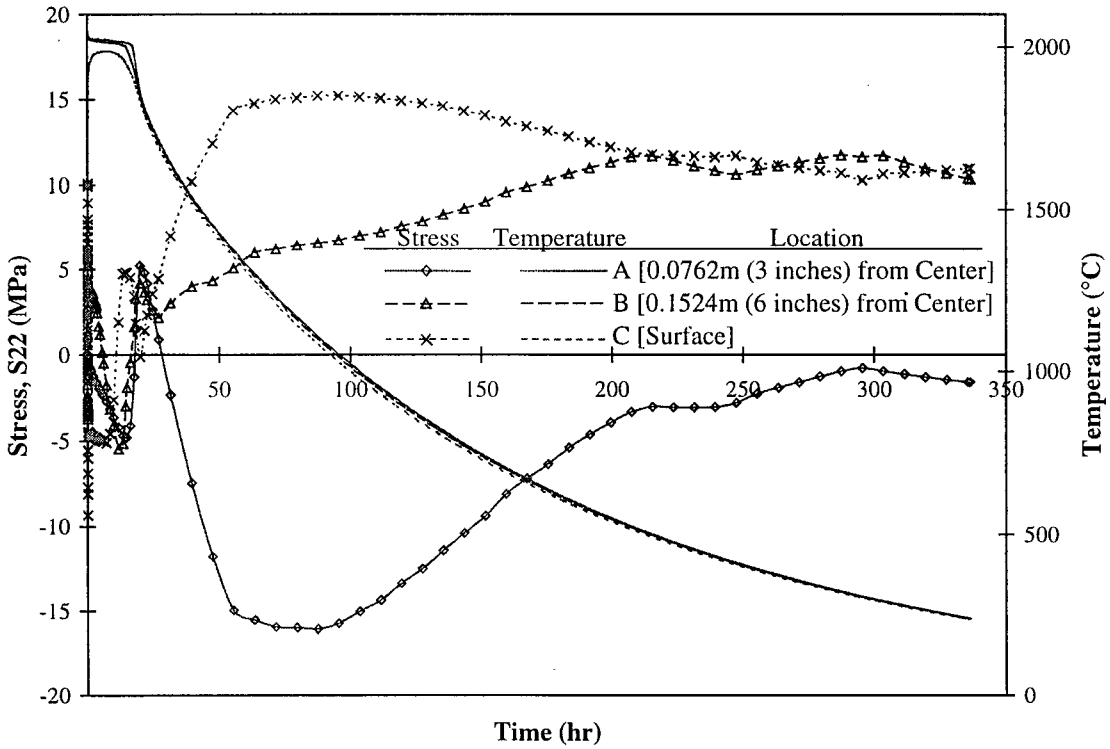

Figure 6.22 – Stress evolution obtained from the elastic-plastic stress model of Monofrax-M during Stage II cooling.

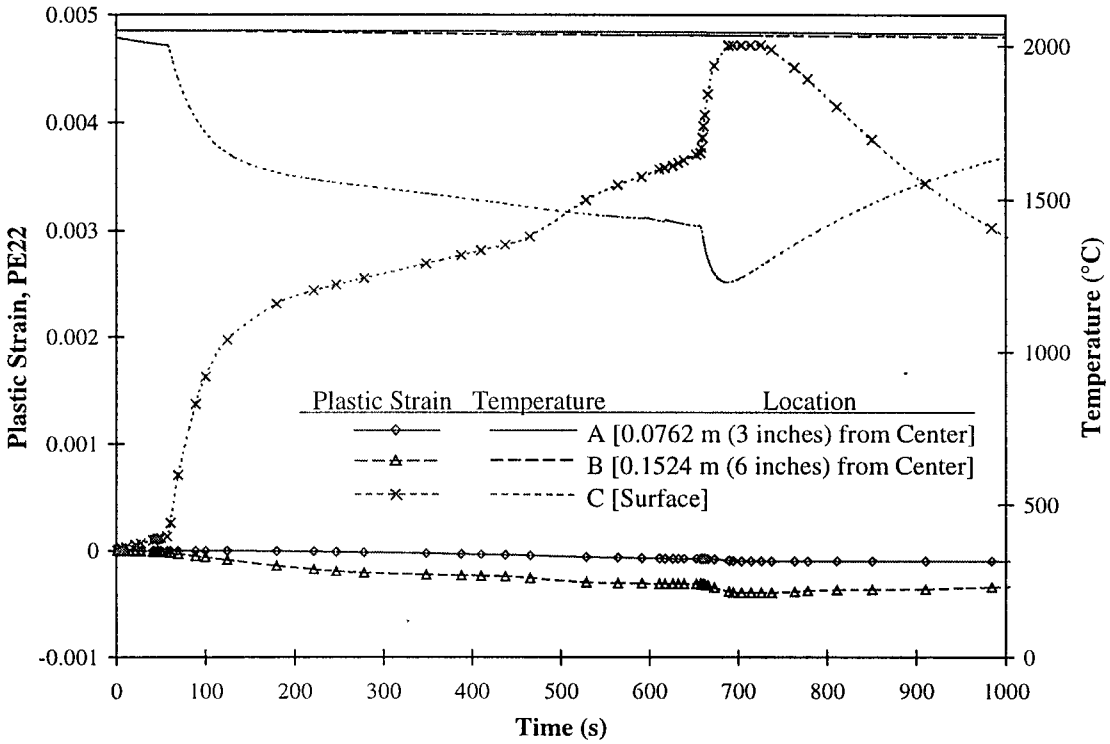

Figure 6.23 – Plastic strain evolution obtained from the elastic-plastic stress model of Monofrax-M during Stage I cooling.

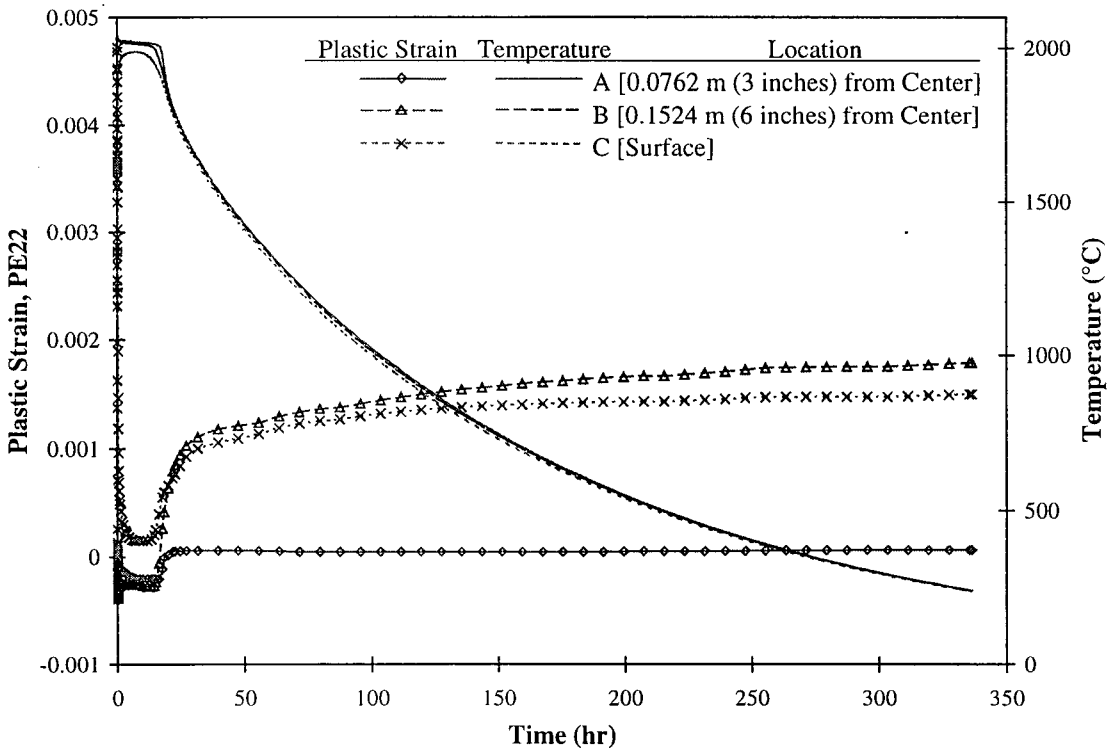

Figure 6.24 – Plastic strain evolution obtained from the elastic-plastic stress model of Monofrax-M during Stage II cooling.

CHAPTER 7

SUMMARY AND CONCLUSIONS

The present study has focused on developing mathematical models capable of predicting the temperature, stress and strain evolution in Monofrax-M crown blocks during the casting process. The finite element method has been adopted and utilized to analyze the manufacturing process. Industrial thermocouple and pyrometer measurements have been obtained to validate the heat transfer model. Experiments have also been performed to characterize the inelastic behavior of the fused-cast $\alpha\beta$-alumina refractory at elevated temperature.

The commercial finite element code ABAQUS was employed to develop an uncoupled thermal stress model. The thermal model was 'fine-tuned' and validated against the industrial thermocouple and pyrometer measurements obtained at Monofrax Inc. This has been accomplished based on a comparison between the predictions of the model and thermocouple data obtained at several locations from within the graphite mold, during Stage I cooling, and in the alumina annealing ore, during Stage II cooling. The 'fine-tuning' involved adjustment of the parameters that describe the thermal boundary conditions between the refractory and the molding materials. In Stage I cooling, it has been necessary to adopt a liquid conductivity multiplication factor in the thermal conductivity of the refractory to account for convective heat transport in the liquid. A sintering algorithm was also introduced in Stage II cooling to account for the increase in the thermal conductivity of the alumina annealing ore due to densification of ore on exposure to elevated temperature in the bin. However, optimal agreement was achieved with the sintering algorithm switched off.

The temperature predictions obtained from the thermal model were employed as input to the stress model. The αβ/β-alumina distribution as well as the void distribution were introduced into the ABAQUS stress model through a user subroutine. Elastic and elastic-plastic stress analyses were performed to investigate the stress and strain evolution developed during the casting process. The preliminary results predicted by the elastic-plastic stress model were more realistic than those obtained from the elastic analyses. Due to the limited available stress-strain data, the influence of strain rate dependent plasticity has not been investigated. Hence, the results of the plastic stress analysis should be considered only semi-qualitative. The plastic strain obtained employing data generated at a strain rate of $1x10^{-5}$ s^{-1} may be under-predicted during Stage II cooling. Nevertheless, the predictions of the model have been used to propose a mechanism for formation of the intergranular crack found in the Monofrax-M crown blocks.

The results of the stress analysis indicate that the temperature gradient that the casting experiences and the different dilatational behavior of the αβ/β-alumina are the main drivers of the stress/strain evolution, whereas the void distribution appears to have only a small effect. The β-alumina core, in particular, plays an important role in the generation of tensile stresses and likely gives rise to the generation of cracks. However, some cracking may also be associated with some of the processing steps. Based on the high tensile stress/strain developed within the refractory, it is likely that crack initiates subsurface and propagates outwards.

Overall, the results of the present study show the importance and usefulness of developing the ability to predict stress and strain evolution in the fused-cast αβ-alumina

refractories casting process. Based on an understanding of the mechanism of crack defect formation, procedures may be developed to reduce the likelihood of crack formation.

7.1 Recommendations for Future Work

Owing to the computational efficiency, the latent heat of Monofrax-M implemented in the present model is simplified such that the volumetric latent heat is released linearly over the liquidus and solidus of the refractory. Work should be undertaken to more correctly account for primary alpha and peritectic beta formation.

The β-alumina core distribution incorporated in the stress model was shown to be important in the stress and strain predictions. The β-alumina core, however, was assumed to be simplified ellipsoid and be present throughout the entire casting process. In reality, the β-alumina core is formed gradually when Na_2O is being rejected at the αβ/β-alumina interface. An algorithm based on mass diffusion should be implemented into the thermal model to attempt to predict its formation.

Finally, further investigation into time-dependent plasticity/creep relations is essential. It is likely that the rate-dependent plasticity has an influence on the inelastic deformation during both Stages I and II cooling. Also, creep tends to occur in the fused-cast refractory at elevated temperatures. Both primary and secondary creep characteristics should be assessed over a large temperature range that the casting experiences and implemented into the model to enhance the capability of the stress analysis.

Bibliography

1. Monofrax Inc. Engineered Materials Product Advertisement Brochure.

2. Private conversations with Monofrax Inc. personnel, 1997-1999.

3. A.E. McHale, R.S. Roth, eds. *Phase Equilibria Diagrams*. Vol. 12, Fig. 9883, American Ceramic Society, 1996.

4. J.K. Brimacombe, I.V. Samarasekera, S.L. Cockcroft. "Computer Simulation of Solidification and Casting Processes." *International Conference on Computer-assisted Materials Design and Process Simulation,* (1993).

5. P. Jeanmart, J. Bouvaist. "Finite Element Calculation and Measurement of thermal stresses in quenched plates of high-strength 7075 aluminium alloy." *Materials Science and Technology*, 1 (October 1985): 765-769.

6. J.W. Wiese, J.A. Dantzig. "Modeling Stress Development during the Solidification of Gray Iron Castings." *Met. Trans.*, 21A (1990): 489-497.

7. F. Bradley, A.C.D. Chaklader, A. Mitchell. "Thermal Stress Fracture of Refractory Lining Components; Part I, Thermoelastic Analysis." *Metall. Trans. B*, 18 (1987): 355-363.

8. W.S. Chang, C.E. Knight, D.P.H. Hasselman, R.G. Mitchiner. "Analysis of Thermal Stress Failure of Segmented Thick-Walled Refractory Structures." *J. Am.Ceram.Soc.*, 66, no. 10 (1983):708-713.

9. J. Knauder, R. Rathner. "Thermomechanical Analysis of Basic Refractories in a Bottom Blowing Converter." *Rader Rundschau*, 4 (December 1990): 354-365.

10. S.L. Cockcroft, J.K. Brimacombe. "Thermal Stress Analysis of Fused-Cast AZS Refractories during Production: Part I, Industrial Study." *J. Am. Ceram. Soc.*, 77, no. 6 (1994): 1505-1511.

11. S.L. Cockcroft, J.K. Brimacombe. "Thermal Stress Analysis of Fused-Cast AZS Refractories during Production: Part II, Development of Thermo-elastic Stress Model." *J. Am. Ceram. Soc.*, 77, no. 6 (1994): 1512-1521.

12. T.J. Lu, A.G. Evans, J.W. Hutchinson, G.V. Srinivasan, S.M. Winder. "Stress and Strain Evolution in Cast Refractory Blocks during Cooling." *J. Am. Ceram. Soc.*, 81, no. 4 (1998): 917-925.

13. T.J. Wang. "Modelling of the Cooling of the Fused Cast α, β-Al_2O_3 Refractory Mouldings." *Glass Technology*, 40, no. 1 (February 1999): 33-40.

14. A. Mo, E.J. Holm. "On the Use of Constitutive Internal Variable Equations for Thermal Stress Predictions in Aluminum Casting." *Journal of Thermal Stresses (USA)*, 14, no. 4 (1991): 571-587.

15. J.B. Wachtman. *Mechanical Properties of Ceramics*, John Wiley & Sons, Inc., 1996.

16. N.E. Dowling. *Mechanical Behavior of Materials*, 2nd ed. Prentice Hall International, Inc., 1999.

17. D.W. Richerson. *Modern Ceramic Engineering*, Marcel Dekker, Inc., 1992.

18. R.G. Munro. "Evaluated Material Properties for a Sintered α-Alumina." *J. Am. Ceram. Soc.*, 80, no. 8 (1997): 1919-1928.

19. A.A. Wereszczak, T.P. Kirkland, G.A. Pecoraro, R.A. New. "Compressive Creep Behavior of Fusion-Cast Alumina Refractories." *Advances in the Fusion and Processing of Glass, Transactions of the American Ceramic Society*, (1997): in press.

20. *JANAF thermochemical tables.* 3rd ed. U.S. National Bureau of Standards, 1985.

21. J.M. Gere, S.P. Timoshenko. *Mechanics of Materials*, 4th ed. PWS Publishing Company, 1997.

22. *Annual Book of ASTM Standards*, C1161. American Society for Testing and Materials, 1994.

23. United Technologies Research Center, Unpublished, 1997-1998.

24. F. Kreith, W.Z. Black. *Basic Heat Transfer.* Harper & Row Publishers, 1980.

25. Materials Science and Engineering Department, Virginia Polytechnic Institute, Unpublished, 1998.

26. Orton Refractory Testing and Research Center, Unpublished, 1998-1999.

27. Oak Ridge National Laboratory, Unpublished, March, 1999.

28. *Metals Handbook*, Vol. 1, 10th ed. ASM International, 1990.

29. J.-M. Drezet, M. Rappaz. "Modeling of Ingot Distortions During Direct Chill Casting of Aluminum Alloys." *Metallurgical and Materials Transactions A*, 27A (1996): 3214-3225.

30. O.C. Zienkiewicz, R.L. Taylor. *The Finite Element Method*, 4th ed. McGraw-Hill Book Co., 1994.

31. "Alumina, alpha Al2O3, 96%," in *MatWeb: The Online Materials Information Resource* [database on-line by Automation Creations, Inc.]; available from http://www.matls.com; Internet; accessed 20 August 1998.